Continuous Microfluidic Viscometers for Biochemical and Diagnostic Analysis

by

Yunzi Li

A dissertation submitted in partial fulfillment
of the requirements for the degree of
Doctor of Philosophy
(Chemical Engineering)
in the University of Michigan
2017

Doctoral Committee:

Professor Mark A. Burns, Chair
Professor Raoul Kopelman
Professor Ronald G. Larson
Professor Joerg Lahann

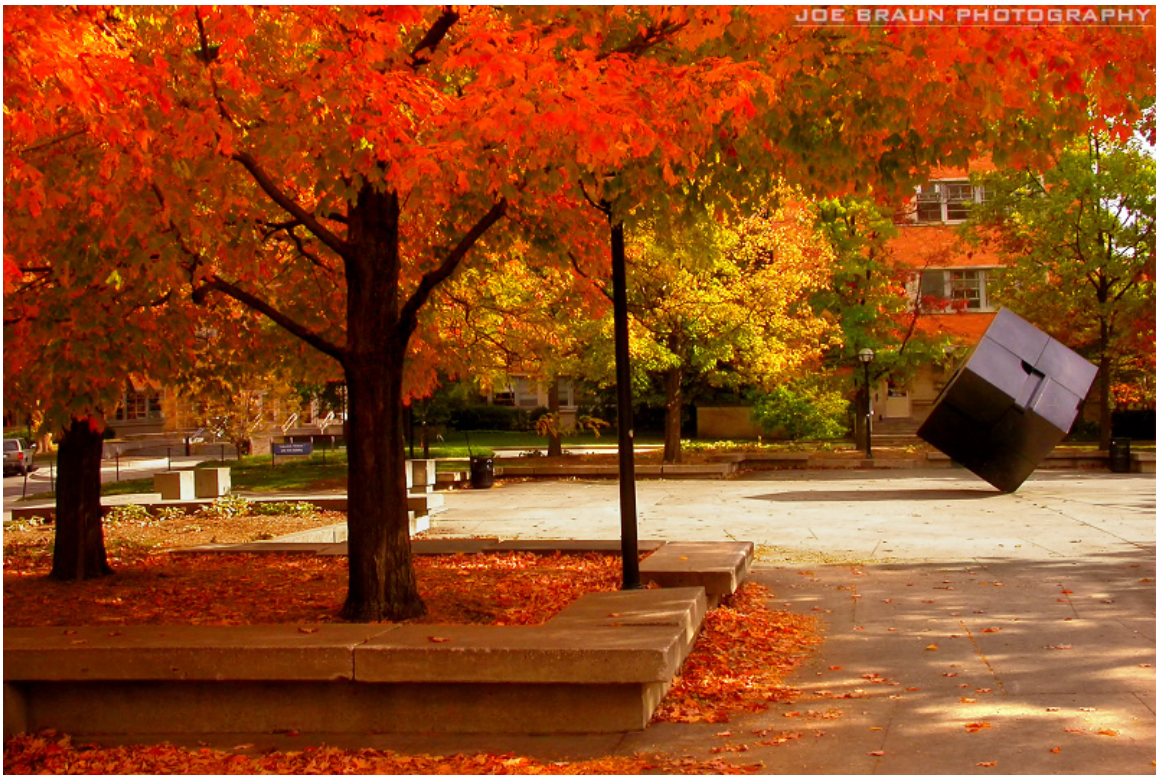

The University of Michigan's rotating Cube framed by the magical autumn foliage, by Joe Braun.

To my family

ACKNOWLEDGEMENTS

The past five years has been the most precious and unforgettable years of my life. Looking back to the past, I feel overwhelmed by the emotional flood and fall short of words to express my gratitude to all that have guided me, helped me, supported me, laughed with me, cried with me and adventured with me. I see myself continuously growing into a better me, and this is all because of you. Now I am very excited that I am here at the end of the five-year journey, willing to start my new adventure and make my own contributions to the society, but I am at the same time nervous to leave my loved ones here at Ann Arbor.

First, I would like to thank my advisor Prof. Mark A. Burns. I remember every single moment that he is there for me, cherishing or supporting me. He has always been an excellent example for me. I learnt how to be a teacher, respecting students, stimulating their self-motivation and coaching them to their destinations. I learnt how to be a researcher, always curious and brave but rigorously and persistently seeking the truth. I learnt how to sell an idea, how to negotiate deals, how to prioritize tasks, how to interact with people at work, how to balance time, and so on. Nearly every perspective of life that I seldom thought about before, but will enormously benefit from in my future.

I would also like to thank the rest of my dissertation committee, Prof. Raoul Kopelman, Prof. Ronald G. Larson and Prof. Joerg Lahann. I'm very grateful to Prof. Raoul Kopelman for his guidance and help on my first project, which is based on a technology originated from his group. I would also like to thank Prof. Ronald

G. Larson and Prof. Joerg Lahann for their technical insights and inspiring advice during our discussions on the physics of my viscometers and the application of the technology. In addition, I would like to express my gratitude to Prof. Kevin R. Ward and Prof. David T. Burke, as they have provided me with insights from the perspective of healthcare providers and made me aware of the most critical clinical issues. It's truly my honor to be able to discuss scientific challenges in my projects with these world-class scientists and learn from them.

I would like to extend my thanks to each member of the Burns group, both past and present. I would like to thank previous group members Dr. Jihyang Park, Dr. Irene Sinn and Dr. Eric M. Livak-Hale for their guidance, support and help. I would also like to thank current group members Brian Johnson, Dr. Sarah Mena, Jaesung Lee, Steven Wang, Wen-Chi Lin, Liang Zhang, Zach Pritchard, Martin de Beer, Ioana C. Nadra and Alyse Krausz. These amazing fellows have made my research life rewarding. We have numerous discussions on research as well as daily life, and they have been very supportive and encouraging. Brian, our research engineer, was always able to "magically" solve any problems on lab equipment and smooth my experiment. Eric is one of the smartest people I have ever met, and he has given me valuable advice on curriculum, research, writing and career even after he graduated from the group. Jaesung is one of the most rigorous and perfectionistic researchers, and I could not thank him more for his guidance and advice on research, literature review and experiment. Steven, who joined the group at the same time with me, has been one of my best friends and accompanied me for five years, taking classes, doing experiment and hanging out together.

I would also like to acknowledge students, staffs and researchers from outside my research group, who helped me with different aspects of my research. I would like to thank Brendan McCracken, Hyesun Jun, Jodi Wilkowski and David Boyer for their help in collection of biological specimens. In addition, I would like to thank Gregory

Allion, Terre Briggs, Robert Hower, Nadine Wang, Kevin Owen and Brian Armstrong for training and helping me in the cleanroom. Furthermore, I would like to thank Weizhong Zou, Dr. Zhenguang Huang, Dr. Tongyang Zhao, Dr. Taotao Fu, Tatyana Saleski, Theodore Glenn Albertson, Dr. Ming Qin, Dr. Jennifer Zhang, Dr. Xiaolin Xia, Dr. Chong Cheng, Letian Zhou, Dr. Zeta Yu, Dr. Daniel Sobczynski, Dr. Fengming Lin, Corine Jackman, Scott Scholz and Adam Krieger. They either discussed with me and offered suggestions on my research, or helped me in my experiment. Finally, I would like to thank the administrators, especially Kelly Raickovich and Susan Hamlin, whose hard work has indirectly made my research life so much easier.

While I'm treasuring the experience of meeting all these talented people, I know that I wouldn't have the chance to be here without Prof. Yongli Mi and Prof. Henry H. N. Lam at Hong Kong University of Science and Technology. They opened the door of research for me and ignited my interests to pursue this path. I couldn't thank them more for their supervision while I worked as an undergraduate research assistant in their groups, learning experimental and programming techniques. It's also them who believed strongly in me and encouraged me to apply to the graduate school here.

Through the ups and downs in the past five years, I grew to be stronger and got to know myself better. I developed new hobbies, such as gymming, baking and board games, and made many new friends. I opened a food blog in my final year of graduate study, and received more than 700 followers from Ann Arbor area. I'd also like to acknowledge them for their recognition and support of me. Thousands of miles away from home, my dear friends make a new home here for me, offering their unconditional love. I don't know how to thank them for this, or they even need my thanks. They are always there whenever I need them, and I truly felt adored and spoiled by them. My ex-roommates Janet Wei and Yik Lee Chieng had accompanied me for three years before they left Ann Arbor for career. They are like my sisters, and we have so many good memories together. Caroline and Floyd McNutt, "parents" of our household,

often visited us during periods of final exams, bringing food and desserts to us. Steven Wang and Weizhong Zou have always been with me through the five years, and their close friendship and support have been precious to me. I would also like to thank Chun Wan, Jingqian Chen, Jun Liu, Jingfei He, Miqiu Kong, Peng Tian, Peng Yin, Qi Chen, Zhenguang Huang and Zhongming Qu for their companions, as they remain some of my closest friends that I'm willing to share anything with. I know that I can't suffice here and I have many more friends to thank that I simply couldn't all fit in here. I'm very grateful to all of them for their friendship, and I believe that it will continue for a lifetime.

Finally, I would like to thank my family. My cousins Zhongyi Yang and Siqi Zhong have been and will always be my closest friends without secrets. I enjoyed the long hours that we spent over the phone in the past five years. My parents have always been my guidance and supports. They believe in me and grant me full freedom to explore my interests. My dad, a mechanical engineer, influenced me with his pure passion to science and engineering. On the other hand, my mom, also an engineer by training, pursued the track of training and managing people. She has put so much time and effort to help me discover my hidden capabilities and grow me into a better and happier person. I know for a hundred percent that they are the two in the world who love me the most no matter what. I'd also like them to know that I thank them so much for everything and love them forever.

TABLE OF CONTENTS

LIST OF FIGURES

Figure

LIST OF TABLES

Table

ABSTRACT

Continuous Microfluidic Viscometers for Biochemical and Diagnostic Analysis

by

Yunzi Li

Chair: Professor Mark A. Burns

Microfluidic technologies have advanced rapidly over the past two decades. Numerous microfluidic devices to assess different biomarkers have been reported, yet very few address physical properties, such as viscosities, of biological specimens. Continuous monitoring of viscosity changes provides a new biological and diagnostic parameter not yet made readily accessible due to the low obtainable volume of many biological specimens.

In this dissertation, we have developed a droplet-based, water-in-oil continuous viscometer capable of measuring viscosity changes in 10 seconds or less and consuming a total sample volume of less than 1 microliter per hour. The viscometer employs a flow-focusing geometry and generates droplets under constant pressure. The length of the droplets is highly correlated to the aqueous-phase viscosity at high ratios of aqueous-to-oil inlet pressure, resulting in a linear calibration relationship for viscosity measurements. Theoretical analysis verifies the linear relationship and guides viscometer optimization. The viscometer can be used for Newtonian fluids and, by accurately calculating shear rates, for non-Newtonian fluids. The shear rates can be

adjusted experimentally by varying the input pressures. The viscometer measures viscosities reliably over three orders of magnitude with less than 5% error. Using the viscometer, we measured viscosity changes of whole blood during blood coagulation continuously under different conditions.

We have also developed a particle-based microviscometer for label-free DNA detection by applying the asynchronous magnetic bead rotation (AMBR) phenomenon. We have demonstrated experimentally that the rotation period of paramagnetic beads is linearly proportional to the viscosity of a DNA solution surrounding the paramagnetic beads, as expected theoretically. Simple optical measurement of asynchronous microbead motion determines solution viscosity precisely in microscale volumes, thus allowing an estimate of DNA concentration or average fragment length. The effects of different operating conditions have been investigated and a standard deviation of less than 10% has been achieved for viscosity measurements under the optimal conditions. The response of the AMBR viscometer yields reproducible measurement of DNA solutions, enzymatic digestion reactions, and PCR systems at template concentrations across a 5000-fold range. Preliminary design and operation of a ChessTrap device has been demonstrated to trap single particles into individual chambers for viscometer automation.

CHAPTER I

Introduction

1.1 Significance of Miniaturization of Biochemical and Diagnostic Analysis

Early diagnosis and immediate initiation of treatment are crucial to prevent unnecessary mortality and morbidity in numerous diseases. As examples, more than 23 million cases of malaria and 20-30 million cases of sepsis have been estimated globally every year, resulting in millions of deaths and billions of dollars in hospital expenditure. [1–4] Various types of diseases present different challenges to the development of diagnostic tools. For infectious diseases, cheap and simple diagnostic technology with multiplexing capability is highly desirable, because of the wide spread of numerous kinds of infectious diseases in developing countries. In the field of emergency care, diagnosis of diseases, such as coagulopathy and sepsis, requires quick diagnostic tools available in the emergency room, intensive care unit (ICU) or even on an ambulance. To diagnose and control chronic diseases like cardiovascular diseases and diabetes, certain biomarkers (e.g. blood viscosity or glucose concentration) need to be routinely monitored, so diagnostic kits requiring minimal sample volumes for patients to use at home demonstrate tremendous potential.

Interestingly, all these challenges suggest a single solution – miniaturization of the

diagnostic tool. As diagnostic equipment shrinks in size, the required sample volume also decreases. The diagnosis speeds up due to more efficient transport of reactants within the miniaturized device. As a result, the time and cost of diagnostic tests decrease, and on-site diagnosis is made possible. Moreover, low sample requirement in miniaturized diagnostic technology will enable assessment of biological information not yet made accessible. Such information includes continuous data (e.g. blood viscosity) from routinely examined blood samples and biomarkers present in biological specimens at minuscule scale, such as sweats, tears and gingival crevicular fluids (between teeth and gum). [5–8] Therefore, miniaturized diagnostic solutions could revolutionize the field of medical diagnosis and benefit all patients around the world.

1.2 Microfluidic Technology

Microfluidics is a technology that manipulates minuscule amounts of fluids (as low as femto- to picoliter scales) at length scales on the order of micrometers to millimeters. The advent of microfluidic devices, also commonly known as miniaturized total analysis systems (μTAS) or lab-on-a-chip devices, dates at least back to 1980s. [9–12] The first use of microfluidic technology leverages the fabrication technology of semiconductor devices and micro-electromechanical systems (MEMS) for chemical analysis. [13] Since then, the microfluidic technology has attracted significant attention and has emerged rapidly in various fields ranging from medical diagnosis to chemical synthesis. [11, 14–17] To meet the increasing needs for robust, versatile and low-cost fabrication methods for these new applications, the portfolio of microfabrication technologies has also been expanded, from photolithography on glass, silicon and polymer substrates [18–20] to 3D printing of plastics, elastomers and photopolymers [21–23].

The transport phenomena in microfluidic systems differ significantly from those at the macroscale. [11, 24, 25] At the microscale, the effects of gravitational forces have been greatly reduced, and other forces, such as capillary forces, surface tensions

and viscous forces, play more important roles. Consequently, the Reynolds number, Re, in microfluidic systems is typically very low, and they are defined as

$$\mathrm{Re} = \frac{\rho \mathrm{vL}}{\mu} \tag{1.1}$$

where ρ is the density of the fluid, v is the flow velocity of the fluid, L is the characteristic length and μ is the viscosity of the fluid. At such low Reynolds numbers, the viscous forces dominate the inertial forces, resulting in laminar flow conditions. The Péclet number, Pe, a measure of the convective-to-diffusive transport rates, is also low in these systems,

$$\mathrm{Pe} = \frac{\mathrm{vL}}{\mathrm{D}} \tag{1.2}$$

where D is the diffusion coefficients. Diffusion therefore dominates fluid mixing.

With increased understanding of the physics within the microfluidic systems, numerous microfluidic components and subsequently integrated microfluidic platforms have been developed over the past two decades. [10] Researchers have developed a broad spectrum of microfluidic components, from micropumps, microvalves and micromixers, to microreactors, microseparators and microsensors. The integration and ultimately automation of these elements into a single chip pose great challenges to the microfabrication process as well as management of efficient heat and mass transport on a chip. [10, 14] The first integrated microfluidic device in the literature is a DNA analysis device with on-chip heaters, reactors, separators, temperature sensors and fluorescent detectors. [26] This device, for the first time, addresses the challenges of incompatibility of various microfluidic elements. With continuous research and development of microfluidic technology, it is foreseen that microfluidic devices could influence and revolutionize the field of medical diagnosis, providing individuals with point-of-care diagnostic tools.

1.3 Droplet-based Biosensors

Droplet-based microfluidic systems introduce compartmentalization to microfluidic systems. [27–29] Unlike continuous flow systems, droplet-based systems generate discrete volumes via emulsions of two or more immiscible phases. This extra degree of freedom due to the immiscible phase allows each droplet to perform a different reaction independently from another neighboring droplet, thus enabling parallelization and multiplexing of reactions without significantly increasing device size or complexity. [27] Within individual droplets, mixing occurs more rapidly than continuous flow systems, due to the presence of internal convective circulation. Between droplets, there is generally no material exchange. However, diffusion through the interface can occur if the molecules are soluble in both phases, resulting in inter-droplet material exchange over long periods of time. [29]

A merit of droplet generation in microfluidic systems is the capability to produce uniform droplets at a high throughput. Droplet formation can be induced by instabilities at the interface, such as capillary, interfacial and shear-driven instabilities. [30–32] The relevant dimensionless number is the capillary number, Ca, which is defined as

$$\mathrm{Ca} = \frac{\mu \mathrm{v}}{\gamma} \tag{1.3}$$

where γ is the interfacial tension between the immiscible phases. Therefore, the capillary number compares the relative importance of viscous forces to interfacial tensions. At a low capillary number (i.e., $\mathrm{Ca} < 10^{-2}$), the volume of droplets is linearly proportional to the ratio of the dispersed-phase to continuous-phase flow rate. [33, 34] At a high capillary number, the radius of droplets scales with the inverse of the capillary number. [35] The three most common channel geometries for droplet generation are co-flowing, T-junction and flow-focusing geometry. [36–38] In

such devices, a droplet polydispersity of 1-3% can be achieved at a typical rate of up to several kHz. [28, 36, 37, 39]

After droplets are produced, they can be readily transported and manipulated for downstream processes. [28, 29, 37, 40] The droplets are transported down a pressure gradient with the carrier fluid (i.e., the continuous phase). The latter is often driven by a constant flow or constant pressure/vacuum source. Upon arrival at the appropriate location, droplets are manipulated by techniques such as droplet merging, mixing, trapping, storage/incubation, splitting and sorting. The droplet manipulation can be achieved through hydrodynamic effects, physical intervention (e.g. obstacles, constrictions/expansions and valves) or field-assisted approaches (e.g. electric and magnetic fields). A thorough review on various droplet manipulation techniques can be found in [27, 29].

Due to their ultra-high multiplexing, throughput and integration capabilities, droplet-based microfluidic systems have been applied to areas, such as high-throughput screens of drugs, enzymes and microbial communities and the "omic" sciences of genes, proteins and cells (or microorganisms). [28, 39, 41, 42] A library of droplets can be generated, where each droplet stores a different element (e.g. DNA, protein or single cell). These droplets are subsequently manipulated and assayed to decode biological information. For example, the Weitz group has developed a droplet-based platform for high-throughput drug screening. [39, 43, 44] A droplet library is generated in which each droplet contains a potential antimicrobial drug. Then, a single microbial cell is encapsulated into each droplet through droplet merging. Upon droplet incubation, the microbial cell in each droplet is either killed by the drug or grows in population. Droplets containing effective drugs are subsequently sorted and the effective drugs are identified by their barcodes (e.g. nucleic acid sequences or fluorophore combinations). This method enables rapid screening of millions to billions of candidates with sample volumes on the orders of 100 μl. Therefore, droplet-based

microfluidic systems are ideal candidates for bio-sensing.

1.4 Particle-based Biosensors

In the past decades, the research involving micro- and nanoparticle biosensors has grown by leaps and bounds. As understanding of these systems and the methods of synthesizing magnetic particles have steadily improved, magnetic particles have become an increasingly common tool in many avenues of research. While the way in which such particles have been used varies a great deal, magnetic particles have turned into successful biosensors because biological systems of interest do not contain any significant magnetic background that would be affected by the relatively small magnetic fields associated with magnetic particle biosensors. [45] This means that magnetic particles can easily be used to transport and/or isolate biological targets using an external magnetic field. But more importantly, it means that if measurements associated with the magnetic particles can be made reliably, there is no magnetic signal associated with the biological system that could contaminate the information from the magnetic particles. For this reason, even small signals associated with magnetic particles can reliably be used to detect instances of biological interaction.

Since their first use as biosensors in the mid-1990s, magnetic particles have been used for bio-sensing in a wide variety of detection methods and platforms. [46–50] More recently, magnetic particle biosensors have been integrated into microfluidic systems, further increasing the speed, sensitivity and robustness of the particle-based technologies. [46, 51, 52] While the techniques have been numerous, magnetic particle biosensors can be divided into three categories by the functionality of the magnetic particles in these biosensors: magnetic particles as carriers for signal intensification, magnetic particles as labels to detect magnetic contents, and bio-sensing based on the dynamics of magnetic particles. While not every example fits perfectly into one category, these are the major ways in which magnetic particles are used as biosensors.

The first category uses the magnetic particles as a solid phase for capturing the target of interest and increasing the concentration of the target via magnetic separation. Some kind of label, generally non-magnetic, is used to report the presence of the target. For this category, the aspect that changes is the reporter – the system or method that is used to detect the presence of the target. The magnetic label method uses the magnetic particles themselves to report the presence of the target of interest. In these systems, it is the method of magnetic particle detection that changes throughout the various techniques. More recently, the dynamics of magnetic particles in a magnetic field has been widely studied and used to infer different physical and biological properties of biological samples as well as to detect the presence of the target, adding more dimensions to magnetic particle biosensors. Generally, the rotational motion of magnetic particles is measured optically, and properties/targets of interests can be quantified from the dynamic theory. The dynamic theory, and thus the method of quantification, varies with the shape and quantity of magnetic particles used in these systems.

Amidst various magnetic dynamics-based bio-sensing strategies, the asynchronous magnetic bead rotation (AMBR) biosensor is one of the earliest and most diverse methods in the literature. In AMBR systems, spherical magnetic particles (i.e., ferromagnetic, superparamagnetic, or paramagnetic particles) are placed in a rotating magnetic field generated by perpendicular electromagnetic coils or a rotating magnet. The magnetic particle rotates asynchronously with the driving field when the driving frequency exceeds a critical value, because the magnetic particle cannot overcome the viscous drag exerted by the surrounding fluids. [53, 54] The rotational motion of the magnetic particle in this asynchronous regime is recorded, and the apparent rotational periodicity of the magnetic particle is correlated with the measured properties, [54–57]

$$\dot{\theta} = \frac{\chi'' \mathrm{V_m B^2}}{\kappa \eta \mathrm{V} \mu_0} \tag{1.4}$$

where $\dot{\theta}$ is the rotational frequency, χ'' is the imaginary part of magnetic susceptibility (which is frequency dependent), $\mathrm{V_m}$ is the volume of magnetic content, B is strength of the magnetic field, κ is the shape factor of the particle (e.g. $\kappa = 6$ for sphere), η is the viscosity of the surrounding fluids, V is the volume of the particle, and μ_0 is the permeability of free space. By detecting analyte-induced volume changes of magnetic particles, AMBR biosensors have been applied to biomolecule detection [58, 59], single cell detection [60, 61], cell growth and drug susceptibility monitoring [57, 62, 63].

1.5 Organization of the Dissertation

This dissertation will primarily discuss the design and development of droplet-based and particle-based microfluidic viscometers for bio-sensing. It will first discuss a droplet-based continuous viscometer and its applications in measurements of Newtonian, non-Newtonian and biological fluids. Next, a magnetic particle based viscometer and its application in DNA diagnostic reactions will be presented, followed by preliminary design and fabrication of a microfluidic platform for particle manipulation. Some of the chapters in this dissertation have been published or submitted as journal articles, and are presented here with minor adaptions. Some are in preparation for submission as journal articles or book chapters.

Chapter I - Introduction: The introduction discusses the motivation of this thesis and introduces droplet-based and particle-based microfluidic technologies.

Chapter II - Droplet-based Microfluidic Viscometer: This chapter presents the design and development of a droplet-based (i.e., water-in-oil) microfluidic viscometer. The viscometer employs a flow-focusing geometry and generates droplets under constant pressure. With a pre-calibrated linear relationship, the aqueous-phase viscosity

can be readily determined from the optically measured droplet lengths. Optimization of operating pressures, oil-phase viscosity and device geometry has been studied theoretically, followed by experimental verification. The device has been demonstrated to measure viscosities of Newtonian fluids accurately over a range of three orders of magnitude.

Chapter III - Analysis of Non-Newtonian Fluids using a Microfluidic Viscometer: Chapter III extends the system in Chapter II to viscosity measurements of non-Newtonian fluids. The use of droplet lengths for viscosity measurements is still valid for non-Newtonian fluids. Using the power law model for non-Newtonian fluids, the shear rate, adjustable by varying operating pressures, can be calculated from the velocity of the aqueous phase. By modifying the geometry of the device, two modes of operations have been achieved. One mode allows precise measurements of absolute viscosities at various shear rates, and the other favors continuous viscosity monitoring at a constant shear rate.

Chapter IV - Whole Blood and Blood Coagulation Analysis: This chapter applies the droplet-based microfluidic viscometer to study viscoelastic properties of blood and blood that has undergone reactions. Banked blood of different storage duration and blood coagulation of citrated whole blood of different storage duration at various temperatures and shear rates have been analyzed. Also, a preliminary prototype of capacitive droplet sensor for device automation has been designed and fabricated.

Chapter V - Asynchronous Magnetic Bead Rotation (AMBR) Microviscometer for Label-Free DNA Analysis: This chapter reports the design and development of a particle-based microviscometer. The AMBR viscometer measures the rotational period of the asynchronous motion of a spherical paramagnetic particle in a rotating magnetic field. The viscosity of a DNA solution surrounding the magnetic particle can be calculated from the rotational period with a linear calibration relationship. The successful use of the AMBR viscometer for label-free DNA quantification has been

demonstrated in DNA solutions, enzymatic digestion reactions, and PCR systems. Sections are adapted and reprinted with permission by *Biosensors* [64].

Chapter VI - Preliminary Design of ChessTrap for Particle/Droplet Manipulation: This chapter presents initial work towards a microfluidic platform to manipulate particles/droplets. The ChessTrap design features a chessboard-like layer of trapping chambers with a single through-hole in each chamber and a membrane-based normally closed valve for flow control. Preliminary results show that the prototype device is able to capture a single magnetic particle into each chamber.

Chapter VII - Conclusion and Future Work: This chapter concludes the dissertation and identifies potential future directions. Overall, this dissertation primarily presents miniaturized tools to measure viscoelastic properties of biological fluids in biochemical and diagnostic analysis. These tools bridge the gap between viscosity changes and biological events, thus enabling rapid assessment of a new biophysical parameter not yet made accessible.

1.6 Bibliography

[1] World Health Organization. World health statistics 2013. Report, 2013.

[2] Global Sepsis Alliance. The world sepsis day fact sheet. Report, 2013.

[3] M. J. Hall, S. N. Williams, C. J. DeFrances, and A. Golosinskiy. Inpatient care for septicemia or sepsis: a challenge for patients and hospitals. 2011.

[4] C. Fleischmann, A. Scherag, N. K. Adhikari, C. S. Hartog, T. Tsaganos, P. Schlattmann, D. C. Angus, K. Reinhart, and Trialists International Forum of Acute Care. Assessment of global incidence and mortality of hospital-treated sepsis. current estimates and limitations. *Am J Respir Crit Care Med*, 193(3):259–72, 2016.

[5] I. B. Lamster and J. K. Ahlo. Analysis of gingival crevicular fluid as applied to the diagnosis of oral and systemic diseases. *Ann N Y Acad Sci*, 1098:216–29, 2007.

[6] The Gerber Foundation. Annual report. Report, 2014.

[7] P. Atram, P. Patil, F. Saify, V. Rathod, and S. Gotmare. Gingival crevicular fluid: As a diagnostic marker in hiv positive patients. *Journal of International Society of Preventive & Community Dentistry*, 5(1):24–30, 2015.

[8] W. Gao, S. Emaminejad, H. Y. Nyein, S. Challa, K. Chen, A. Peck, H. M. Fahad, H. Ota, H. Shiraki, D. Kiriya, D. H. Lien, G. A. Brooks, R. W. Davis, and A. Javey. Fully integrated wearable sensor arrays for multiplexed in situ perspiration analysis. *Nature*, 529(7587):509–14, 2016.

[9] G. M. Whitesides. The origins and the future of microfluidics. *Nature*, 442(7101):368–73, 2006.

[10] D. Mark, S. Haeberle, G. Roth, F. von Stetten, and R. Zengerle. Microfluidic lab-on-a-chip platforms: requirements, characteristics and applications. *Chem Soc Rev*, 39(3):1153–82, 2010.

[11] E. K. Sackmann, A. L. Fulton, and D. J. Beebe. The present and future role of microfluidics in biomedical research. *Nature*, 507(7491):181–9, 2014.

[12] R. Ahn, T. F. Burke, and A. M. McGahan. *Innovating for Healthy Urbanization*. Springer, 2015.

[13] A. Manz, N. Graber, and H. M. Widmer. Miniaturized total chemical analysis systems: a novel concept for chemical sensing. *Sensors and actuators B: Chemical*, 1(1):244–248, 1990.

[14] M. A. Burns. Everyone's a (future) chemist. *Science*, 296(5574):1818–1819, 2002.

[15] S. Li, J. Kiehne, L. I. Sinoway, C. E. Cameron, and T. J. Huang. Microfluidic opportunities in the field of nutrition. *Lab Chip*, 13(20):3993–4003, 2013.

[16] K. S. Elvira, X. Casadevall i Solvas, R. C. Wootton, and A. J. deMello. The past, present and potential for microfluidic reactor technology in chemical synthesis. *Nat Chem*, 5(11):905–15, 2013.

[17] T. W. Phillips, I. G. Lignos, R. M. Maceiczyk, A. J. deMello, and J. C. deMello. Nanocrystal synthesis in microfluidic reactors: where next? *Lab Chip*, 14(17):3172–80, 2014.

[18] P. Abgrall and A. M. Gué. Lab-on-chip technologies: making a microfluidic network and coupling it into a complete microsystem – a review. *Journal of Micromechanics and Microengineering*, 17(5):R15–R49, 2007.

[19] P. Kim, K. W. Kwon, M. C. Park, S. H. Lee, S. M. Kim, and K. Y. Suh. Soft lithography for microfluidics: a review. 2008.

[20] V. Faustino, S. O. Catarino, R. Lima, and G. Minas. Biomedical microfluidic devices by using low-cost fabrication techniques: A review. *J Biomech*, 49(11):2280–92, 2016.

[21] B. C. Gross, J. L. Erkal, S. Y. Lockwood, C. Chen, and D. M. Spence. Evaluation of 3d printing and its potential impact on biotechnology and the chemical sciences. *Anal Chem*, 86(7):3240–53, 2014.

[22] C. M. Ho, S. H. Ng, K. H. Li, and Y. J. Yoon. 3d printed microfluidics for biological applications. *Lab Chip*, 15(18):3627–37, 2015.

[23] N. Bhattacharjee, A. Urrios, S. Kang, and A. Folch. The upcoming 3d-printing revolution in microfluidics. *Lab Chip*, 16(10):1720–42, 2016.

[24] H. Bruus. *Theoretical microfluidics, Oxford master series in condensed matter physics*. Oxford University Press Oxford, 2008.

[25] E. Livak-Dahl, I. Sinn, and M. Burns. Microfluidic chemical analysis systems. *Annu Rev Chem Biomol Eng*, 2:325–53, 2011.

[26] M. A. Burns, B. N. Johnson, S. N. Brahmasandra, K. Handique, J. R. Webster, M. Krishnan, T. S. Sammarco, P. M. Man, D. Jones, and D. Heldsinger. An integrated nanoliter dna analysis device. *Science*, 282(5388):484–487, 1998.

[27] S. Y. Teh, R. Lin, L. H. Hung, and A. P. Lee. Droplet microfluidics. *Lab Chip*, 8(2):198–220, 2008.

[28] X. Casadevall i Solvas and A. deMello. Droplet microfluidics: recent developments and future applications. *Chem Commun (Camb)*, 47(7):1936–42, 2011.

[29] R. Seemann, M. Brinkmann, T. Pfohl, and S. Herminghaus. Droplet based microfluidics. *Rep Prog Phys*, 75(1):016601, 2012.

[30] M. Hashimoto, P. Garstecki, H. A. Stone, and G. M. Whitesides. Interfacial instabilities in a microfluidic hele-shaw cell. *Soft Matter*, 4(7):1403, 2008.

[31] J. K. Nunes, S. S. Tsai, J. Wan, and H. A. Stone. Dripping and jetting in microfluidic multiphase flows applied to particle and fiber synthesis. *J Phys D Appl Phys*, 46(11), 2013.

[32] G. Bolognesi, A. Hargreaves, A. D. Ward, A. K. Kirby, C. D. Bain, and O. Ces. Microfluidic generation of monodisperse ultra-low interfacial tension oil droplets in water. *RSC Adv.*, 5(11):8114–8121, 2015.

[33] P. Garstecki, H. A. Stone, and G. M. Whitesides. Mechanism for flow-rate controlled breakup in confined geometries: a route to monodisperse emulsions. *Phys Rev Lett*, 94(16):164501, 2005.

[34] P. Garstecki, M. J. Fuerstman, H. A. Stone, and G. M. Whitesides. Formation of droplets and bubbles in a microfluidic t-junction-scaling and mechanism of break-up. *Lab Chip*, 6(3):437–46, 2006.

[35] T. Thorsen, R. W. Roberts, F. H. Arnold, and S. R. Quake. Dynamic pattern formation in a vesicle-generating microfluidic device. *Phys Rev Lett*, 86(18):4163–6, 2001.

[36] G. F. Christopher and S. L. Anna. Microfluidic methods for generating continuous droplet streams. *Journal of Physics D: Applied Physics*, 40(19):R319–R336, 2007.

[37] C. N. Baroud, F. Gallaire, and R. Dangla. Dynamics of microfluidic droplets. *Lab on a Chip*, 10(16):2032–2045, 2010.

[38] S. L. Anna. Droplets and bubbles in microfluidic devices. *Annual Review of Fluid Mechanics*, 48(1):285–309, 2016.

[39] M. T. Guo, A. Rotem, J. A. Heyman, and D. A. Weitz. Droplet microfluidics for high-throughput biological assays. *Lab Chip*, 12(12):2146–55, 2012.

[40] E. Samiei, M. Tabrizian, and M. Hoorfar. A review of digital microfluidics as portable platforms for lab-on a-chip applications. *Lab Chip*, 16(13):2376–96, 2016.

[41] P. S. Dittrich and A. Manz. Lab-on-a-chip: microfluidics in drug discovery. *Nat Rev Drug Discov*, 5(3):210–8, 2006.

[42] L. Kang, B. G. Chung, R. Langer, and A. Khademhosseini. Microfluidics for drug discovery and development: from target selection to product lifecycle management. *Drug Discov Today*, 13(1-2):1–13, 2008.

[43] J. J. Agresti, E. Antipov, A. R. Abate, K. Ahn, A. C. Rowat, J.-C. Baret, M. Marquez, A. M. Klibanov, A. D. Griffiths, and D. A. Weitz. Ultrahigh-throughput screening in drop-based microfluidics for directed evolution. *Proceedings of the National Academy of Sciences*, 107(9):4004–4009, 2010.

[44] L. Mazutis, J. Gilbert, W. L. Ung, D. A. Weitz, A. D. Griffiths, and J. A. Heyman. Single-cell analysis and sorting using droplet-based microfluidics. *Nat Protoc*, 8(5):870–91, 2013.

[45] J. B. Haun, T.-J. Yoon, H. Lee, and R. Weissleder. Magnetic nanoparticle biosensors. *Wiley Interdisciplinary Reviews: Nanomedicine and Nanobiotechnology*, 2010.

[46] A. van Reenen, A. M. de Jong, J. M. den Toonder, and M. W. Prins. Integrated lab-on-chip biosensing systems based on magnetic particle actuation–a comprehensive review. *Lab Chip*, 14(12):1966–86, 2014.

[47] D. Issadore, Y. I. Park, H. Shao, C. Min, K. Lee, M. Liong, R. Weissleder, and H. Lee. Magnetic sensing technology for molecular analyses. *Lab Chip*, 14(14):2385–97, 2014.

[48] T. A. P. Rocha-Santos. Sensors and biosensors based on magnetic nanoparticles. *TrAC Trends in Analytical Chemistry*, 62:28–36, 2014.

[49] S. Schrittwieser, B. Pelaz, W. J. Parak, S. Lentijo-Mozo, K. Soulantica, J. Dieckhoff, F. Ludwig, A. Guenther, A. Tschope, and J. Schotter. Homogeneous biosensing based on magnetic particle labels. *Sensors (Basel)*, 16(6), 2016.

[50] A. Hrin, P. Kinnunen, Y. Li, M. A. Burns, and R. Kopelman. *Magnetic Particle Biosensors, book chapter in preparation.* 2016.

[51] Martin A. M. Gijs. Magnetic bead handling on-chip: new opportunities for analytical applications. *Microfluidics and Nanofluidics*, 2004.

[52] T. Jamshaid, E. T. T. Neto, M. M. Eissa, N. Zine, M. H. Kunita, A. E. El-Salhi, and A. Elaissari. Magnetic particles: From preparation to lab-on-a-chip, biosensors, microsystems and microfluidics applications. *TrAC Trends in Analytical Chemistry*, 79:344–362, 2016.

[53] G. Helgesen, P. Pieranski, and A. Skjeltorp. Nonlinear phenomena in systems of magnetic holes. *Physical Review Letters*, 64(12):1425–1428, 1990.

[54] B. McNaughton, R. Agayan, J. Wang, and R. Kopelman. Physiochemical microparticle sensors based on nonlinear magnetic oscillations. *Sensors and Actuators B: Chemical*, 121(1):330–340, 2007.

[55] B. H. McNaughton, K. A. Kehbein, J. N. Anker, and R. Kopelman. Sudden breakdown in linear response of a rotationally driven magnetic microparticle and application to physical and chemical microsensing. *The Journal of Physical Chemistry B*, 110(38):18958–18964, 2006.

[56] X. J. A. Janssen, A. J. Schellekens, K. van Ommering, L. J. van Ijzendoorn, and M. W. J. Prins. Controlled torque on superparamagnetic beads for functional biosensors. *Biosensors and Bioelectronics*, 24(7):1937–1941, 2009.

[57] P. Kinnunen, I. Sinn, B. H. McNaughton, D. W. Newton, M. A. Burns, and R. Kopelman. Monitoring the growth and drug susceptibility of individual bacteria using asynchronous magnetic bead rotation sensors. *Biosens Bioelectron*, 26(5):2751–5, 2011.

[58] A. Hecht, P. Kinnunen, B. McNaughton, and R. Kopelman. Label-acquired magnetorotation for biosensing: An asynchronous rotation assay. *J Magn Magn Mater*, 323(3-4):272–278, 2011.

[59] A. Hecht, A. A. Kumar, and R. Kopelman. Label-acquired magnetorotation as a signal transduction method for protein detection: aptamer-based detection of thrombin. *Anal Chem*, 83(18):7123–8, 2011.

[60] B. H. McNaughton, R. R. Agayan, R. Clarke, R. G. Smith, and R. Kopelman. Single bacterial cell detection with nonlinear rotational frequency shifts of driven magnetic microspheres. *Applied Physics Letters*, 91:224105, 2007.

[61] B. H. McNaughton, P. Kinnunen, R. G. Smith, S. N. Pei, R. Torres-Isea, R. Kopelman, and R. Clarke. Compact sensor for measuring nonlinear rotational dynamics of driven magnetic microspheres with biomedical applications. *Journal of Magnetism and Magnetic Materials*, 321(10):1648–1652, 2009.

[62] I. Sinn, P. Kinnunen, T. Albertson, B. H. McNaughton, D. W. Newton, M. A. Burns, and R. Kopelman. Asynchronous magnetic bead rotation (ambr) biosensor in microfluidic droplets for rapid bacterial growth and susceptibility measurements. *Lab Chip*, 11(15):2604–11, 2011.

[63] R. Elbez, B. H. McNaughton, L. Patel, K. J. Pienta, and R. Kopelman. Nanoparticle induced cell magneto-rotation: monitoring morphology, stress and drug sensitivity of a suspended single cancer cell. *PLoS One*, 6(12):e28475, 2011.

[64] Y. Li, D. T. Burke, R. Kopelman, and M. A. Burns. Asynchronous magnetic bead rotation (ambr) microviscometer for label-free dna analysis. *Biosensors (Basel)*, 4(1):76–89, 2014.

CHAPTER II

Droplet-based Microfluidic Viscometer

2.1 Introduction

The viscosity of chemical and biological fluids is an important material property. In industry, viscosities of polymers [1], paints [2], petroleum products [3], food products [4], therapeutic proteins [5], and fermentation products [6] are routinely monitored during production and transportation to maximize efficiency and cost effectiveness. In medical diagnostics, changes in viscosities of biological fluids such as blood [7], plasma [8], cerebrospinal fluid [9], pleural fluid [10], and amniotic fluid [11] are correlated with a range of diseases. In applications where continuous viscosity measurements are necessary, labor costs and sampling volume typically become prohibitively high. Therefore, characterization of viscosity is often limited to single-point measurements.

Recently, many miniaturized viscometers have been developed using microfabrication and microfluidic technology. One approach is to use a hydrophilic channel that measures the velocity of an imbibing fluid multiplied by the length of that fluid stream, a product that is correlated to the fluid's viscosity. [12] Another approach measures the position and curvature of co-flowing laminar streams and calculates the viscosity numerically from the geometry of the interface, the flow rates and the viscosity of the reference stream. [13, 14] Viscosity information can also be derived from

the rotational rates of particles under a driven field or by tracking their Brownian motion. [15–17] The above methods require sample volumes on the order of microliters per run. With the incorporation of droplet microfluidics, the requirement on sample volume is further reduced from the order of microliters to nanoliters. Livak-Dahl *et al.* developed a droplet-based viscometer by measuring the velocity of droplets through a constriction at an imposed pressure. [18] DeLaMarre *et al.* determined the viscosity of fluids within the range of 1-50 cP by measuring the volumetric ratio of spacing oil to aqueous droplets. [19] Note that the above methods require complex calculations and/or calibrations for viscosity measurements.

In droplet-based microfluidic systems, droplet generation is governed by a balance between the viscous force and the interfacial tension, and the relevant dimensionless number is the capillary number. [20–22] For droplet generation in the absence of jetting or thread formation, two models are often used. At a low capillary number, the mechanism for flow-rate controlled breakup proposed by Garstecki *et al.* relates the volume of the droplet to the ratio of the dispersed-phase to continuous-phase flow rate. [23–25] At a high capillary number, the shearing model developed by Thorsen *et al.* relates the radius of the droplet to the inverse of the capillary number (i.e., the volume of the droplet relates to the cube of the flow rate ratio at a constant dispersed-phase flow rate). [26] Although the models do not directly relate the volume of the droplets to their viscosity, the droplet viscosity influences the size of the droplet in several ways including changing the liquid flow rates or the capillary number. In the literature, contradictive conclusions on whether and how droplet size depends on viscosity of the dispersed phase have been found [25, 27, 28], which may be explained by differences in capillary number regimes, operating conditions (e.g. operated at constant flow rates or constant pressures) and device geometry for the various studies.

Here, we report a continuous droplet-based viscometer to measure viscosity from the size of the droplets. We employ a flow-focusing device geometry to generate

droplets under constant pressure. The viscosity of aqueous fluids is determined from the length of the droplets. While droplets are continuously generated in the device, the viscometer can measure viscosities continuously every 10 seconds or less, and the total sample consumption over an hour can be as low as 1 μl or less. This chapter was partially modified from the paper submitted to *Analytical Chemistry*: Yunzi Li, Kevin R. Ward, Mark A. Burns, "Viscosity measurements using microfluidic droplet length". [29]

2.2 Materials and Methods

2.2.1 Device Fabrication

Borofloat glass wafers (PG&O) were first annealed in a furnace (Tempress S6T1) at 560 °C for an hour, and Nano-Strip (Cyantek) cleaned. A 200 Å thick layer of Cr followed by 2000 Å thick layer of Au was deposited on the glass wafer as a masking layer for glass etching. The wafers were then spin-coated with 3 μm S1827 positive photoresist (MicoChem) and patterned using a photomask on a mask aligner (MA6, SUSS MicroTec). Subsequent development was conducted using AZ 726 developer, TFA gold etchant and CR-1020 chrome etchant (Transene). After removal of photoresist, the glass wafer was etched in 49% HF. Finally, the Cr and Au masking layers were removed using their corresponding etchants. The depth of the patterned channels was measured by a surface profilometer (Dektak XT, Bruker), and the widths of the channels were measured under a microscope (Nikon Eclipse Ti).

Another glass wafer was drilled to create access holes of the inlets and outlets. The two sides of the glass wafer were bonded to two dummy glass wafers for protection using Crystalbond 555 adhesives. The access holes were marked on the wafer and electro-chemically drilled in 50% NaOH (Sigma-Aldrich). After drilling, the adhesives were dissolved in water and the glass wafers with access holes were cleaned in buffered

HF for 30 minutes.

The glass wafer with patterned channels and the glass wafer with access holes were coated with 2 μm parylene-C to render them hydrophobicity (SCS PDS 2035CR). The two wafers were aligned and bonded at 230 °C for 30 minutes with a force of 5000 N (EVG 520IS). Finally, the wafer was diced on a dicing saw (ADT 7100) to yield individual devices, and inlet ports for tubing connections were created by gluing shoulder washers (McMaster-Carr) on top of the access holes using UV-curable glues (Norland Optical Adhesive 72). To seal the space between the edges of shoulder washers and tubings, cured polydimethylsiloxane (PDMS) pieces were cut and filled into the empty space.

2.2.2 Experimental Setup

Fluids were fed into the device at constant pressures through a custom-built pressure control system. Compressed air was fed into microcentrifuge tubes containing aqueous samples or oils through electronic pressure controllers (VSO-EP, Parker Hannifin), and the magnitudes of air pressures were controlled by a custom LabVIEW program. The pressures at the inlet of the tubes were measured using a digital pressure gauge (Druck). The fluids in the tubes were pumped into the device through PTFE tubings (inner diameter 0.022 inch, Cole-Parmer). The device was placed on an inverted microscope (Nikon Eclipse Ti) with a 10× objective lens, and recordings were made with a CCD camera (Q Imaging).

2.2.3 Sample Preparation

Glycerol (Sigma-Aldrich) and deionized water solutions with varying glycerol mass fraction were prepared for viscometer calibration. Light mineral oil with 5 wt% Abil EM 90 (Evonik Goldschmidt GmbH) and heavy mineral oil with 5 wt% Abil EM 90 were prepared and used as the continuous phase for droplet generation. The cell cul-

ture medium contains M9 minimal medium with 36 g/l glucose (2 mM $MgSO_4$, 0.1 mM $CaCl_2$, 33.7 mM Na_2HPO_4, 22 mM KH_2PO_4, 8.55 mM NaCl, 9.35 mM NH_4Cl, 3.6% glucose). Blood plasma were prepared from porcine whole blood using standard protocols. [30]

2.2.4 Viscosity Measurements

The viscosities of all aqueous solutions and oil/surfactant mixtures at 25 °C were measured on a cone-and-plate viscometer (AR1000, TA Instruments). The droplet-based microfluidic viscometer was used to measure the glycerol/water solutions. After connecting the oil reservoir to the chip, pressure was applied to the oil inlet to fill the channels with oil. Then, the aqueous sample was fed into the device and droplets were generated. Recordings and measurement were made after droplet generation become steady (typically in less than 1 minute). The image stacks were analyzed using ImageJ to measure the length and speed of the droplets, the spacing between two droplets and the generation time for one droplet.

2.3 Results and Discussion

2.3.1 Principle of the Droplet-based Viscometer

The droplet-based viscometer consists of a flow-focusing geometry for droplet generation and a narrow channel downstream for droplet measurement, as depicted in Figure 2.1. Oil and aqueous solutions are fed into the device at constant applied pressures, and the outlet of the device is open to atmospheric pressure. At the cross-junction, the aqueous phase is sheared and pinched by the oil phase and droplets form at a rate and size based on geometric dimensions and solution properties. The droplets generated at the cross-junction flow into the narrow downstream channel and adopt a discoid shape.

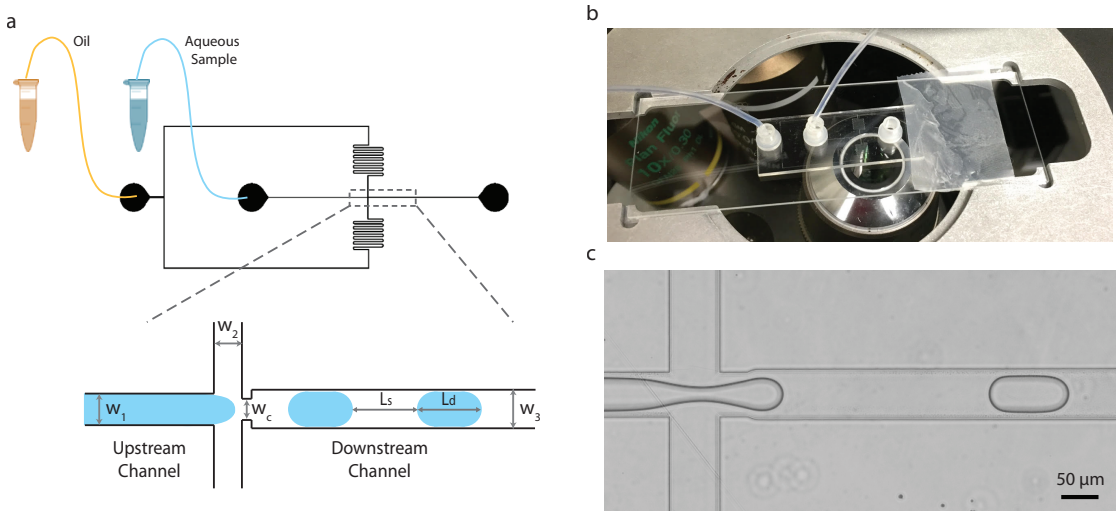

Figure 2.1: Viscometer design and set-up. (a) A schematic of device layout and operation. Oil (orange) and aqueous solutions (blue) are fed into the device at constant applied pressures. The length of the droplets (L_d) in the downstream channel is measured optically. Unless otherwise specified, the device has a channel depth of 22.5 μm, and $w_1 = w_c = 47.5\,\mu$m and $w_2 = w_3 = 55.0\,\mu$m. (b) A photo of the device set-up on an inverted microscope. (c) A photo of the cross-junction of the device.

At fixed operating pressures, the length of the droplet is directly affected by the viscosity of the aqueous solution and is independent of interfacial tensions between the two phases. As shown in Figure 2.2a and 2.2b, the droplet length decreases with increasing viscosity of glycerol/water solutions. The rate of decrease in droplet length as a function of solution viscosity eventually converges to a length that is comparable to the width of the channels. Interfacial tensions vary slightly with changes in solution viscosities (Fig. 2.2c), but no correlation is found between droplet length and interfacial tension. Similar results were observed by others. [23, 24, 31]

A calibration curve was constructed to calculate solution viscosities (μ_{aq}, viscosity of the aquesous phase) from droplet lengths. A linear relationship was found between μ_{aq} and $1/(L_d\text{-}L_c)$ and this relationship was verified with our theoretical derivation (See Theoretical Prediction of Droplet Lengths). Experimentally, we found that the length of the droplets converges to a minimal length at high μ_{aq} or at a low ratio of

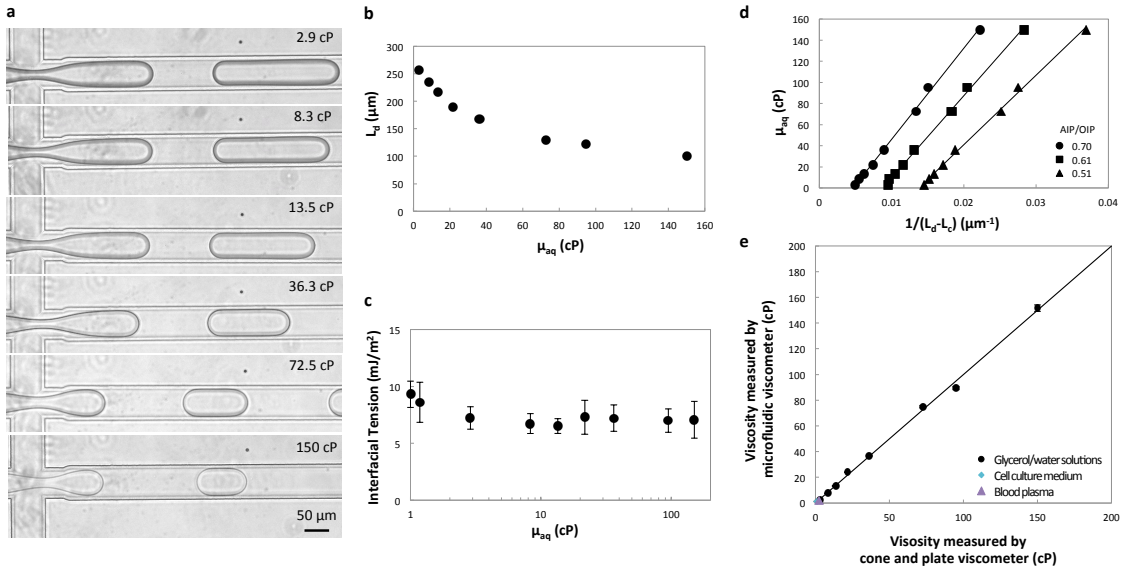

Figure 2.2: Viscometer calibration and viscosity measurements of Newtonian fluids. (a) Images of droplets with different viscosities generated in the device. (b) The length of droplets decreases with viscosity of droplets. The measurements were conducted at oil inlet pressure (OIP) of 3.17 psi and an applied pressure ratio (AIP/OIP) of 0.70. (c) Interfacial tension versus viscosity of the aqueous phase. The interfacial tensions were measured by axisymmetric drop shape analysis. The error bars represent the measurements of ten replicates. (d) The calibration curve relating the length of droplets to their viscosity. L_c is 55 μm in our system. (e) Comparison between the viscosities of Newtonian solutions measured by the microfluidic viscometer and those measured by a cone-and-plate viscometer. The error bars represent triplicates using the same device.

aqueous inlet pressure (AIP) to oil inlet pressure (OIP). Thus we define the minimal droplet length as L_c, and the values of L_c can be measured experimentally by decreasing the operating AIP/OIP. As shown in Figure 2.2d, a linear calibration curve was constructed at each AIP/OIP with L_c being the width of the downstream channel, a valve that proved accurate in most situations. This linear relationship is used to calculate solution viscosities from droplet lengths. The viscosities of Newtonian solutions (e.g. glycerol/water solutions with varying glycerol mass fraction, cell culture medium and blood plasma) measured by the droplet-based viscometer agree well with those measured by a cone-and-plate viscometer (Fig. 2.2e).

2.3.2 Sensitivity and Range of Viscosity Measurements

In order to generate droplets for viscosity measurements, the device needs to be operated within a range of applied pressure ratio (i.e., AIP/OIP). When the value of AIP/OIP is below a lower bound, the aqueous pressure is not high enough to inject the aqueous solution into the oil phase, and no droplets can be formed. Low AIP/OIP values fall into the retracting regime shown in Figure 2.3a. On the other hand, when AIP/OIP is beyond an upper bound, a thread instead of droplets is produced at the cross-junction, signifying the onset of the threading regime. Within the operating regime, the droplet size increases with AIP/OIP. The total flow rate (i.e., Q_{tot}) remains relatively constant except at high AIP/OIP close to the upper limit of the operable range (Fig. 2.3b). The range of operable pressure ratios is relatively constant for a given device geometry, with only a slight dependency on the viscosities of the two phases and OIP (Fig. 2.3c and 2.3d).

The sensitivity of the device to measure viscosity changes increases with AIP/OIP and decreases with viscosity ratio (i.e., μ_{aq}/μ_{oil}). As AIP/OIP increases, the slope of the droplet length versus viscosity curve increases (Fig. 2.4a), indicating an increase in sensitivity. In order to quantify the sensitivity, we can define the minimal detectable change in viscosity ($\Delta\mu_{aq}$) as

$$\Delta\mu_{aq} = \left|\frac{\partial L_d}{\partial \mu_{aq}}\right|^{-1} \Delta L_{min} \tag{2.1}$$

where ΔL_{min} is the minimum length that a microscope or other system can measure ($0.5\,\mu$m in our set-up). A low value of $\Delta\mu_{aq}$ indicates a high sensitivity. A calculation of $\Delta\mu_{aq}$ shows that $\Delta\mu_{aq}$ decreases with AIP/OIP for a given μ_{aq}/μ_{oil}, regardless of the magnitudes of AIP and OIP (Fig. 2.4b). Also, $\Delta\mu_{aq}$ increases with μ_{aq}/μ_{oil} at a fixed AIP/OIP (Fig. 2.4c).

The optimal operating AIP/OIP is a trade-off because, at high AIP/OIP, $\Delta\mu_{aq}$ is

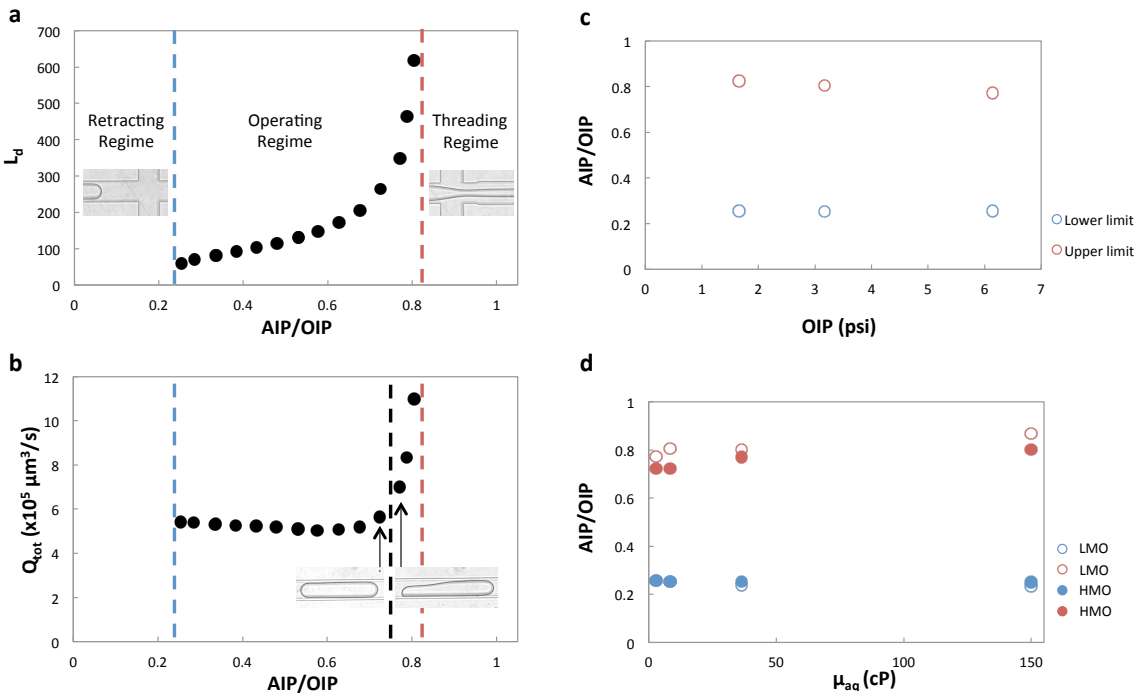

Figure 2.3: Effects of applied pressure ratio (AIP/OIP) on L_d and Q_{tot}. (a) The operable AIP/OIP range for droplet generation. The blue dashed line is the lower limit of AIP/OIP, and the red dashed line is the upper limit. The photos show droplet behavior in the retracting and threading regimes. (b) The total flow rate remains relatively constant at low to moderate AIP/OIP and increases at high AIP/OIP. The black dashed line indicates the optimal AIP/OIP. The photos show the shapes of droplets close to the outlet port of the device at the corresponding AIP/OIP. (c) The operable range of AIP/OIP decreases slightly with OIP. (d) The operable range of AIP/OIP increases slightly with μ_{aq}. The effect of oil-phase viscosity on the operable range is shown, where a light mineral oil (LMO, $\mu_{oil} = 37\,cP$) and a heavy mineral oil (HMO, $\mu_{oil} = 147\,cP$) were used.

low, but the droplet formation can become unstable resulting in unreliable viscosity measurements. We observed experimentally that the onset of droplet distortion is always accompanied by a sudden increase in Q_{tot} (Fig. 2.3b). At AIP/OIP below approximately 0.72, Q_{aq} increases and Q_{oil} decreases with AIP/OIP at a fixed OIP, so Q_{tot} remains relatively constant. Once AIP/OIP increases above 0.72, droplets closer to the outlet port are distorted in shape, and Q_{tot} rises as oil can flow around these droplets. As a result, the correlation of droplet length to aqueous phase vis-

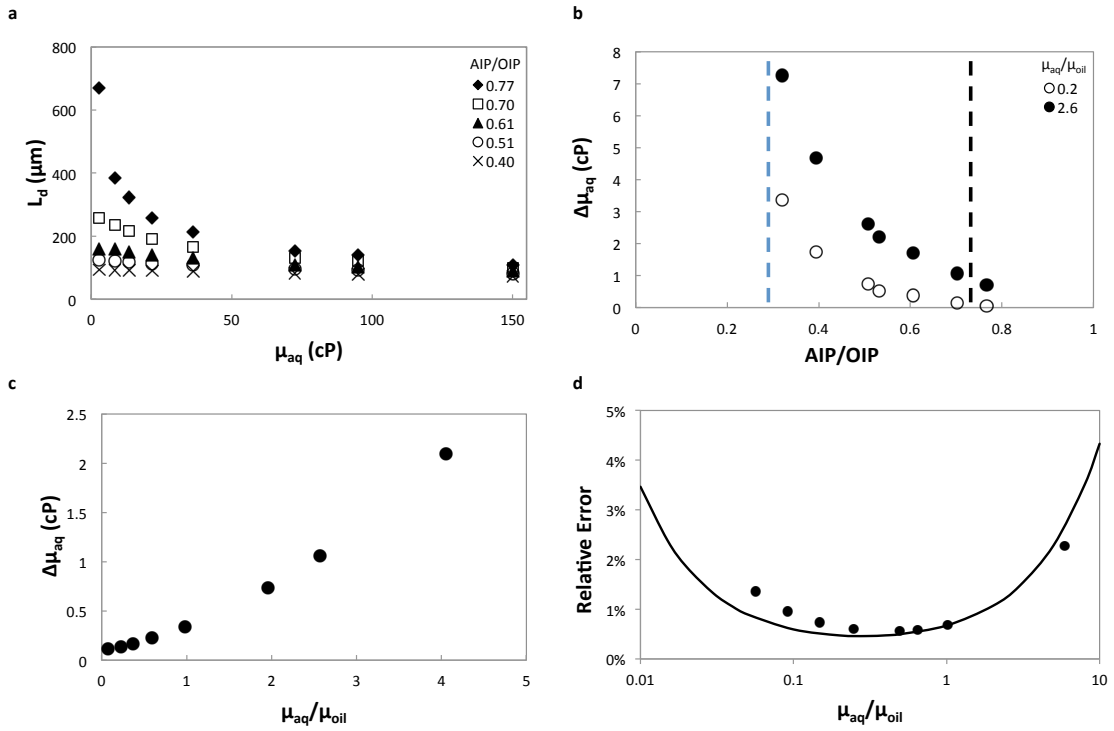

Figure 2.4: Sensitivity and range of viscosity measurements. (a) Droplet length versus viscosity at different AIP/OIPs. The derivatives of the curves increase with AIP/OIP, regardless of the absolute values of AIP and OIP. (b) The minimal detectable viscosity change ($\Delta\mu_{\mathrm{aq}}$) decreases with AIP/OIP. The blue and black dashed lines represent the lower limit and optimal value of AIP/OIP, respectively. (c) $\Delta\mu_{\mathrm{aq}}$ increases with the viscosity ratio. AIP/OIP is 0.70. (d) The relative error of viscosity measurements (i.e., $\Delta\mu_{\mathrm{aq}}/\mu_{\mathrm{aq}}$) versus the viscosity ratio. The points are relative error calculated from the experiment ($\mu_{\mathrm{oil}} = 147\,\mathrm{cP}$, AIP/OIP = 0.70) and the solid line is the theoretically predicted relative error.

cosity becomes tenuous. The viscometer should be operated at the highest AIP/OIP that does not produce observable droplet distortion. This optimal value of AIP/OIP increases with $\mu_{\mathrm{aq}}/\mu_{\mathrm{oil}}$ and decreases with $\mathrm{Q_{tot}}$ (Fig. 2.5).

The range and sensitivity of the viscometer can be altered by changing the viscosity of the oil phase. For a fixed oil-phase viscosity, as $\mu_{\mathrm{aq}}/\mu_{\mathrm{oil}}$ decreases, $\Delta\mu_{\mathrm{aq}}$ decreases (Fig. 2.4c). However, because μ_{aq} eventually decreases at a higher rate, the relative error of the viscosity measurement, defined as $\Delta\mu_{\mathrm{aq}}/\mu_{\mathrm{aq}}$, becomes more

significant. In addition, if μ_{aq}/μ_{oil} is very low, the droplets are more readily deformed (i.e., deformed at a lower AIP/OIP, Fig. 2.5a), as its viscosity is much less than the viscosity of the surroundings. Therefore, in order to measure viscosities with less than 5% relative error, the oil-phase viscosity should be chosen such that $0.01 < \mu_{aq}/\mu_{oil} < 10$ (Fig. 2.4d). For example, if μ_{aq} to be measured is approximately 850 cP, an oil-phase viscosity of 150 cP is preferred over 40 cP, because the more viscous oil would give a lower relative error for viscosity measurements (i.e., approximately 2% error for $\mu_{oil} = 150$ cP, and 10% error for $\mu_{oil} = 40$ cP).

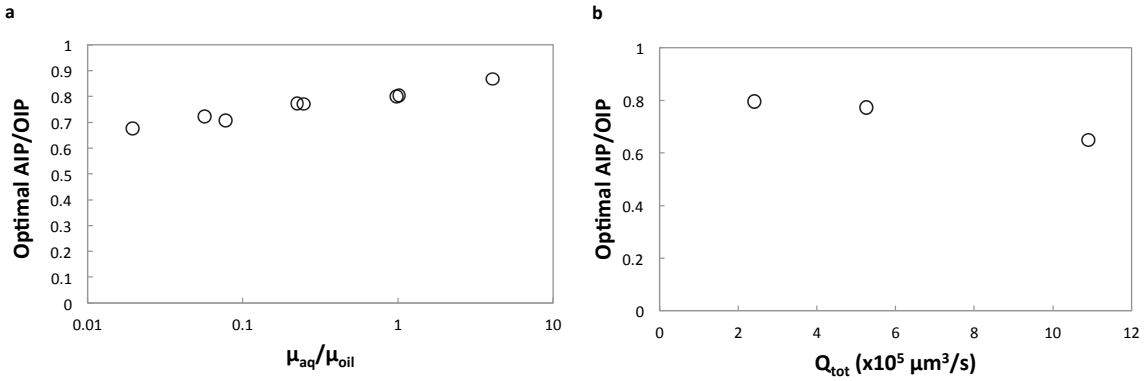

Figure 2.5: The influence of viscosity ratios and total flow rate on the optimal AIP/OIP. (a) The optimal AIP/OIP increases with μ_{aq}/μ_{oil}. (b) The optimal AIP/OIP decreases with Q_{tot}.

2.3.3 Theoretical Prediction of Droplet Lengths

The change in droplet length in response to viscosity changes is governed by the mechanism for flow-rate controlled breakup. For droplets that are forced to adopt a discoid shape in a narrow channel of constant cross-sectional area, the volume of the droplets is linearly proportional to their length. Garteski *et al.* showed that droplet generation in a T-junction geometry at low Reynolds and capillary numbers follows the equation [24]

$$\frac{L_d}{w_3} = 1 + \alpha \frac{Q_{aq}}{Q_{oil}} \tag{2.2}$$

where L_d is the length of the droplets, w_3 is the width of the downstream channel, α is a geometry-dependent constant on the order of 1, Q_{aq} is the flow rate of the aqueous phase, and Q_{oil} is the flow rate of the oil phase. In our viscometer, the droplets are generated in a flow-focusing geometry at low Reynolds ($Re \sim 10^{-1} - 10^{-2}$) and low capillary numbers ($Ca \sim 10^{-3} - 10^{-4}$). Experimentally, we found that the length of the droplets is linearly proportional to the flow rate ratio with α being approximately 1.5 (Fig. 2.6a).

In order to predict the droplet length using Equation 2.2, an expression for the flow rate ratio needs to be developed. The total pressure drop in the system can be written as a sum of the individual pressure drops, [22]

$$\Delta P_{applied} = \Delta P_{upstream} + \Delta P_{spacing} + \Delta P_{droplet} + \Delta P_{capillary} \tag{2.3}$$

The pressure drop in the upstream channel ($\Delta P_{upstream}$), the cumulative pressure drop of the spacing oil ($\Delta P_{spacing}$) and the cumulative pressure drop of the droplets ($\Delta P_{droplet}$) in the downstream channel are due to viscous dissipation of a single-phase fluid. These pressure drops can be calculated using the Hagen-Poiseuille law, [32]

$$\Delta P_i = k_i \mu_i Q_i \tag{2.4}$$

where ΔP_i, k_i, μ_i and Q_i are the pressure drop, geometric constant, viscosity and flow rate, respectively, in the corresponding channel i.

The discrete nonlinear capillary pressure drop ($\Delta P_{capillary}$) arises as a result of differences in curvature at the front and rear edges of the droplets. An exact expression of $\Delta P_{capillary}$ has not yet been developed for viscous droplets in a rectangular channel in the literature, but the study on viscous droplets in a tube by Teletke *et*

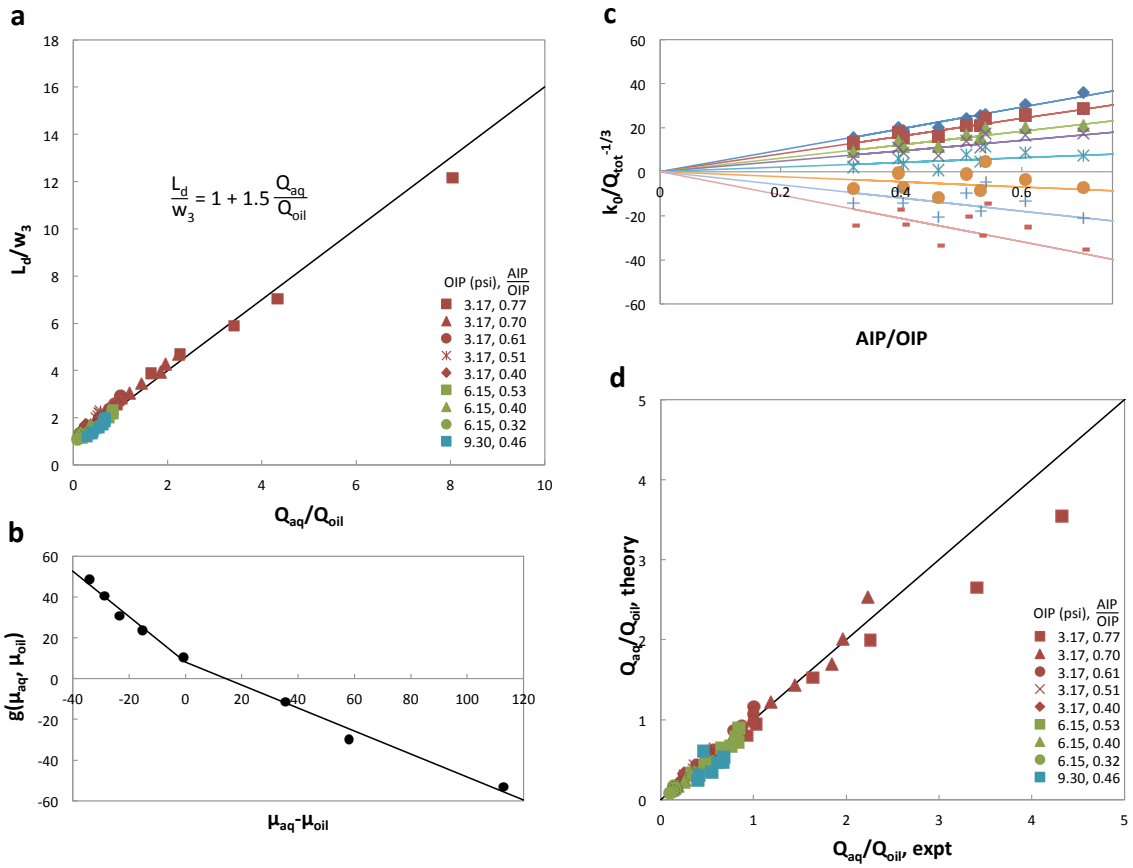

Figure 2.6: Experimental verification of theoretical relationship and fitting of coefficients. (a) The ratio of droplet length to the width of the downstream channel versus the flow rate ratio for different OIPs, AIP/OIPs and μ_{aq}. The solid line is the fitting line for Equation 2.2, where the geometry-dependent constant α is determined to be 1.5. (b) The plot of $g(\mu_{aq}, \mu_{oil})$ versus $\mu_{aq} - \mu_{oil}$. The lines show the results of curve fitting using Equation 2.12. The slope of the linear fitting is steeper when μ_{aq} is less than μ_{oil}. (c) The plot of $k_0/Q_{tot}^{-1/3}$ versus AIP/OIP. The lines show the results of curve fitting using Equation 2.11. (d) A comparison between the theoretically calculated Q_{aq}/Q_{oil} and the experimentally determined Q_{aq}/Q_{oil} for different viscosities of the aqueous solutions and operating pressures ($\mu_{oil} = 37\,cP$).

al. suggests, [33, 34]

$$\Delta P_{capillary} \propto f(\mu_{aq}, \mu_{oil}) N Q_{tot}^{2/3} \tag{2.5}$$

where N is the number of droplets in the downstream channel, and $f(\mu_{aq}, \mu_{oil})$ is

relatively constant and is a function of the viscosities of the two phases. Here, we define a k_0 such that,

$$\Delta P_{\text{capillary}} = k_0 N Q_{\text{tot}} \tag{2.6}$$

where k_0 is a constant that determines the capillary pressure drops for each viscous droplet at a given total flow rate.

Substituting Equations 2.4 and 2.6 into Equation 2.3, the ratio of applied pressure of the aqueous phase to that of the oil phase (AIP/OIP) becomes,

$$\frac{\text{AIP}}{\text{OIP}} = \frac{k_1 \mu_{\text{aq}} Q_{\text{aq}} + k_3 \mu_{\text{aq}} Q_{\text{aq}} + k_3 \mu_{\text{oil}} Q_{\text{oil}} + k_0 N (Q_{\text{aq}} + Q_{\text{oil}})}{k_2 \mu_{\text{aq}} Q_{\text{aq}} + k_3 \mu_{\text{aq}} Q_{\text{aq}} + k_3 \mu_{\text{oil}} Q_{\text{oil}} + k_0 N (Q_{\text{aq}} + Q_{\text{oil}})} \tag{2.7}$$

where k_1, k_2 and k_3 are the geometric constants of the upstream channel of the aqueous phase, the upstream channel of the oil phase and the downstream channel, respectively. Rearranging Equation 2.7, we have

$$\frac{Q_{\text{aq}}}{Q_{\text{oil}}} = \frac{A}{B - \frac{\text{AIP}}{\text{OIP}}} - C \tag{2.8}$$

where

$$A = \frac{(k_1 k_2 + k_2 k_3 + k_1 k_3)\mu_{\text{oil}} \mu_{\text{aq}} + k_1 \mu_{\text{aq}} k_0 N + k_2 \mu_{\text{oil}} k_0 N}{(k_3 \mu_{\text{aq}} + k_0 N)^2} \tag{2.9a}$$

$$B = 1 + \frac{k_1 \mu_{\text{aq}}}{k_3 \mu_{\text{aq}} + k_0 N} \tag{2.9b}$$

$$C = \frac{k_2 \mu_{\text{oil}} + k_3 \mu_{\text{oil}} + k_0 N}{k_3 \mu_{\text{aq}} + k_0 N} \tag{2.9c}$$

k_1, k_2, k_3 can be expressed as, [32]

$$k_i = \frac{12 L_i}{w_i h^3} [1 - \frac{192 h}{\pi^5 w_i} \sum_{n=1,3,5}^{\infty} \frac{1}{n^5} \tanh(\frac{n \pi w_i}{2h})]^{-1}, \text{where } i = 1, 2, 3 \tag{2.10}$$

where w_i and L_i are the width and length of the corresponding channel. k_0 is experimentally determined as,

$$k_0 = g(\mu_{aq}, \mu_{oil}) \frac{AIP}{OIP} Q_{tot}^{-1/3} \tag{2.11}$$

where

$$g(\mu_{aq}, \mu_{oil}) = -1.12(\mu_{aq} - \mu_{oil}) + 8.0,\ \mu_{aq} < \mu_{oil} \tag{2.12a}$$

$$g(\mu_{aq}, \mu_{oil}) = -0.56(\mu_{aq} - \mu_{oil}) + 8.0,\ \mu_{aq} > \mu_{oil} \tag{2.12b}$$

These expressions of $g(\mu_{aq}, \mu_{oil})$ were derived by fitting experimental data (Fig. 2.6b and 2.6c). Note that, combining Equations 2.6 and 2.11, $\Delta P_{capillary}$ is proportional to $Q_{tot}^{2/3}$ in agreement with Equation 2.5 developed theoretically by Teletke *et al.* The flow rate ratios predicted using Equation 2.8 agree well with the experimentally determined flow rate ratios (Fig. 2.6d), except at very high AIP/OIP (e.g. AIP/OIP > 0.72) when droplet distortion occurs.

The theoretically derived expression successfully predicts the length of droplets in our device, as shown in Figure 2.7a. The predictions were found by substituting Equations 2.8-2.12 into Equation 2.2, and the droplet lengths in our device can be predicted as long as the device geometry, oil-phase viscosity and operating pressures are known. The two variables that are not apparent from these input parameters are N and Q_{tot}. The number of droplets can be determined iteratively using

$$N = \frac{L_3}{L_d + L_s} = \frac{L_3}{L_d(1 + (\frac{Q_{aq}}{Q_{oil}})^{-1})} \tag{2.13}$$

where L_s is the length of spacing oil between two droplets, and L_3 is the length of the downstream channel. The total flow rate can be calculated using an empirical

Device #	h (μm)	w_1 (μm)	w_2 (μm)	w_3 (μm)	L_3 (μm)	oil viscosity (cP)
1	5	15	25	25	8000	37
2	22.5	47.5	55	55	8000	37
3	22.5	47.5	55	55	8000	147
4	22.5	47.5	55	55	4000	37
5	41	74	82.5	82.5	8000	37
6	44	80	88	88	8000	147
7	60	94	111	111	8000	37
8	175	230	230	230	8000	37

Table 2.1: A list of different device geometry and oil-phase viscosities used in the experiment. For all devices, L_1=7200 μm and L_2=49000 μm.

relationship that depends only on the experimental inputs,

$$Q_{tot} = \frac{10.8\,\mathrm{OIP}}{\mu_{oil}/(wh^3)} \tag{2.14}$$

where w is the width of the channels assuming all channels are comparable in width (i.e., $w \approx w_1 \approx w_2 \approx w_3$). Equation 2.14 holds true for different device geometry, oil-phase viscosities and operating pressures (Fig. 2.7b). A list of device geometry and oil-phase viscosities used in this experiment are tabulated in Table 2.1.

The linear calibration curve between the aqueous-phase viscosity and droplet length found experimentally can be verified with the theory. Substituting Equation 2.8 to Equation 2.2, we obtain a correlation between L_d and μ_{aq}, yet this theoretically derived relationship does not offer an explicit equation for viscosity calculation. Therefore, we simplified Equation 2.8 numerically by substituting averaged values of other experimental measurable into the equations in order to infer relationship between L_d and μ_{aq}. The numerical simplification implies a linear relationship

$$\mu_{aq} = m\frac{1}{L_d - L_c} + b \tag{2.15}$$

where m and b are two coefficients of the linear calibration curve determined by experimental fitting, and L_c is the minimal droplet length that the droplets converge to at

high μ_{aq} or at low AIP/OIP. The value of L_c can be predicted theoretically using a high value of μ_{aq}, or it can be measured experimentally by decreasing the operating AIP at a constant OIP. In general, L_c is comparable to the size of the downstream channel. Re-plotting Figure 2.4a with the axes being μ_{aq} and $1/(L_d - L_c)$, we found both experimental data and theoretical predictions follow linear relationships (Fig. 2.7c). The linear relationship can be used to calculate viscosities from the droplet lengths in our viscometer.

2.3.4 Design Considerations

The theoretical equations derived in the previous section can be used to guide the design of this type of droplet-based viscometer. As a first step, the channel depth of the device, h, should be estimated. According to Equation 2.10, the height of the channels has more of an effect in determining the geometric constants and channel resistance than the widths and lengths of the channels. In order to estimate h for a pair of applied pressures, we used the Hagen-Poiseuille equation. However, applying Equations 2.4 and 2.10 for the device assuming the device is filled with oils results in large errors because of the presence of aqueous droplets. Instead, we used the empirically found correlation Equation 2.14 to relate the input pressures to the channel resistance and total flow rate.

The total flow rate, Q_{tot}, should be chosen such that the frequency of reliable measurements of the viscometer is high enough to capture viscosity changes in the sample. To quantify the measurement frequency, we define the time interval between two consecutive viscosity measurements, t_0, to be the time it takes to fill the downstream channel with droplets of a new viscosity,

$$t_0 = \frac{w_3 L_3 h}{Q_{tot}} \tag{2.16}$$

Thus t_0 decreases with increasing Q_{tot} (Fig. 2.7d), indicating that a higher Q_{tot} results

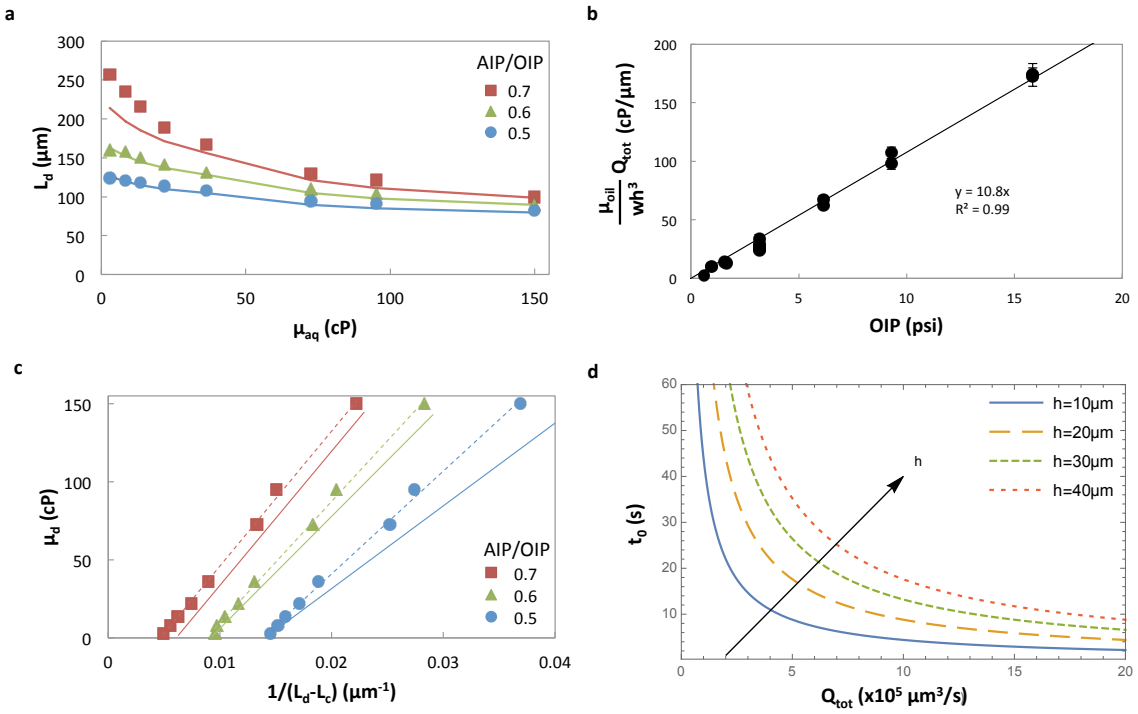

Figure 2.7: Theoretical prediction of droplet lengths and minimal time interval between two consecutive viscosity measurements. (a) The droplet length versus viscosity of the aqueous phase. The points are experimentally measured droplet lengths and the solid lines represent theoretically predicted droplet lengths. (b) $\mu_{oil}Q_{tot}/(wh^3)$ versus OIP falls onto one linear line for different operating pressures, different viscosities of the two phases, different channel depths and channel widths, assuming all channels in the device have comparable widths (i.e., $w_i \approx w_3$). The error bars represent the average of eight measurements of samples of different μ_{aq}. (c) The calibration curve relating the length of droplets to their viscosity. L_c is 55 μm for our system. The experimental data (indicated as points) follows linear relationship (indicated as dashed lines), and closely matches theoretical prediction (indicated as solid lines). (d) The predictive minimal time interval between two consecutive measurements t_0 versus the total flow rate in the device for different channel depths.

in a higher frequency of viscosity measurements. However, it is also noted that the benefit of increasing measurement frequency becomes less pronounced when Q_{tot} is more than 1×10^6 $\mu m^3/s$. Also, the relative error becomes significant at very high Q_{tot} because the optimal AIP/OIP decreases with Q_{tot} (Fig. 2.5b).

Rearranging Equation 2.16 for an expression for Q_{tot} and substituting it into

Equation 2.14, we have an expression of the channel depth assuming all channels have comparable widths,

$$h = \sqrt{\frac{\mu_{oil} L_3}{10.8\, t_0\, OIP}} \tag{2.17}$$

In this equation, μ_{oil} can be determined as discussed in Sensitivity and Range of Viscosity Measurements, t_0 is chosen to meet the requirement on measurement frequency and OIP is chosen based on the availability of the pressure sources and pressure regulators. Therefore, the channel depth can be estimated with a choice of L_3 (e.g. L_3=8000 μm in our device). Alternatively, if h is fixed due to fabrication limitations, Equation 2.17 can be rearranged and used to determine the operating pressure of the oil phase.

If two independently controlled applied pressure sources are available and there are no limitations on their values, different choices of widths and lengths of the upstream channels do not affect the relative error of viscosity measurements, though the optimal value of AIP/OIP might change. The geometric constants of the upstream channels change with the channel dimensions as predicted by Equation 2.10. If AIP and OIP can be adjusted to maintain the same flow rates as before the geometrical change, the relative error is expected to remain the same. The adjustment to the applied pressures can be predicted by applying the Hagen-Poiseuille equation to the upstream channels,

$$\Delta P_{aq} = (k_1' - k_1)\mu_{aq} Q_{aq} \tag{2.18a}$$

$$\Delta P_{oil} = (k_2' - k_2)\mu_{oil} Q_{oil} \tag{2.18b}$$

where ΔP_{aq} and ΔP_{oil} are the appropriate applied pressures changes, and k_1' and k_2' are the new geometric constants after the change. The boundary values of AIP/OIP for the operating regime and thus the optimal value of AIP/OIP may change, as the

applied pressures change according to Equation 2.18.

If only a certain range of applied pressures is available due to limitations of the pressure sources or regulators, the channel widths and lengths should be optimized to minimize the relative error of viscosity measurements. To study the effects of geometrical variation, we substituted Equation 2.8 into Equation 2.2 and calculated this error. As shown in Figure 2.8a, the relative error reaches a minimum when k_1 is approximately $0.1\,\mu m^3$ at the optimal AIP/OIP, implying a minimum of the relative error. With the optimal value of k_1, the width and length of the upstream channel of the aqueous phase could be determined using Equation 2.10. The dimensions of other channels are determined in comparison with the dimensions of the upstream channel of the aqueous phase. As shown in Figure 2.8b and 2.8c, the relative error decreases with k_2/k_1 and increases with k_3/k_1. Therefore, in order to minimize the relative error, the upstream channel of the oil phase should be longer and narrower than that of the aqueous phase, and the downstream channel should be comparable to the upstream channel of the aqueous phase. For example, we designed our device to have a k_1 value of approximately $0.1\,\mu m^3$, a k_2/k_1 value of 3 and k_3/k_1 value of 1.

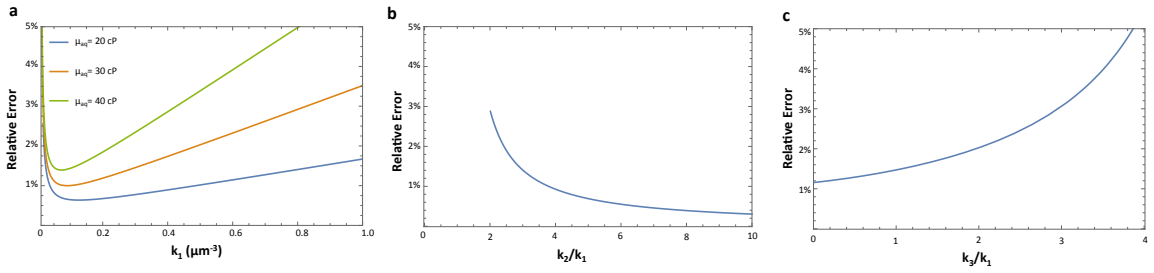

Figure 2.8: The effect of device geometry on viscosity measurements. Unless otherwise specified, the results are obtained for $\mu_{aq} = 21.7\,cP$, $\mu_{oil} = 37\,cP$ and AIP/OIP = 0.70. (a) The relative error of viscosity measurements versus the geometric constant of the upstream channel of the aqueous phase. (b) The relative error decreases with k_2/k_1. (c) The relative error increases with k_3/k_1.

In addition to choosing the channel dimensions to optimize the geometric con-

stants, other design factors should be taken into accounts, such as w_3/w_1 and the presence of the constriction. One unique advantage of our system to achieve high sensitivity for viscosity measurements is the ability to generate droplets of discoid shape at high AIP/OIP. At such high AIP/OIP, droplets adopt irregular shapes if a wide opening is present in the downstream channel (i.e., high w_3/w_1), making their volumes difficult to quantify. We also found experimentally that the optimal AIP/OIP decreases sharply with w_3/w_1, resulting in an increase in the relative error. For example, the optimal AIP/OIP decreases by approximately 50% due to the onset of droplet distortion if w_3/w_1 increases from 1 to 2 (only w_3 is varied), limiting the ability to be operated at high AIP/OIP. In our device, we used a w_3/w_1 value of 1. Moreover, the presence of a narrower constriction before the downstream channel increases the optimal AIP/OIP by approximately 25%, most likely through facilitating the pinching and break-up of the aqueous phase and stabilizing the droplet generation.

2.4 Conclusion

Our droplet-based viscometer provides a simple method to measure the viscosity of a sample using a very low sample volume. Theoretically, the sample volume of a single viscosity measurement equals the volume of one droplet, which is on the order of 1-100 pl. Experimentally, we used as low as 100 nl sample for viscosity measurements, which was limited by the minimal pipette volume. For continuous viscosity measurements, the viscometer can respond to a viscosity change on the order of seconds, and the total sample consumption over an hour can be less than 1 μl.

The viscometer could be used for reactions and analyses in solutions with significant viscosity changes. With a simple flow-focusing geometry design and pressure/vacuum operation, the viscometer is compatible with other large-scale and microfluidic processes. The thin oil layer between the sample and the channel wall protects the sample from cross-contamination, making the device also compatible

with biological applications. If the viscometer is connected to a batch reactor of a fermentation process, the progress of the reaction can be monitored by measuring the viscosity changes. The viscometer can also be integrated with droplet-based polymerization reactions to measure the viscosity of the reactant solutions and improve the uniformity and performance of the products. The viscosity changes in these reactions can be readily visualized from the lengths of the droplets, or alternatively be measured in real-time with an on-chip optical or capacitive sensor.

2.5 Bibliography

[1] J. M. Dealy and R. G. Larson. *Structure and rheology of molten polymers*. Hanser, Munich. 2006.

[2] W. K. Asbeck, D. D. Laiderman, and M. Van Loo. A high shear method of rating brushability of paints. *Journal of colloid science*, 7(3):306–315, 1952.

[3] D. W. Nagala and M. Boufaida. The importance of online viscosity measurement for leak detection and other simulation applications. pages 2267–2273. American Society of Mechanical Engineers.

[4] P. J. Cullen, A. P. Duffy, C. P. O'Donnell, and D. J. O'Callaghan. Process viscometry for the food industry. *Trends in Food Science & Technology*, 11(12):451–457, 2000.

[5] J. Jezek, M. Rides, B. Derham, J. Moore, E. Cerasoli, R. Simler, and B. Perez-Ramirez. Viscosity of concentrated therapeutic protein compositions. *Advanced drug delivery reviews*, 63(13):1107–1117, 2011.

[6] B. McNeil and L. M. Harvey. Viscous fermentation products. *Critical reviews in biotechnology*, 13(4):275–304, 1993.

[7] Jr. Holsworth, R. E., L. M. Shecterle, J. A. St Cyr, and G. D. Sloop. Importance of monitoring blood viscosity during cardiopulmonary bypass. *Perfusion*, 28(1):91–2, 2013.

[8] M. A. Elblbesy. Plasma viscosity and whole blood viscosity as diagnostic tools of blood abnormalities by using simple syringe method. *Medical Instrumentation*, 2(1):5, 2014.

[9] F. Yetkin, U. Kayabas, Y. Ersoy, Y. Bayindir, S. A. Toplu, and I. Tek. Cerebrospinal fluid viscosity: a novel diagnostic measure for acute meningitis. *Southern medical journal*, 103(9):892–895, 2010.

[10] O. Yetkin, I. Tek, A. Kaya, A. Ciledag, and N. Numanoglu. A simple laboratory measurement for discrimination of transudative and exudative pleural effusion: pleural viscosity. *Respir Med*, 100(7):1286–90, 2006.

[11] P. Rosati, P. Pola, P. Riccardi, R. Flore, P. Tondi, and U. Bellati. The use of ammiotic fluid viscosity measurements to establish fetal lung maturity. *International Journal of Gynecology & Obstetrics*, 35(4):351–355, 1991.

[12] N. Srivastava, R. D. Davenport, and M. A. Burns. Nanoliter viscometer for analyzing blood plasma and other liquid samples. *Analytical chemistry*, 77(2):383–392, 2005.

[13] P. Guillot, P. Panizza, J.-B. Salmon, M. Joanicot, A. Colin, C.-H. Bruneau, and T. Colin. Viscosimeter on a microfluidic chip. *Langmuir*, 22(14):6438–6445, 2006.

[14] D. E. Solomon and S. A. Vanapalli. Multiplexed microfluidic viscometer for high-throughput complex fluid rheology. *Microfluidics and Nanofluidics*, 16(4):677–690, 2013.

[15] I. Sinn, T. Albertson, P. Kinnunen, D. N. Breslauer, B. H. McNaughton, M. A. Burns, and R. Kopelman. Asynchronous magnetic bead rotation microviscometer for rapid, sensitive, and label-free studies of bacterial growth and drug sensitivity. *Anal Chem*, 84(12):5250–6, 2012.

[16] Y. Li, D. T. Burke, R. Kopelman, and M. A. Burns. Asynchronous magnetic bead rotation (ambr) microviscometer for label-free dna analysis. *Biosensors (Basel)*, 4(1):76–89, 2014.

[17] K. M. Schultz and E. M. Furst. High-throughput rheology in a microfluidic device. *Lab Chip*, 11(22):3802–9, 2011.

[18] E. Livak-Dahl, J. Lee, and M. A. Burns. Nanoliter droplet viscometer with additive-free operation. *Lab Chip*, 13(2):297–301, 2013.

[19] M. F. DeLaMarre, A. Keyzer, and S. A. Shippy. Development of a simple droplet-based microfluidic capillary viscometer for low-viscosity newtonian fluids. *Anal Chem*, 87(9):4649–57, 2015.

[20] G. F. Christopher and S. L. Anna. Microfluidic methods for generating continuous droplet streams. *Journal of Physics D: Applied Physics*, 40(19):R319–R336, 2007.

[21] T. Cubaud and T. G. Mason. Capillary threads and viscous droplets in square microchannels. *Physics of Fluids*, 20(5):053302, 2008.

[22] C. N. Baroud, F. Gallaire, and R. Dangla. Dynamics of microfluidic droplets. *Lab on a Chip*, 10(16):2032–2045, 2010.

[23] Piotr Garstecki, Irina Gitlin, Willow DiLuzio, George M. Whitesides, Eugenia Kumacheva, and Howard A. Stone. Formation of monodisperse bubbles in a microfluidic flow-focusing device. *Applied Physics Letters*, 85(13):2649, 2004.

[24] P. Garstecki, M. J. Fuerstman, H. A. Stone, and G. M. Whitesides. Formation of droplets and bubbles in a microfluidic t-junction-scaling and mechanism of break-up. *Lab Chip*, 6(3):437–46, 2006.

[25] Z. Nie, M. S. Seo, S. Xu, P. C. Lewis, M. Mok, E. Kumacheva, G. M. Whitesides, P. Garstecki, and H. A. Stone. Emulsification in a microfluidic flow-focusing device: effect of the viscosities of the liquids. *Microfluidics and Nanofluidics*, 5(5):585–594, 2008.

[26] T. Thorsen, R. W. Roberts, F. H. Arnold, and S. R. Quake. Dynamic pattern formation in a vesicle-generating microfluidic device. *Phys Rev Lett*, 86(18):4163–6, 2001.

[27] W. Lee, L. M. Walker, and S. L. Anna. Role of geometry and fluid properties in droplet and thread formation processes in planar flow focusing. *Physics of Fluids*, 21(3):032103, 2009.

[28] T. Fu, Y. Wu, Y. Ma, and H. Z. Li. Droplet formation and breakup dynamics in microfluidic flow-focusing devices: From dripping to jetting. *Chemical Engineering Science*, 84:207–217, 2012.

[29] Y. Li, K. R. Ward, and M. A. Burns. Viscosity measurements using microfluidic droplet length. *Analytical Chemistry*, submitted, 2016.

[30] A. Renshaw. *Henry's Clinical Diagnosis and Management by Laboratory Methods*. LWW, 2007.

[31] P. Garstecki, H. A. Stone, and G. M. Whitesides. Mechanism for flow-rate controlled breakup in confined geometries: a route to monodisperse emulsions. *Phys Rev Lett*, 94(16):164501, 2005.

[32] H. Bruus. *Theoretical microfluidics, Oxford master series in condensed matter physics*. Oxford University Press Oxford, 2008.

[33] Gary F. Teletzke, H. Ted Davis, and L. E. Scriven. Wetting hydrodynamics. *Revue de Physique Applique*, 23(6):989–1007, 1988.

[34] F. Jousse, G. Lian, R. Janes, and J. Melrose. Compact model for multi-phase liquid-liquid flows in micro-fluidic devices. *Lab Chip*, 5(6):646–56, 2005.

CHAPTER III

Analysis of Non-Newtonian Fluids using a Microfluidic Viscometer

3.1 Introduction

Non-Newtonian fluids, such as paint, ketchup, cornstarch, shampoo, and blood, are widespread in nature and in industry. [1–3] Understanding rheological properties of non-Newtonian fluids, in particular their viscosities, significantly improves production and transportation of the fluids in chemical and processing industry. Generally, non-Newtonian fluids demonstrate elasticity and their viscosities depend on shear rate or shear rate history. A common model to describe the viscosity dependency on shear rate is the two-parameter power law model.

To characterize the viscosity profile of non-Newtonian fluids, two major categories of viscometers are rotational viscometers and capillary viscometers. [1] Rotational viscometers, such as cone-and-plate viscometers, measure viscosities in a velocity-driven flow field. On the other hand, capillary viscometers, such as Ubbelohde viscometers, measure viscosities in a pressure-driven flow field. Therefore, an inherent advantage of the capillary viscometers is their ability to simulate the real flow field in tubular channels such as pipelines and blood vessels.

The introduction of microfluidic devices in 1980s opened the door to miniaturized

capillary viscometer. [4–6] Most of early microfluidic viscometers measure viscosities based on the Hagen-Poiseuille law or its variations, which relates the pressure drop of a single-phase fluid to the viscosity and flow rate of the fluid. [7, 8] These viscometers can be categorized to flow rate sensing viscometers [9–18] and pressure sensing viscometers [19–22]. One example is a self-calibrating viscometer developed by Srivastava *et al.* [9, 12] The viscometer tracks the front edge of an imbibing fluid, and measures the velocity and length of the traveling liquid column inside a microchannel to calculate the viscosity of the fluid. This method provides viscosity measurements of similar accuracy and precision using much less sample volumes (i.e., 600 nl) compared with traditional macroscale viscometers.

With the advances of droplet microfluidics, viscometers based on water-in-oil droplets emerged. Droplet-based viscometers demonstrate unique advantages over other existing microfluidic viscometers, which include extremely low sample volumes (30 nl or less), higher potential of process integration, capability of continuous operation and reusability of devices. Livak-Dahl *et al.* developed a method to quantify viscosity by measuring the velocity of a droplet in a narrow channel of high hydrodynamic resistance. [23] DeLaMarre *et al.* measured viscosity by correlating the solution viscosity to the ratio of droplet spacing to droplet length in a train of droplets in a narrow channel. [24] Despite of these promising designs, the development of droplet-based viscometer is still at its early stage, as it has not yet been proven that they can measure viscosities for all types of fluids, such as non-Newtonian fluids and highly viscous fluids.

In this work, we expand the applications of the previously developed droplet-based viscometer to non-Newtonian fluids. With a modification of the channel dimensions, we successfully measured viscosities of non-Newtonian fluids at different shear rates. The viscosity of aqueous fluids is calculated from the length of the droplets, and the shear rate is calculated from the flow velocity of the aqueous phase and power

law index of non-Newtonian fluids. The shear rates are readily adjusted by varying operating pressures. This is the first demonstration of a droplet-based microfluidic viscometer to assess viscosities of non-Newtonian fluids at different shear rates. This chapter was partially modified from the paper submitted to *Analytical Chemistry*: Yunzi Li, Kevin R. Ward, Mark A. Burns, "Viscosity measurements using microfluidic droplet length" [25].

3.2 Materials and Methods

3.2.1 Device Fabrication

The device was manufactured using standard photolithography and is detailed elsewhere. [25] Briefly, borofloat glass wafers (PG&O) were annealed at 560 °C and cleaned using Nano-Strip solutions. A masking metal layer (200 Å Cr/2000 Å Au) was deposited on top of the glass wafer, patterned using positive photoresist and etched using corresponding etchants. Then, the glass wafer was etched in 49% HF. The depth of the patterned channels was measured by a surface profilometer (Dektak XT, Bruker), and the widths of the channels were measured under a microscope (Nikon Eclipse Ti). Another glass wafer was drilled electrochemically to create access holes of the inlets and outlets, and cleaned in buffered HF for 30 minutes. The two glass wafers were coated with 2 μm parylene-C using physical vapor deposition method in order to modify the surface property of glass (SCS PDS 2035CR), and bonded at 230 °C for 30 minutes (EVG 520IS). Finally, the wafer was diced into individual devices, and inlet ports were created by gluing shoulder washers (McMaster-Carr) onto the access holes using UV-curable glues (Norland Optical Adhesive 72).

3.2.2 Sample Preparation

Light mineral oil with 5 wt% Abil EM 90 (Evonik Goldschmidt GmbH) was prepared and used as the continuous phase in the device. Glycerol (Sigma-Aldrich) and water were gently mixed at different ratios for viscometer calibration. Boger fluids were prepared by dissolving polyethylene glycol in glycerol solutions. Shear thinning fluids were prepared by dissolving Xanthan gum powder in deionized water or glycerol solutions. The polymer solutions were placed on a rotator at room temperature for a day to ensure complete dissolution before viscosity measurements.

3.2.3 Experimental Setup and Operation

Constant air pressures were applied to micro-centrifuge tubes containing aqueous samples or oils to feed the liquids into the device. The air pressures were controlled with a custom-built pressure control system, which includes electronic pressure controllers (VSO-EP, Parker Hannifin) and a LabVIEW user interface. A digital pressure gauge (Druck) is connected to a three-way valve to monitor the pressure at the inlet of the tubes.

To measure viscosities using the microfluidic viscometer, the following procedures were conducted. The oil phase was first fed into the device to fill all channels of the device. Then, the aqueous phase was introduced to generate droplets. To re-use the device for a second aqueous solution, air in the inlet tubing of the second solution assists in pushing the residual aqueous solution out of the aqueous channel/chamber, and the second aqueous solution is allowed to flow for approximately 2-4 minutes before taking any measurements. In parallel, viscosities of all liquids were also measured by a standard cone-and-plate viscometer.

The microfluidic device was set up on an inverted microscope (Nikon Eclipse Ti). After droplet generation reached a steady state (typically in less than 1 minute), the droplet motion in the center of the downstream channel was recorded with a CCD

camera (Q Imaging). The length and speed of the droplets and the spacing between two droplets were measured using ImageJ via image analysis.

3.3 Theory

3.3.1 Viscosity Calculations of Non-Newtonian Fluids

The viscosity of a fluid is measured by the size of the droplets generated in the droplet-based microfluidic viscometer. The length of the droplets (L_d) is correlated with the viscosity of the droplet (μ_{aq}, viscosity of the aqueous phase) through the relationship

$$\mu_{aq} = m\frac{1}{L_d - L_c} + b \tag{3.1}$$

where m and b are two coefficients determined by experimental fitting, and L_c is the minimal droplet length that the droplets converge to at high μ_{aq} or at a low ratio of aqueous inlet pressure (AIP) to oil inlet pressure (OIP). Experimentally, L_c can be readily measured by decreasing AIP at a constant OIP. The derivation of this relationship is detailed elsewhere. [25]

The linear relationship (Equation 3.1) is valid for various aqueous/oil systems, regardless of the material property of the two phases. For a given device geometry, the droplet generation in the low capillary number regime ($Ca \sim 10^{-3} - 10^{-4}$ in our system) is solely governed by the flow rate ratio of the two phases, thus largely independent of material property of the two phases. The viscosities of the two phases, however, can influence the length of the droplets by changing the flow rates, as predicted by the Hagen-Poiseuille equation.

3.3.2 Geometrical Design

In order to design the geometry of the upstream channels and the downstream channel, we conducted a pressure balance within the system to quantify the contribution of each channel to the total pressure loss. The pressure loss in the downstream channel can be further divided into three contributors, namely the cumulative pressure drop of the spacing oil ($\Delta P_{spacing}$) the cumulative pressure drop of the droplets ($\Delta P_{droplet}$), and the discrete nonlinear capillary pressure drop ($\Delta P_{capillary}$). Therefore, a pressure balance between the applied pressure ($\Delta P_{applied}$) and the pressure drops gives,

$$\Delta P_{applied} = \Delta P_{upstream} + \Delta P_{spacing} + \Delta P_{droplet} + \Delta P_{capilary} \tag{3.2}$$

where $\Delta P_{upstream}$ is the pressure drop in the upstream channel.

Each term in the right hand side of Equation 3.2 can be estimated in order to determine the relative contribution of each type of pressure drop, which will help identify the most significant section for shear rate calculations. $\Delta P_{upstream}$, $\Delta P_{spacing}$ and $\Delta P_{droplet}$ are due to viscous dissipation of a single-phase fluid, and can be calculated using the Hagen-Poiseuille equation,

$$\Delta P_i = k_i \mu_i Q_i \tag{3.3}$$

where ΔP_i, k_i, μ_i and Q_i are the pressure drop, geometric constant, viscosity and flow rate, respectively, in the corresponding channel i (i=1 for the upstream channel of the aqueous phase, i=2 for the upstream channel of the oil phase, i=3 for the downstream channel). The geometric constants are defined as,

$$k_i = \frac{12L_i}{w_i h^3}[1 - \frac{192h}{\pi^5 w_i} \sum_{n=1,3,5}^{\infty} \frac{1}{n^5} \tanh(\frac{n\pi w_i}{2h})]^{-1} \tag{3.4}$$

where w_i and L_i are the width and length of the corresponding channel, respectively,

and h is the depth of the channels. $\Delta P_{capillary}$ is caused by differences in curvature at the front and rear edges of the droplets, and can be expressed as,

$$\Delta P_{capilary} = k_0 N Q_{tot} \tag{3.5}$$

where k_0 is a constant signifying the capillary pressure drop per droplet at a given total flow rate.

The sensitivity of the viscometer can be improved by increasing k_2/k_1 or decreasing k_3/k_1. With Equations 3.2-3.5, the effects of geometric constants on the relative error of viscosity measurement can be determined. The derivations and results are detailed elsewhere. [25] Briefly, the relative error of measurements decreases with increasing k_2/k_1 or decreasing k_3/k_1. In general, a k_2/k_1 value of greater than approximately 2 and a k_3/k_1 value of less than 3 is a good starting point for design. Also, w_1 and w_3 are designed to be comparable in size so that the droplets generated on-chip are forced to adopt a discoid shape, which enables easy measurement of droplet size and also stabilizes droplet generation at high AIP/OIP.

3.3.3 Shear Rate Calculations for Power Law Fluids

The viscosity of a non-Newtonian fluid depends on the shear rate at which it is measured. The viscosity may decrease (shear thinning), increase (shear thickening) or remain constant (Boger fluids) with increasing shear rates. A common model to describe such behavior of a non-Newtonian fluid is the power law model,

$$\mu_{aq} = K\dot{\gamma}^{n-1} \tag{3.6}$$

where μ_{aq} is the viscosity of the aqueous fluid, K is the consistency index, $\dot{\gamma}$ is the shear rate, and n is the power-law index. For example, n is less than 1 for shear thinning fluids and greater than 1 for shear thickening fluids.

The shear rate experienced by a power law fluid can be quantified by the average flow velocity, the channel depth and the power-law index. For a slit channel geometry ($h << w$), the shear rate at the channel walls can be determined as, [12, 26]

$$\dot{\gamma} = \frac{6v_{aq}}{h}(\frac{2}{3} + \frac{1}{3n}) \tag{3.7}$$

where v_{aq} is average flow velocity of the aqueous phase in the upstream channel, and can be calculated from a flow rate balance of the aqueous phase between the upstream channel and the downstream channel,

$$v_{aq} = \frac{w_3}{w_1}\phi_{aq}v_d, \text{ where } \phi_{aq} = \frac{L_d}{L_d + L_s} \tag{3.8}$$

where v_d is the measured velocity of the droplets, ϕ_{aq} is the volumetric fraction of the aqueous phase inside the downstream channel, and L_s is the length of the spacing oil between two consecutive droplets. Substitute Equation 3.7 into Equation 3.6,

$$\mu_{aq} = K(\frac{6v_{aq}}{h}(\frac{2}{3} + \frac{1}{3n}))^{n-1} \tag{3.9}$$

Thus, the power-law index n can be determined experimentally by fitting μ_{aq} and v_{aq} into Equation 3.9 with a least squares method. Substitute Equation 3.8 into Equation 3.7, we have an expression of the shear rate in terms of experimental measurable,

$$\dot{\gamma} = \frac{6}{h}\frac{w_3}{w_1}\frac{L_d}{L_d + L_s}v_d(\frac{2}{3} + \frac{1}{3n}) \tag{3.10}$$

3.4 Results and Discussion

3.4.1 Viscometer Operation and Calibration

The microfluidic viscometer generates droplets on-chip and measures the length of the droplet in the downstream channel (Fig. 3.1) for viscosity calculation. The

viscometer uses a flow-focusing geometry for droplet generation, and the geometry of each channel is designed such that most of the pressure drop (approximately 70%-96% of the total pressure drop) occurs in the upstream channel of the aqueous phase. The aqueous phase and the oil phase are fed into the viscometer at constant operating pressures. Aqueous droplets form at the cross-junction, and adopt a discoid shape as they move into the narrow downstream channel. The length of the droplets is measured optically to determine the viscosity of the dispersed phase (i.e., the aqueous phase).

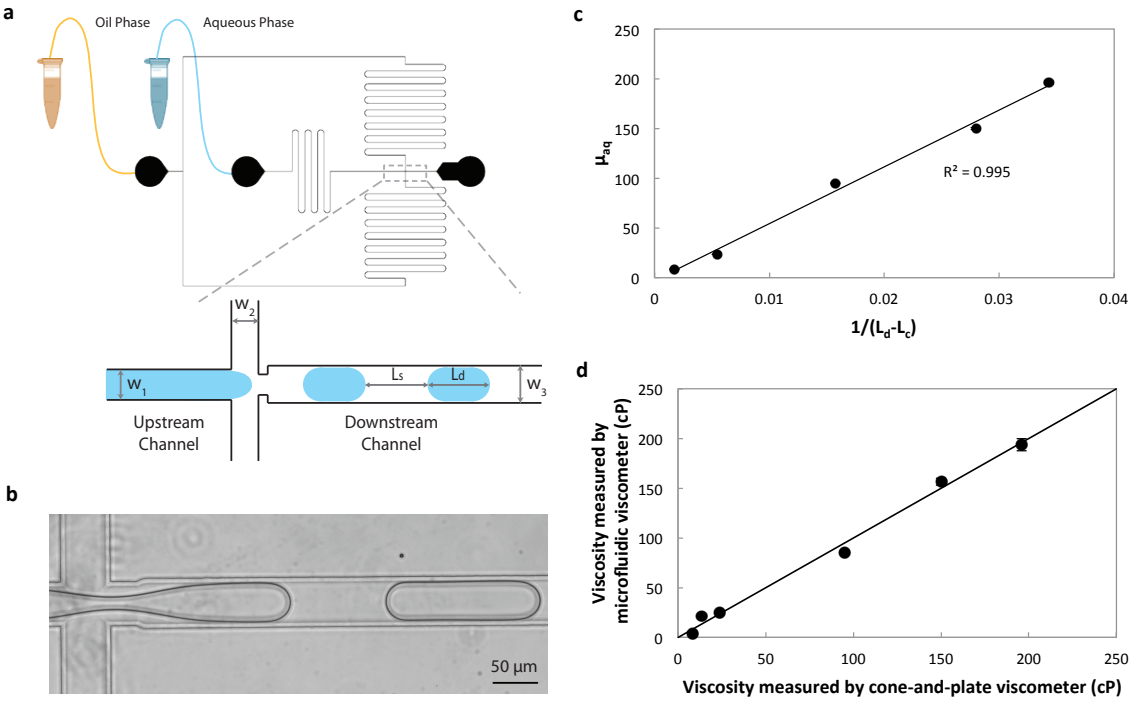

Figure 3.1: Viscometer calibration and characterization using Newtonian solutions (a) A schematic of device layout and operation. Fluids of the oil (orange) and aqueous (blue) phases are fed into the microfluidic viscometer at constant input pressures. A zoom-in view at the cross-junction depicts the droplet generation process. (b) A photo of droplet generation in the device under a microscope. (c) The calibration curve for viscosity calculation from the droplet length. L_c is the minimal droplet length, and determined to be 100 μm for our system. (d) Comparison between the viscosities measured by the microfluidic viscometer and the viscosities measured by a cone-and-plate viscometer.

The relationship between the viscosity of the aqueous phase (μ_{aq}) and the droplet length (L_d) is calibrated for viscosity calculation. Experimentally, it was observed that L_d decreases with increasing μ_{aq} and finally converges to a minimal droplet length (L_c). This change in L_d is governed by the mechanism of flow-rate controlled breakup at a low capillary number ($Ca \sim 10^{-3} - 10^{-4}$ in our system), and is largely independent of interfacial tensions as detailed in our earlier work. [25] As shown in Figure 3.1c, a linear calibration curve was constructed between μ_{aq} and $1/(L_d - L_c)$. This linear relationship is used for viscosity measurements. The viscosities of Newtonian solutions (e.g. glycerol/water solutions) measured by the droplet-based viscometer agree with those measured by a cone-and-plate viscometer (Fig. 3.1d).

3.4.2 Viscosity Measurements of Power Law Fluids

The shear rate at which the viscosity of a power law fluid is measured in our system depends on the velocity of the aqueous phase in the upstream channel (v_{aq}). The viscous dissipation in the upstream channel of the aqueous phase contributes most to the total pressure loss in the system, so the shear rate that the aqueous fluid experiences in this channel is most significant. The shear rate in this channel is strongly dependent on AIP, so its value can be varied by changing the input value of AIP. The OIP is adjusted accordingly to maintain a high AIP/OIP value so as to ensure a high sensitivity of viscosity measurements. It is worth noting that the shear rate also depends on the viscosity of the measured fluid, so the AIP required to achieve the same shear rate may vary from samples to samples. However, this would not influence the accuracy of viscosity measurements, because $\dot{\gamma}$ and μ_{aq} are independently determined from experimentally measured variables (i.e., v_{aq} and L_d, respectively).

The power law index and shear rate can be determined from experimentally measured variables. The power law index n can be determined by fitting Equation 3.9 to

a set of v_{aq} and v_{aq} values with the least squares method, where v_{aq} is calculated from experimentally measured v_d using Equation 3.8. The power law index of a Newtonian fluid (i.e., 87% glycerol) is calculated using this method to test the validity of the method. The value of n was found to be 1.05, very close to the expected value of n=1 (Fig. 3.2a). Once the power law index is known, the shear rate experienced by the power law fluid can be calculated using Equation 3.10.

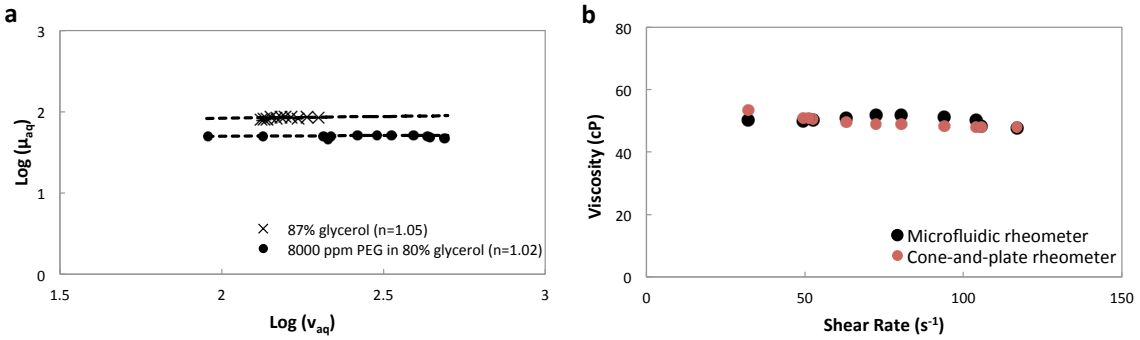

Figure 3.2: Viscosity and power law index measurements for Newtonian (87% glycerol) and Boger (8000 ppm PEG in 80% glycerol) fluids. The error bars represent triplicates using the same microfluidic device. (a) The plot of $\log(\mu_{aq})$ versus $\log(v_{aq})$. The dash lines indicate the fitted values using Equation 3.9. The values of n in the bracket are the power law index determined by the microfluidic viscometer. (b) Comparison between the viscosities measured by the microfluidic viscometer and those measured by the cone-and-plate viscometer at different shear rates.

To verify the validity of shear rate calculations and reliability of viscosity measurements for non-Newtonian fluids, the viscosities of a Newtonian fluid and a Boger fluid (i.e., non-Newtonian fluid with constant viscosity) were measured. The power-law indexes determined experimentally were 1.02 for the Newtonian fluid and 1.05 for the Boger fluid, very close to the expected value of $n = 1$ (Fig. 3.2a). The viscosities measured at different shear rates are constant as expected, which verifies the reliability of the viscosity measurements at different shear rates.

Viscosities of Boger and shear thinning fluids were measured using the droplet-based viscometer and compared with the viscosity values measured by a cone-and-

plate viscometer. The power law index of 8000 ppm PEG in 80% glycerol (a Boger fluid) was determined to be 1.02, as expected (Fig. 3.2b). The viscosities measured at different shear rates remain constant, and the values match those measured by the cone-and-plate viscometer. The power law index of 4000 ppm Xanthan gum (a shear thinning fluid) is found to be 0.34 using the droplet-based viscometer (Fig. 3.3a), close to the value of 0.30 as determined by the cone-and-plate viscometer (Fig. 3.3b). The viscosities of the shear thinning fluid measured by the droplet-base viscometer match well with those measured by the cone-and-plate viscometer, except at very low shear rates (Fig. 3.3c). The error may come from two sources: (1) the pressure controller used in our setup is less precise when operated at its lower limit (approximately 0.9 psi), which is evident in the large error bars at very low shear rates. (2) the error in determination of n causes error in the shear rate. Comparing Figure 3.3d with Figure 3.3c, the results match better if we use the n from the cone-and-plate viscometer for shear rate calculation.

3.4.3 Device Design for Constant Shear Rate Operation

Another geometry design of the viscometer can provide viscosity measurements at a constant shear rate for a wide range of viscosities at certain operating pressures. This is particularly useful for applications, such as monitoring reactions with a significant change in viscosities, where the absolute values of viscosities and shear rates are not necessarily important. In such designs, the ratios of k_2/k_1 and k_3/k_1 are high and changes in μ_{aq} do not cause significant changes in the ratio of the pressure drop in the upstream channel of the aqueous phase to the aqueous inlet pressure (i.e., $\Delta P_{upstream,aq}/AIP$). An example is a device with $k_2/k_1 = 3$ and $k_3/k_1 = 1$. This is contrary to the design when absolute values are important as described in the previous section, where the values of k_2/k_1 and k_3/k_1 are designed to be low.

Boger fluids and shear thinning fluids were measured in such systems where the

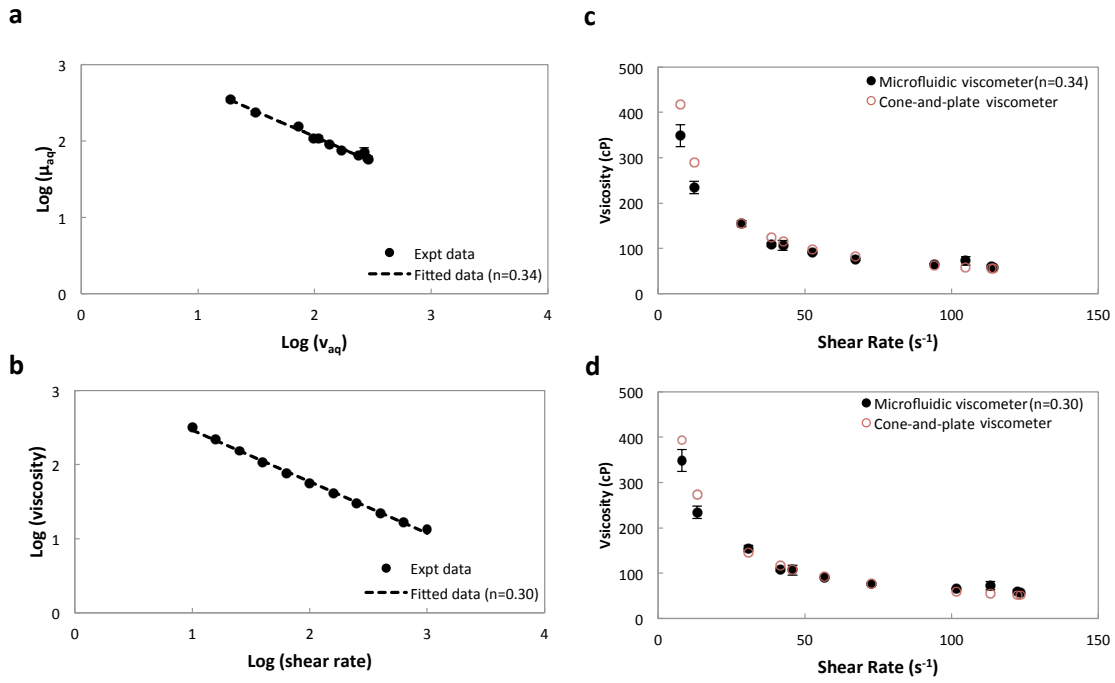

Figure 3.3: Viscosity and power law index measurements for shear thinning fluids (4000 ppm Xanthan gum). The error bars represent triplicates using the same microfluidic device. (a) The plot of of log(μaq) versus log(v_{aq}) using the microfluidic viscometer. (a) The plot of log(viscosity) versus log(shearrate) using the cone-and-plate viscometer. (c) Comparison of the viscosities measured by the microfluidic viscometer and the cone-and-plate viscometer at different shear rates, with the power law index determined from the microfluidic viscometer. (d) Comparison of the viscosities measured by the microfluidic viscometer and the cone-and-plate viscometer at different shear rates, with the power law index determined from the cone-and-plate viscometer.

pressure drops in the downstream channel is significant, with the shear rate estimated from the velocity of the droplets v_d. In this scenario, Equation 3.7 is no longer valid for shear rate calculation, because the fluid experiences different shear rates in different channels and an average shear rate needs to be used. Therefore, we estimated the shear rates with the equation $\dot{\gamma} = 6v_d/h$. This simple equation gives us an approximation of the orders of magnitude of the shear rates, which provides a tool to monitor viscosity changes when absolute values of viscosity are not necessary. We first used the device to measure viscosities of Boger fluids. The viscosities of

two different concentrations of Boger fluids measured by the microfluidic viscometer agree with the measurement by the cone-and-plate viscometer (Fig. 3.4a). We also measured viscosities of shear thinning fluids of different polymer concentrations over a shear rate range of two orders of magnitude. Using the equation for shear rate estimation, the viscosity versus shear rate profiles generally agree with the results by the cone-and-plate viscometer for polymer solutions of different concentrations and viscosities, although slight deviation is observed for polymer solutions of lower concentrations at lower shear rates (Fig. 3.4b). Note that we would anticipate an upper limit of measurable viscosities, because of the bead-on-a-string phenomenon for highly concentrated polymer solutions which prevents stable droplet generation. [27]

The shear rate is controlled by the operating pressure of the oil phase (i.e., OIP) and remains relatively constant upon changes in aqueous-phase input pressure and viscosity. As shown in Figure 3.4c, the shear rates vary from 50 to 250 s^{-1} by increasing OIP from 1.6 to 6.1 psi while keeping AIP/OIP constant. This result demonstrates that the shear rates can be changed by varying OIP. If increasing the AIP at a constant OIP, the shear rates do not vary much, with only a slight increase from 106 to 120 s^{-1} by increasing AIP/OIP from 0.4 to 0.75 at an OIP of 3.1 psi (Fig. 3.4d). Note that significant error at low AIP/OIP is due to low sensitivity of the viscometer. [25] According to the Hagen-Poiseuille equation, we would expect the shear rates would also be insensitive to μ_{aq} in the same fashion as to AIP. This can also be explained by the empirical relationship that we found in our earlier work [25], the total flow rate of the system is linearly proportional to OIP for a fixed device geometry, so the velocity of the droplets, thus the shear rate, is approximately constant for a given OIP and device geometry. Therefore, the viscometer can be used to monitor viscosity changes continuously at a relatively constant shear rate as long as OIP is kept constant throughout the measurement.

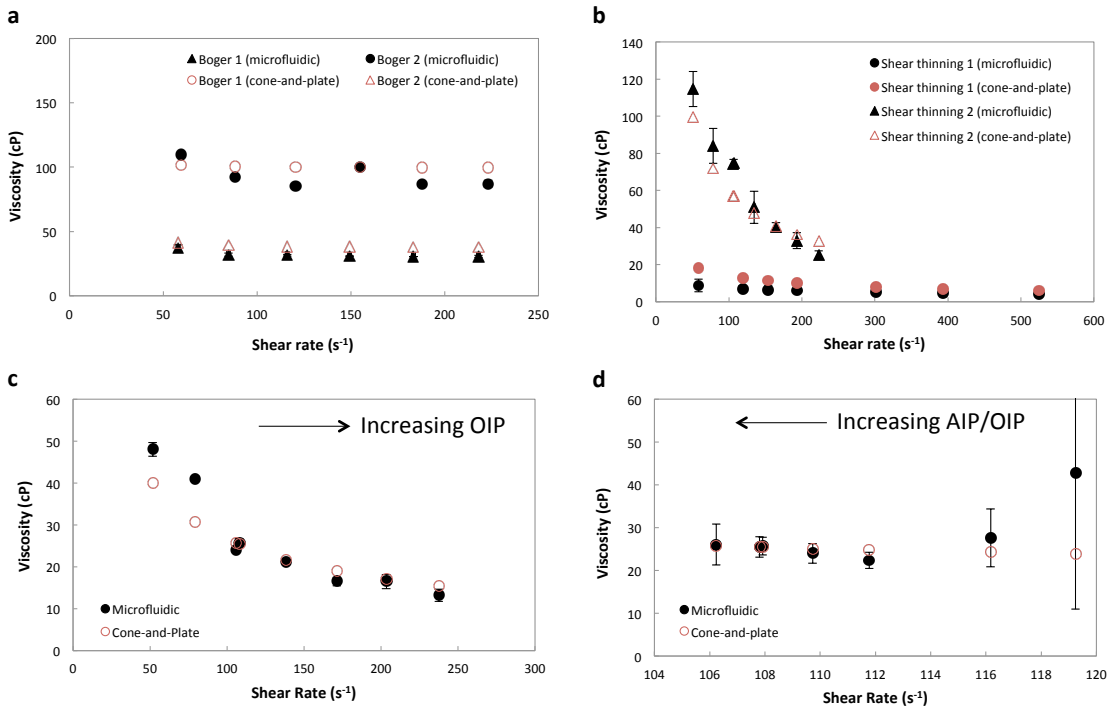

Figure 3.4: Viscosity measurements of non-Newtonian fluids using device with a geometry that is able to measure viscosity changes under a constant shear rate. Error bars represent triplicates using the same device. (a) Viscosity versus shear rate for Boger fluids. Boger 1: 8000 ppm Xanthan gum in 78% glycerol solution; Boger 2: 4000 ppm Xanthan gum in 87% glycerol solution. (b) Viscosity versus shear rate for shear thinning fluids. Shear thinning 1: 1000 ppm Xanthan gum solution; shear thinning 2: 4000 ppm Xanthan gum solution. (c) Viscosity versus shear rate for a shear thinning fluid (i.e., 2000 ppm Xanthan gum in 10% glycerol solution) at constant AIP/OIP. (d) Viscosity versus shear rate for a shear thinning fluid (i.e., 2000 ppm Xanthan gum in 10% glycerol solution) with increasing AIP at a constant OIP.

3.5 Conclusion

We have applied the previously developed microfluidic viscometer to measure viscosities of non-Newtonian fluids. To the best of our knowledge, this is the first droplet-based microfluidic viscometer capable of analyzing viscoelastic properties of non-Newtonian fluids. With a slight modification of the device geometry, the viscometer can either be used to measure absolute viscosities at different shear rates, or to monitor viscosity changes throughout the course of a reaction at a relatively con-

stant shear rate. The viscosity measurements span a shear rate range of at least two orders of magnitude and a viscosity range of up to three orders of magnitude. This microfluidic viscometer can be used to monitor viscosity changes, thus progression of biological reactions, in processes such as fermentation and blood coagulation.

3.6 Bibliography

[1] Raj P Chhabra and John Francis Richardson. *Non-Newtonian flow in the process industries: fundamentals and engineering applications*. Butterworth-Heinemann, 1999.

[2] Rajendra P Chhabra. *Non-Newtonian fluids: an introduction*, pages 3–34. Springer, 2010.

[3] M. A. Rao. *Rheology of fluid and semisolid foods: principles and applications: principles and applications*. Springer Science & Business Media, 2010.

[4] G. M. Whitesides. The origins and the future of microfluidics. *Nature*, 442(7101):368–73, 2006.

[5] R. Ahn, T. F. Burke, and A. M. McGahan. *Innovating for Healthy Urbanization*. Springer, 2015.

[6] E. Livak-Dahl, I. Sinn, and M. Burns. Microfluidic chemical analysis systems. *Annu Rev Chem Biomol Eng*, 2:325–53, 2011.

[7] C. J. Pipe and G. H. McKinley. Microfluidic rheometry. *Mechanics Research Communications*, 36(1):110–120, 2009.

[8] S. Gupta, W. S. Wang, and S. A. Vanapalli. Microfluidic viscometers for shear rheology of complex fluids and biofluids. *Biomicrofluidics*, 10(4):043402, 2016.

[9] N. Srivastava, R. D. Davenport, and M. A. Burns. Nanoliter viscometer for analyzing blood plasma and other liquid samples. *Analytical chemistry*, 77(2):383–392, 2005.

[10] J. Lee and A. Tripathi. Intrinsic viscosity of polymers and biopolymers measured by microchip. *Analytical Chemistry*, 77(22):7137–7147, 2005.

[11] G. Degré, P. Joseph, P. Tabeling, S. Lerouge, M. Cloitre, and A. Ajdari. Rheology of complex fluids by particle image velocimetry in microchannels. *Applied Physics Letters*, 89(2):024104, 2006.

[12] N. Srivastava and M. A. Burns. Analysis of non-newtonian liquids using a microfluidic capillary viscometer. *Analytical chemistry*, 78(5):1690–1696, 2006.

[13] P. Guillot, P. Panizza, J.-B. Salmon, M. Joanicot, A. Colin, C.-H. Bruneau, and T. Colin. Viscosimeter on a microfluidic chip. *Langmuir*, 22(14):6438–6445, 2006.

[14] Y.-Y. Lin, C.-W. Lin, L.-J. Yang, and A.-B. Wang. Micro-viscometer based on electrowetting on dielectric. *Electrochimica Acta*, 52(8):2876–2883, 2007.

[15] Z. Han, X. Tang, and B. Zheng. A pdms viscometer for microliter newtonian fluid. *Journal of Micromechanics and Microengineering*, 17(9):1828–1834, 2007.

[16] X. Tang and B. Zheng. A pdms viscometer for assaying endoglucanase activity. *Analyst*, 136(6):1222–6, 2011.

[17] S. D. Hudson, P. Sarangapani, J. A. Pathak, and K. B. Migler. A microliter capillary rheometer for characterization of protein solutions. *J Pharm Sci*, 104(2):678–85, 2015.

[18] D. E. Solomon, A. Abdel-Raziq, and S. A. Vanapalli. A stress-controlled microfluidic shear viscometer based on smartphone imaging. *Rheologica Acta*, 55(9):727–738, 2016.

[19] K. Kang, L. J. Lee, and K. W. Koelling. High shear microfluidics and its application in rheological measurement. *Experiments in Fluids*, 38(2):222–232, 2005.

[20] C. J. Pipe, T. S. Majmudar, and G. H. McKinley. High shear rate viscometry. *Rheologica Acta*, 47(5-6):621–642, 2008.

[21] J. Chevalier and F. Ayela. Microfluidic on chip viscometers. *Rev Sci Instrum*, 79(7):076102, 2008.

[22] L. Pan and P. E. Arratia. A high-shear, low reynolds number microfluidic rheometer. *Microfluidics and Nanofluidics*, 14(5):885–894, 2013.

[23] E. Livak-Dahl, J. Lee, and M. A. Burns. Nanoliter droplet viscometer with additive-free operation. *Lab Chip*, 13(2):297–301, 2013.

[24] M. F. DeLaMarre, A. Keyzer, and S. A. Shippy. Development of a simple droplet-based microfluidic capillary viscometer for low-viscosity newtonian fluids. *Anal Chem*, 87(9):4649–57, 2015.

[25] Y. Li, K. R. Ward, and M. A. Burns. Viscosity measurements using microfluidic droplet length. *Analytical Chemistry*, submitted, 2016.

[26] C.W. Macosko. *Rheology: principles, measurements, and applications*. VCH, 1994.

[27] L. Derzsi, M. Kasprzyk, J. P. Plog, and P. Garstecki. Flow focusing with viscoelastic liquids. *Physics of Fluids*, 25(9):092001, 2013.

CHAPTER IV

Whole Blood and Blood Coagulation Analysis

4.1 Introduction

Abnormality in blood coagulation (e.g. bleeding or clotting disorders) is a major cause of morbidity and mortality worldwide. In the field of urgent care, for example, uncontrollable bleeding caused by coagulopathy (i.e., coagulation abnormality) is a major cause of preventable death. More than 5 million people die from trauma every year, accounting for 9% of global annual mortality. [1–3] Coagulopathy, along with acidosis and hypothermia, is often referred to as the "trauma triad of death" because of its high mortality. At least one-fourth of trauma patients suffer from coagulopathy. [4–6] In addition, there are over 1 million cases of sepsis per year resulting in over 250,000 deaths. [7, 8] Coagulopathy is a major complication of sepsis and leads to rapid death. Fortunately, these deaths are preventable if early diagnosis and prevention/treatment of coagulopathy are provided to the patients. [6, 9]

Although efforts have been made to identify biochemical or biophysical indicators of abnormality in blood coagulation and develop commercial assays and tools, complete understanding of blood coagulation is lacking and a reliable predictive indicator is still missing. The current routine coagulation assays, such as prothrombin time/international normalized ratio (PT/INR), optically measures the clotting time of an activated blood plasma at the body temperature. This method provides no

information on the clot evolution and breakdown and generally does not use whole blood for the diagnosis, thus limiting its ability to diagnose a broader range of coagulation abnormalities. [10] The viscoelasticity-based tests, such as thromboelastography (TEG) and rotational thromboelastometry (ROTEM), assess the clot firmness during the entire coagulation process after clot formation, but the poor reproducibility and reliability rendered them unacceptable for clinical purposes. [11, 12] Furthermore, both types of tests cannot monitor any changes in blood before blood clots form.

A promising method to diagnose abnormality in blood coagulation is to monitor viscosity changes during blood coagulation. Changes in viscosity are known to be a marker of general inflammation effecting coagulation. [13] Evaluation of whole blood viscosity at sites of severe atherosclerotic obstructions or sites of blood vessel injuries provides vital information in diagnosis. For example, when a blood vessel is damaged, cascades of biochemical reaction occur, triggering the formation of fibrin polymers, and eventually form blood clots. [14] Therefore, the viscosity of whole blood increases due to the formation of fibrin polymers and clots of cell aggregates, and decreases as the clots gradually dissolve over time. Detecting dynamic viscosity changes represents a new blood vital sign linked to inflammation and coagulation. This nexus is critical in large disease cohorts ranging from trauma and sepsis, to chronic inflammatory disease states (e.g. diabetes and hypertension). Development of this platform will enable rapid assessment of an important coagulation parameter not yet made accessible.

In this work, we used a microfluidic viscometer to measure viscosities of whole blood and monitor blood coagulation process. With the previously developed droplet-based microfluidic viscometer, we measured viscosities of banked blood that were stored for different duration. We also monitored blood coagulation for up to 1 hour, consuming only less than $5\,\mu$l citrated whole blood. The effects of temperature and shear rate on blood clotting were analyzed, and a tendency towards hypercoagulability

was observed at higher temperatures and at higher shear rates. Using the microfluidic viscometer, we were able to detect the onset of blood coagulation and clot formation earlier than commercial viscoelastic-based tests, such as TEG.

4.2 Materials and Methods

4.2.1 Device Fabrication

The device is made of glass and fabricated with photolithography techniques, which is detailed elsewhere. [15] Briefly, borofloat glass wafers (PG&O) were pre-treated by annealing and subsequently cleaning. For the channel layer, a metal mask (200 Å Cr/2000 Å Au) was deposited and patterned. Then, the channels were etched in 49% HF and their depth was measured by a surface profilometer (Dektak XT, Bruker). For the cover layer, another glass wafer was drilled electrochemically and cleaned to create holes for inlet and outlet ports. The two glass wafers were bonded at 230 °C for 30 minutes (EVG 520IS) via a hydrophobic parylene-C layer. Inlet and outlet ports were made by gluing shoulder washers (McMaster-Carr) onto the drilled holes.

For devices with on-chip capacitive sensors, similar fabrication protocols were used except that the access holes were drilled on the glass wafers with channels and the gold electrodes were patterned on the cover wafer. To protect the channels during the drilling process, the channel side of the glass wafer was bonded to a dummy wafer using Crystalbond 555 adhesives. The cover glass wafer was patterned using positive photoresist, and a metal layer (200 Å Cr/1000 Å Au) was deposited on top of the patterned photoresist. The gold electrodes were fabricated using life-off method (1 hour sonication in acetone). The two glass wafers were then aligned (SUSS MicroTec MA-BA-6 Mask-Bond Aligner) and bonded (EVG 520IS).

4.2.2 Sample Preparation

The continuous phase (i.e., the oil phase) was prepared by gently mixing 5 wt% Abil EM 90 (Evonik Goldschmidt GmbH) with light mineral oil. Glycerol (Sigma-Aldrich) and water solutions used for device calibration were prepared similarly. Porcine whole blood was drawn into citrate tubes containing 3.2% sodium citrate (Becton Dickinson) from healthy animals and used within 2 hours of blood collection. The blood was kept at room temperature and re-calcified with $CaCl_2$ (Haemonetics, 20 μl 0.2 M $CaCl_2$ in 340 μl whole blood) immediately before experiment. Blood plasma and blood serum were prepared from porcine whole blood using standard protocols. [16] Segments of banked blood (approximately less than 300 μl per segment) were obtained from UM hospital. Each segment was from a different donor.

4.2.3 Experimental Setup and Operation

Constant air pressures were applied to feed aqueous- and oil-phase liquids into the device. The applied pressures were controlled by a custom-built pressure control system and measured by a digital pressure gauge (Druck). The microfluidic device was set up on an inverted microscope (Nikon Eclipse Ti). When measuring viscosity changes during blood coagulation at 37 °C, a heated glass insert (Tokai Hit) was placed on the microscope stage under the microfluidic device to maintain the temperature during viscosity measurements. During blood coagulation, the motion of droplets in the downstream channel was recorded with a CCD camera (Q Imaging). The length, speed and grayscale intensity of the droplets were analyzed via ImageJ.

For device automation using on-chip capacitive sensors, AD7746 capacitance-to-digital converter and a USB microcontroller that comes with AD7746 in the evaluation kits (Analog Devices) were used. The electrode pads on the microfluidic viscometer and the ports of the microcontroller were connected with wires.

4.2.4 Experimental Controls

The viscosities of aqueous samples were measured by a cone-and-plate viscometer (AR1000, TA Instruments). For measurement of banked blood viscosity using the cone-and-plate viscometers, 2 or 3 segments of blood from different donors were mixed to increase the total sample volumes, as a minimum volume of approximately 1 ml is required for the cone-and-plate viscometer. All measurements were conducted at room temperature. Blood coagulation of citrated whole blood was also monitored using a commercial viscoelastic-based equipment (TEG 5000 Thrombelastograph Hemostasis Analyzer) at room temperature and at 37 °C. The hematocrit percentages of banked blood were measured by a blood analyzer (ABL800 FLEX Radiometer).

4.3 Results and Discussion

4.3.1 Viscosity Measurements of Blood

As detailed in our earlier work [15], we have developed a droplet-based microfluidic viscometer (Fig. 4.1a). The viscometer measures the length of the droplets L_d generated on-chip, and determines the aqueous-phase viscosity μ_{aq} by a linear calibration relationship between μ_{aq} and $1/(L_d - L_c)$, where L_c is the minimal droplet length and is comparable to the width of the downstream channel. The shear rate experienced by the aqueous phase is approximately by $6v_d/h$, where v_d is the velocity of the droplets and h is the depth of the microfluidic channels. Using the microfluidic viscometer, we measured viscosities of blood plasma and blood serum, both of which can be considered shear-rate independent within our range of interests (on the orders of $10^1 - 10^3\,s^{-1}$). As shown in Figure 4.1b, the viscosities measured by the microfluidic viscometer agree with viscosities measured by a cone-and-plate viscometer.

Viscosities of banked blood of various storage duration from different donors were measured and compared, and no obvious viscosity changes were observed for banked

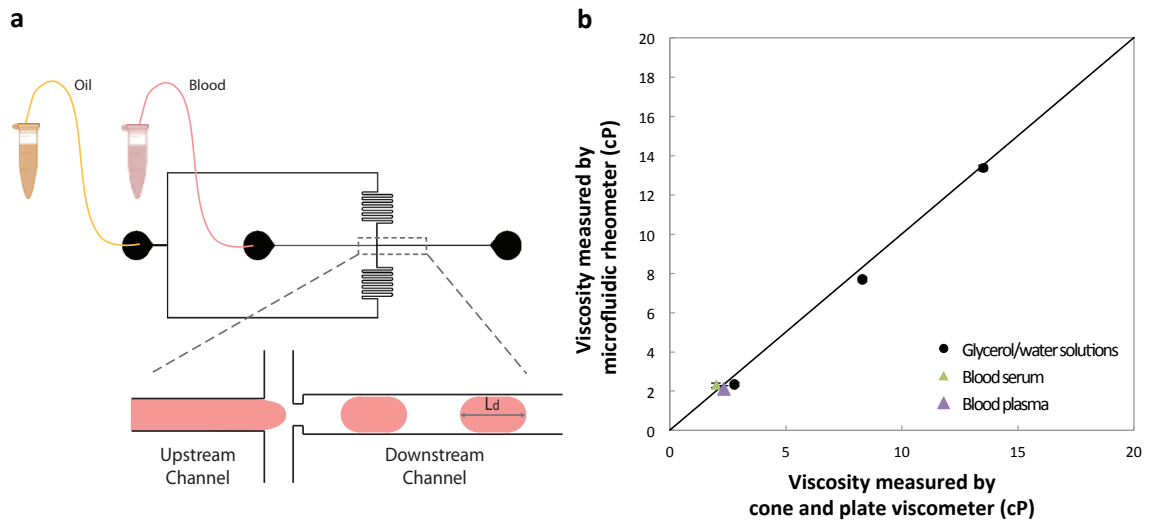

Figure 4.1: The use of droplet-based viscometer to measure viscosity of blood and blood products. (a) A schematic of device layout and operation. Oil (orange) and blood (red) are fed into the device and generate blood droplets at the cross-junction. The length of the droplets L_d is measured for viscosity measurements. (b) Comparison of the viscosities of glycerol/water solutions, blood plasma and blood serum measured by the microfluidic viscometer and a cone-and-plate viscometer. The error bars represent triplicates using the same device.

blood within the shelf life of 42 days. We measured a total of 48 samples of banked blood of different storage lengths from 48 different donors. As shown in Figure 4.2a, the viscosities of banked blood vary from 6 to 13 cP at a shear rate of approximately $70\,s^{-1}$, with no clear dependency of viscosities on the storage duration. At a lower shear rate of approximately $30\,s^{-1}$, the viscosities span from 12 to 22 cP, with only a slight increasing trend of viscosities with increasing storage duration, if there is any at all (Fig. 4.2b). These viscosity values are comparable to the viscosities measured by a cone-and-plate viscometer (Fig. 4.2c). Comparing Figure 2c with Figure 2a and 2b, similar trends within the shelf life of 42 days were observed that blood viscosities at $80\,s^{-1}$ remain relatively constant and blood viscosities at 20-40 s^{-1} increases slightly, despite of a sharp increase in viscosity after the shelf life. Note that the viscosities measured by the cone-and-plate viscometer are prone to an error of on the orders of

1 cP due to the limited amount of blood samples available. To evaluate the reason of wide dispersion of blood viscosities from different donors observed in Figure 4.2a and 4.2b, we measured the hematocrit percentages (i.e., percentages of red blood cells), yet the hematocrit percentages are relatively constant among different blood samples and no dependency of viscosity variation on the hematocrit percentages can be found (Fig. 4.2d).

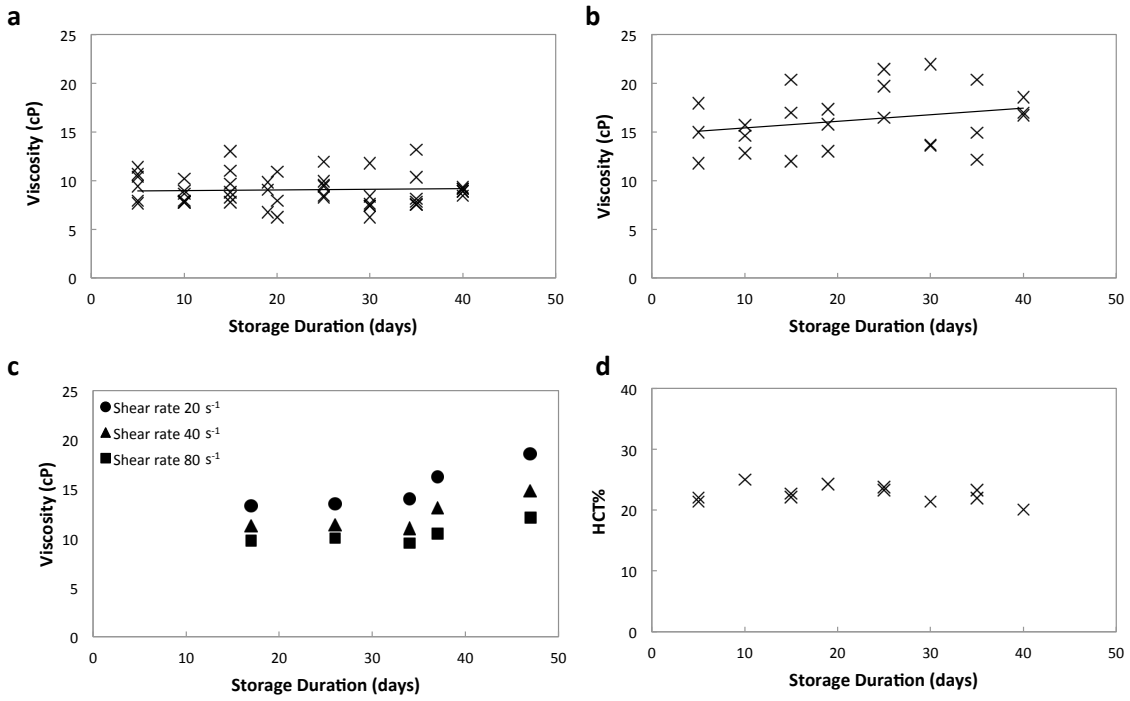

Figure 4.2: Analysis of banked blood of different storage duration. Each data point is from blood of a different donor. (a) Viscosities of banked blood of different storage lengths measured by the microfluidic viscometer at a shear rate of approximately $70\,s^{-1}$. A total of 48 samples were measured. (b) Viscosities of banked blood of different storage lengths measured by the microfluidic viscometer at a shear rate of approximately $30\,s^{-1}$. 24 samples were measured. (c) Viscosities of banked blood of different storage lengths measured by a cone-and-plate viscometer at different shear rates. 2-3 samples of the same storage length were mixed for each measurement. The measurement were conducted a week after the measurements by the microfluidic viscometer (the storage duration is adjusted accordingly). (d) The hematocrit percentages (HCT%) of banked blood. 12 out of the 48 samples were randomly selected and measured.

4.3.2 Monitoring Viscosity Changes of Blood Coagulation

The microfluidic viscometer was used to monitor viscosity changes during blood coagulation. Recalcification of citrated whole blood triggers the initiation of blood coagulation, and viscosity changes due to coagulation reaction over time were measured using the microfluidic viscometer. As shown in Figure 4.3a, the droplet size decreases sharply at the beginning, and then gradually increases. Accompanying the increase in droplet sizes at the later stage, the color of the droplets becomes significantly lighter, suggesting a gradual depletion of red blood cells (Fig. 4.3b). The viscosity, which was calculated from the droplet length, increases and peaks at approximately 7 minutes, and then decreases to reach a plateau. As a comparison, the control group without recalcification does not undergo blood coagulation, so the viscosity remains constant at 3-4 cP. Based on these experimental observations, we hypothesized that the first inflection point at the 5th minute signifies the onset of clotting reactions such as fibrin polymerization and cell recruitment, and the peak point at the 7th minute signifies the formation of a blood clot. The initial gradual increase in viscosity may be due to thrombin and fibrin production (0-5 minutes). The viscosity reduction after clot formation implies an increase in clot firmness, because more red blood cells are trapped in the blood clots, thus lower viscosity of the liquid phase.

The microfluidic viscometer is more sensitive and consumes less blood sample for blood coagulation monitoring than commercial tools such as TEG. As shown in Figure 4.3c, the microfluidic viscometer detects viscoelastic changes due to coagulation reaction earlier than TEG. TEG measures the firmness of blood clots only after clot formation, as the clots couple the oscillatory motions of the pin and cup. [17] Therefore, TEG reports no signals during the initial stages of fibrin formation and blood cell recruitment before clot formation, thus less sensitive than the viscosity-based detection by the microfluidic viscometer. The onset of clot formation in TEG measurement is described by the R time, which is the time to reach a significant TEG amplitude

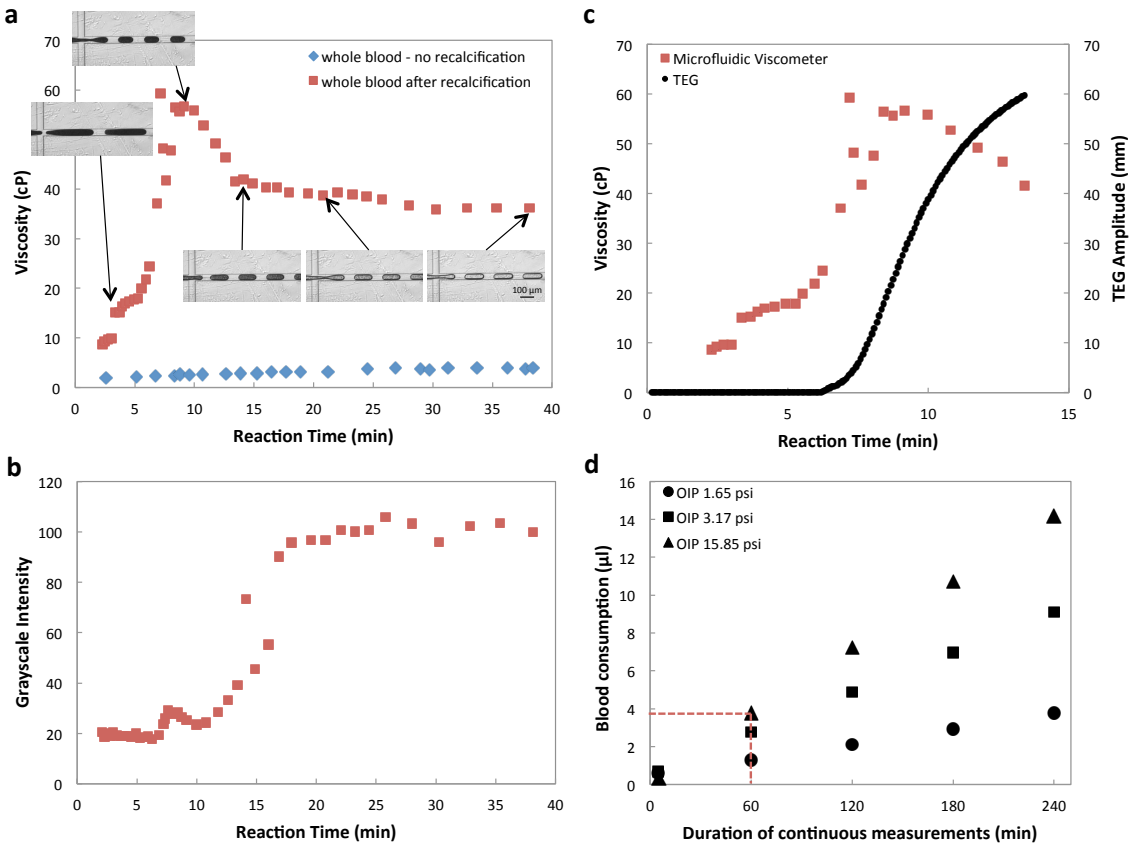

Figure 4.3: Blood coagulation measurements of citrated porcine whole blood. (a) Viscosity changes of citrated blood with (red) and without (blue) recalcification over time. The blood undergoes blood coagulation after recalcification. The viscosities were measured at room temperature and a shear rate of approximately $20\,s^{-1}$. The photo inserts show the size and color of the droplets at the pointed time. The scale bar shows the length of $100\,\mu m$. (b) The grayscale intensity of recalcified blood droplets over time. A higher intensity indicates a lighter color of the droplets. (c) Comparison of blood coagulation measurements between the microfluidic viscometer and TEG. (d) Total blood consumption over time at different oil inlet pressures (OIPs).

after the initial period of latency, approximately at 9 minutes in Figure 4.2c. To compare the microfluidic viscometer with TEG, we define the first inflection point at the 5th minute in Figure 4.2a as the onset of clotting reaction, and the peak at the 7th minute in Figure 4.2a as the onset of clot formation. We measured 10 blood samples from different animals within the first hour after blood collection at 25 °C using the

	25 °C (10 repeats each)		37 °C (5 repeats each)	
	Onset of Clotting Reaction (minutes)	Onset of Clot Formation (minutes)	Onset of Clotting Reaction (minutes)	Onset of Clot Formation (minutes)
Microfluidic viscometer	6.3 ± 4.6	11.9 ± 4.8	1.2 ± 1.7	7.3 ± 3.1
TEG	-	13.7 ± 4.5	-	9.5 ± 4.0

Table 4.1: Comparison of microfluidic viscometer and TEG at different temperatures. The standard deviations represent measurements of 10 blood samples from different animals at 25 °C, and measurements of 5 blood samples at 37 °C. All blood samples were analyzed by the microfluidic viscometer and TEG at approximately the same time within 1 hour of blood collection.

microfluidic viscometer and TEG, and another 5 blood samples at 37 °C. As shown in Table 4.1, we consistently observed that the microfluidic viscometer detects the time of clot formation approximately 2 minutes earlier than TEG. Note that the large standard deviations are due to the use of blood from different animals on different days, but the standard deviations of measurements by the microfluidic viscometers are similar to those by TEG. The total blood consumption over 1 hour is less than 5 μl, much less than 340 μl required by TEG (Fig. 4.3d).

4.3.3 Effects of Temperature, Shear Rate and Blood Storage on Blood Coagulation

The viscosity changes during blood coagulation at different temperatures and different shear rates were measured and compared with TEG. As shown in Figure 4.4a and 4.4b, blood coagulation was accelerated at a higher temperature, resulting in shorter time to initiate clotting reaction and clot formation. In other words, the citrated whole blood tends to be more hypercoagulable at higher temperature. This result is in agreement with TEG. In addition, we monitored blood coagulation at different shear rates, which is not measurable by TEG. The viscosities of whole blood are lower at higher shear rates, owing to its shear thinning behavior. The onset of

clot formation is shorter and the blood is more hypercoagulable at higher shear rates.

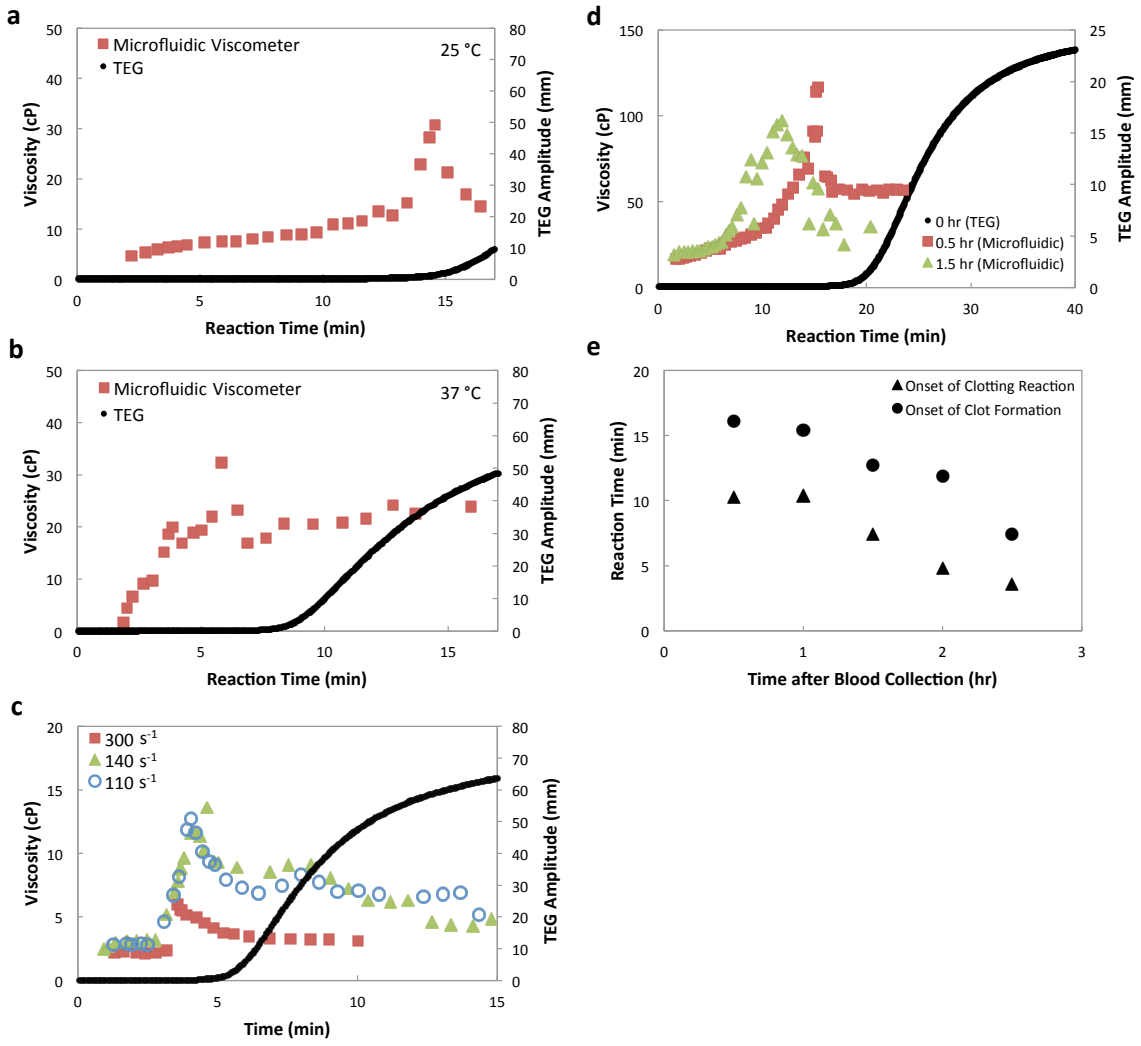

Figure 4.4: Effects of temperatures, shear rates and storage lengths of citrated whole blood on reaction kinetics of blood coagulation. Comparison of blood coagulation monitoring by the microfluidic viscometer and TEG at (a) 25 °C and approximately 50 s^{-1}; (b) 37 °C and approximately 60 s^{-1}; (c) 25 °C and approximately 110, 140 and 300 s^{-1}. (d) Monitoring blood coagulation process by the microfluidic viscometer with citrated whole blood 0.5 hour and 1.5 hours after blood collection. (e) Onsets of clotting reaction and clot formation using blood of different storage time measured by the microfluidic viscometer.

Although it has been generally considered reliable and acceptable to use citrated whole blood within 2 hours of blood collection based on TEG results [18, 19], we

found that reaction kinetics of blood coagulation started to change after 1 hour of blood collection using the microfluidic viscometer. As shown in Figure 4.4d, the onset of clot formation is approximately 4 minutes earlier using blood 1.5 hour after blood collection than using blood 0.5 hour after collection. The onsets of clotting reaction and clot formation remain relatively unchanged within the first hour, but become earlier in time with blood stored 1 hour or longer (Fig. 4.4e). This result is in agreement with findings in the literature that citrated whole blood becomes more hypercoagulable with increasing storage time. However, the cut-off time is found to be 1 hour, instead of the generally accepted 2 hours.

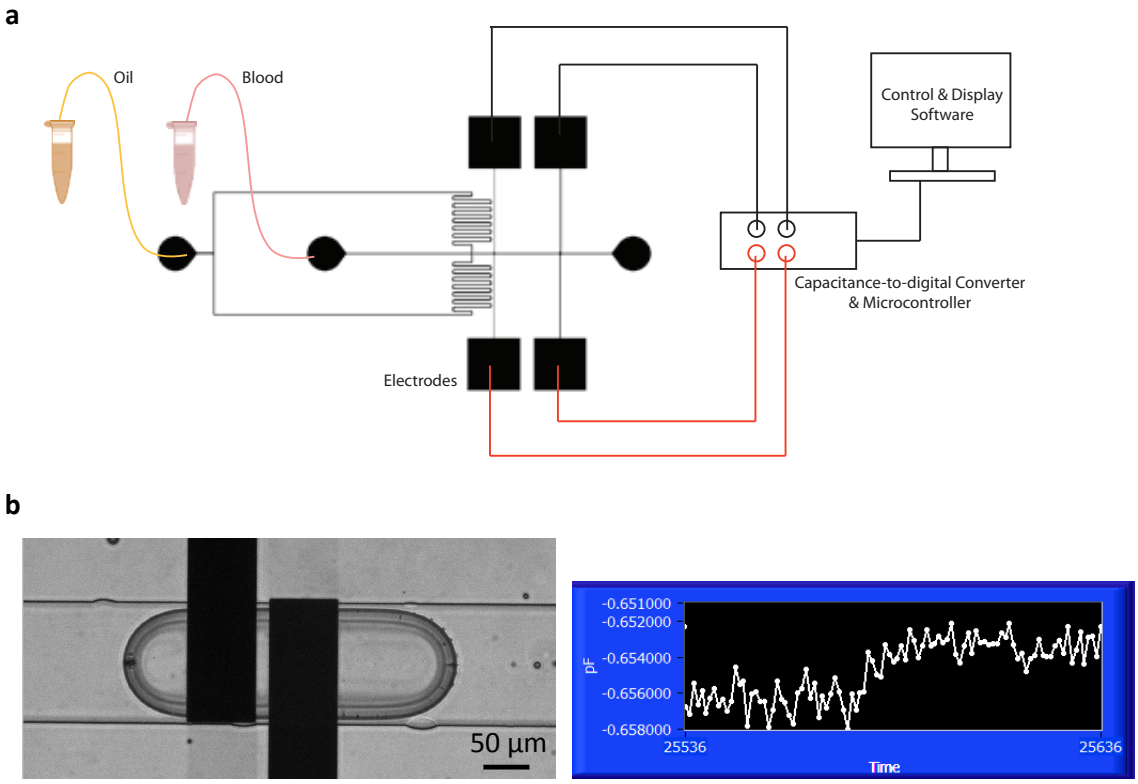

Figure 4.5: Schematics of capacitive droplet sensor and preliminary results on droplet detection. (a) Modification on the microfluidic viscometer to include on-chip capacitive sensors. (b) Preliminary results on droplet sensing. The passage of a single droplet though the electrodes induces a change in capacitance of approximately 0.001-0.002 pF.

4.3.4 Device Automation

To apply the microfluidic viscometer as a point-of-care solution in clinical settings such as an emergency room and ambulance, we automated the device by including a capacitance-based on-chip sensor to measure droplet lengths and speeds (Fig. 4.5a). The capacitive sensor measures changes in capacitance when an aqueous droplet passes through the electrodes due to a 30-fold increase in dielectric constants ε ($\varepsilon_{water} = 80$ and $\varepsilon_{oil} = 2.5$). [20] Therefore, an increase in capacitance signal can be observed in the presence of an aqueous droplet. If we integrate two electrodes on-chip, the speed of droplets can be measured using the same principle as speed detectors for cars, and the lengths of droplets can be determined from the duration of the peak capacitance signal and droplet speeds. In the experiment, we fabricated gold electrodes with parallel rod geometry (Fig. 4.5b) and interdigital finger geometry. Our preliminary results prove the feasibility of detecting the passage of a single droplet (approximately 350 μm in length), which induces a change in capacitance of 0.01-0.02 pF. However, further improvement of the capacitive sensor is necessary to reduce the signal-to-noise ratio and increase the detection sensitivity in order to measure droplet speeds and lengths.

4.4 Conclusion

The microfluidic viscometer presents a new platform to measure blood viscosities and monitor blood coagulation, providing information that was not accessible previously due to the limited amounts of blood samples. With the microfluidic viscometer, we were able to analyze viscosities of banked blood of different storage time and reaction kinetics of blood coagulation of citrated whole blood under different conditions. To use the microfluidic viscometer in an emergency room or ambulance, the device can be automated using an on-chip capacitive sensor and the constant pressure source

can be replaced by a portable vacuum pump at the outlet. Our preliminary results prove the feasibility of capacitance-based droplet sensing, yet further research would be necessary to improve the sensitivity of the capacitive sensors for device automation.

4.5 Bibliography

[1] D. S. Kauvar, R. Lefering, and C. E. Wade. Impact of hemorrhage on trauma outcome: an overview of epidemiology, clinical presentations, and therapeutic considerations. *J Trauma*, 60(6 Suppl):S3–11, 2006.

[2] J. R. Hess. Blood and coagulation support in trauma care. *ASH Education Program Book*, 2007(1):187–191, 2007.

[3] World Health Organization. Injuries and violence: the facts 2014. 2014.

[4] J. B. MacLeod, M. Lynn, M. G. McKenney, S. M. Cohn, and M. Murtha. Early coagulopathy predicts mortality in trauma. *J Trauma*, 55(1):39–44, 2003.

[5] L. Rugeri, A. Levrat, J. S. David, E. Delecroix, B. Floccard, A. Gros, B. Allaouchiche, and C. Negrier. Diagnosis of early coagulation abnormalities in trauma patients by rotation thrombelastography. *Journal of Thrombosis and Haemostasis*, 5(2):289–295, 2007.

[6] D. R. Spahn, B. Bouillon, V. Cerny, T. J. Coats, J. Duranteau, E. Fernandez-Mondejar, D. Filipescu, B. J. Hunt, R. Komadina, G. Nardi, E. Neugebauer, Y. Ozier, L. Riddez, A. Schultz, J. L. Vincent, and R. Rossaint. Management of bleeding and coagulopathy following major trauma: an updated european guideline. *Crit Care*, 17(2):R76, 2013.

[7] K. A. Wood and D. C. Angus. Pharmacoeconomic implications of new therapies in sepsis. *Pharmacoeconomics*, 22(14):895–906, 2004.

[8] M. J. Hall, S. N. Williams, C. J. DeFrances, and A. Golosinskiy. Inpatient care for septicemia or sepsis: a challenge for patients and hospitals. 2011.

[9] D. R. Spahn and R. Rossaint. Coagulopathy and blood component transfusion in trauma. *Br J Anaesth*, 95(2):130–9, 2005.

[10] E. Gonzalez, E. E. Moore, H. B. Moore, M. P. Chapman, C. C. Silliman, and A. Banerjee. Trauma-induced coagulopathy: an institution's 35 year perspective on practice and research. *Scandinavian Journal of Surgery*, 103(2):89–103, 2014.

[11] J. S. Hagemo. Prehospital detection of traumatic coagulopathy. *Transfusion*, 53 Suppl 1:48S–51S, 2013.

[12] L. T. Da Luz, B. Nascimento, A. K. Shankarakutty, S. Rizoli, and N. K. Adhikari. Effect of thromboelastography (teg®) and rotational thromboelastometry (rotem®) on diagnosis of coagulopathy, transfusion guidance and mortality in trauma: descriptive systematic review. *Critical Care*, 18(5):1, 2014.

[13] G. A. M. Pop, D. J. Duncker, M. Gardien, P. Vranckx, S. Versluis, D. Hasan, and C. J. Slager. The clinical significance of whole blood viscosity in (cardio)vascular medicine. *Netherlands Heart Journal*, 10(12):512–516, 2002.

[14] A. L. Fogelson and K. B. Neeves. Fluid mechanics of blood clot formation. *Annu Rev Fluid Mech*, 47:377–403, 2015.

[15] Y. Li, K. R. Ward, and M. A. Burns. Viscosity measurements using microfluidic droplet length. *Analytical Chemistry*, submitted, 2016.

[16] A. Renshaw. *Henry's Clinical Diagnosis and Management by Laboratory Methods*. LWW, 2007.

[17] G. Hochleitner, K. Sutor, C. Levett, H. Leyser, C. J. Schlimp, and C. Solomon. Revisiting hartert's 1962 calculation of the physical constants of thrombelastography. *Clin Appl Thromb Hemost*, 2015.

[18] A. Zambruni, U. Thalheimer, G. Leandro, D. Perry, and A. K. Burroughs. Thromboelastography with citrated blood: comparability with native blood, stability of citrate storage and effect of repeated sampling. *Blood Coagulation and Fibrinolysis*, 15(1):103, 2004.

[19] M. V. Wohlauer, E. E. Moore, J. Harr, E. Gonzalez, M. Fragoso, and C. C. Silliman. A standardized technique for performing thromboelastography in rodents. *Shock*, 36(5):524–6, 2011.

[20] C. Elbuken, T. Glawdel, D. Chan, and C. L. Ren. Detection of microdroplet size and speed using capacitive sensors. *Sensors and Actuators A: Physical*, 171(2):55–62, 2011.

CHAPTER V

Asynchronous Magnetic Bead Rotation (AMBR) Microviscometer for Label-Free DNA Analysis

5.1 Introduction

Sensitive and cost-effective DNA detection methods have a wide range of applications, from clinical diagnostics and drug development to the food industry and forensic sciences. [1–4] In medical diagnostics, especially for infectious diseases, DNA detection technology such as quantitative polymerase chain reaction (qPCR), restriction fragment length polymorphism (RFLP) and ligation detection reaction (LDR) are crucial diagnostic tools. [5–7] Fluorescence has been used almost exclusively as the DNA detection method in these tools due to its simplicity and high sensitivity. [6, 7] Recently, numerous efforts have been made to seek more cost-effective DNA detection technologies, notably for use in the developing world, yet none of them achieve the same sensitivity and applicability as fluorescence-based methods. [8–10]

Another approach to detect and quantify DNA in diagnostic reactions is to measure the solution viscosity. [11, 12] The viscosity of a double-stranded DNA (dsDNA) solution at a known temperature depends on the mass concentration and the average length of the DNA strands. The solution viscosity can indicate DNA concentration and/or length. [13–15] In restriction digestion reactions the solution viscosity de-

creases as longer DNA strands are cut into shorter pieces. Alternatively, in PCR, the solution viscosity increases as the length of the DNA increases, through polymerization of the target sequence. Notably, measurement of changes in solution viscosity does not require specific DNA chemical modification or pre-labeling.

Here we report on a microviscometer that is based on asynchronous magnetic bead rotation (AMBR) and used for DNA detection. AMBR detection monitors the rotational motion of a free-floating magnetic bead placed in a rotating magnetic field and uses changes in this motion to infer physical properties of the surrounding solution. When the rotation rate of the external field exceeds a critical value, the bead rotates at a speed different from that of the external field. The rate of this asynchronous rotation is viscosity dependent. Readily available paramagnetic microbeads can thus be used for measuring changes in DNA concentrations or average lengths. This chapter was partially modified from the paper: Yunzi Li, David T. Burke, Raoul Kopelman, and Mark A. Burns, "Asynchronous Magnetic Bead Rotation (AMBR) Microviscometer for Label-Free DNA Analysis"; *Biosensors*, 03/2014, 4(1), 76-89.[16].

5.2 Materials and Methods

5.2.1 Reagents

Solutions used in the viscosity test were purchased from Sigma-Aldrich, unless otherwise specified. Samples tested in the experiment include glycerol and water solutions, lambda DNA *Eco*RI digest with lengths of 3530-21226 bp, and pUC18 *Hae*III digest with lengths of 80-587 bp. Magnetic beads with diameters of 7.6, 16 and 45 μm were purchased from Spherotech Inc.

In digestion reactions and PCR amplification, lambda DNA was used as the template and purchased from Life Technologies. The restriction enzymes *Eco*RI with *Eco*RI buffer and *Pvu*I with NEBuffer 3 were purchased from New England Biolabs.

For PCR, the forward primer is 5′-GGTGCTTTATGACTCTGCCGC-3′, and the reverse primer is 5′-CGGCACTGGCAAGCAACTGA-3′. Both primers were purchased from Integrated DNA Technologies. PCR master mix was purchased from Promega.

5.2.2 Viscosity Measurement

The magnetic beads were washed with water three times and a concentrated bead solution was added to the samples (with 0.2% bovine serum albumin as a non-specific blocking agent). The bead concentration in the sample solution is 0.0075%w/v. The sample solution was rapidly mixed and then placed between two glass slides. The microviscometer can work with very small liquid volumes ($< 10\,\mu$l). Double-sided tape was inserted between the two glass slides, and nickel particles (210-420 μm) were placed on the edges of the tape to ensure a minimum gap of 210 μm between the two glass slides. Finally, silicone sealant (Dow Corning) was applied to the exterior edges to prevent sample evaporation.

The glass slides were placed in a planar observation area confined within a controlled magnetic field. The latter was generated using orthogonal Helmholtz coils (Fig. 5.1a). Viscosity measurements with AMBR microviscometer were conducted at $25 \pm 1\,^{\circ}$C. The magnetic field was measured with a 3-axis magnetic field probe (C-H3A-2m; Senis GmbH, Switzerland). The field strength was 2.7 mT and a driving frequency was as specified for each experiment, both of which were controlled with a custom LabVIEW program. Image stacks of bead rotations were recorded during the experiment at a rate of 10 frames per second. Rotation periods of ten randomly selected beads were recorded for each sample, to accommodate the wide variance in commercial bead properties. The image stacks were analyzed using ImageJ, and a plot of image intensity versus image number was generated by ImageJ. The plot was imported into MATLAB, and the periodicity of the bead rotation was determined by applying a fast Fourier transform.

The viscosities of glycerol and water solutions at 25 °C were verified using an Ubbelohde viscometer. Briefly, 15 ml glycerol and water solution were poured into an Ubbelohde viscometer that was immersed in a water bath. The time that it took to pass through two calibrated marks on the viscometer was measured and used to determine the solution viscosity.

5.2.3 Preparation of Digestion Reaction Samples

In the digestion reactions, the restriction enzymes, the corresponding buffers, lambda DNA and nuclease free water were mixed and incubated at 37 °C for 1 hr. After the reaction, the solutions were placed in a 25 °C water bath before being measured by the AMBR microviscometer.

5.2.4 Preparation of PCR Samples

All the reagents were added and mixed, and then distributed, 50 μl of the mixture to each tube. The tubes were capped during the reaction to prevent evaporation. Two tubes were used as the product of cycle 0, and the rest were put into a thermal cycler (Bio-Rad). The thermal cycling involved an initial denaturation at 95 °C for 30 s, followed by six amplification cycles. The thermal cycles were: 95 °C for 30 s (denaturation), 60 °C for 1 min (annealing), 72 °C for 5 min (extension). Then, the reactions were stopped and held at 4 °C. Two tubes of samples were taken out from the thermal cycler, and labeled as cycle 6. The rest of the samples underwent resumption of the reaction with an additional five cycles. This was repeated until a total of 41 cycles was completed for the last two tubes of samples. All the samples extracted from different cycles of the reaction were stored in a -20 °C freezer, and placed in a 25 °C water bath before AMBR measurement or gel electrophoresis.

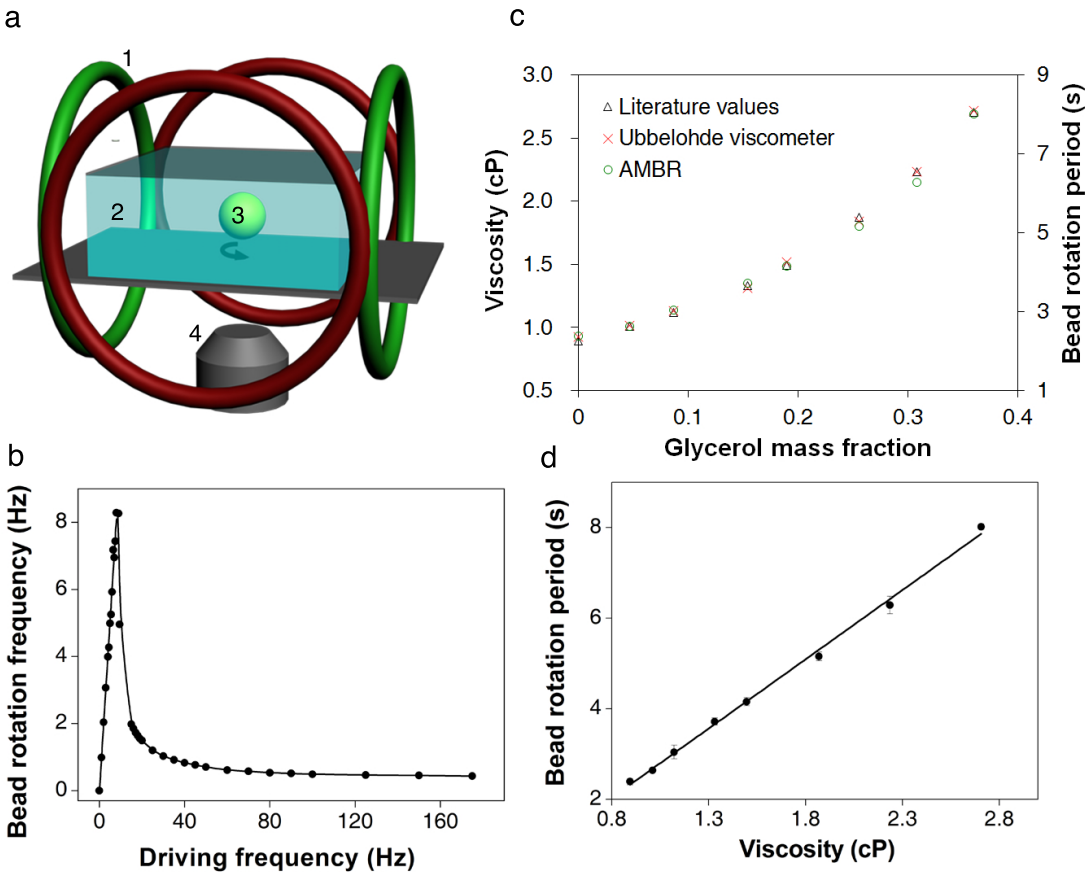

Figure 5.1: Asynchronous magnetic bead rotation (AMBR) micro-viscometer. (a) A schematic experimental set-up of an AMBR microviscometer. 1: perpendicular Helmholtz coils for rotating field generation; 2: liquid to be measured; 3: magnetic bead; 4: inverted microscope objective. (b) Observed bead rotation frequency vs. field driving frequency. Below 9 Hz the bead rotation frequency matches that of the field; above 9 Hz, the bead rotates asynchronously, with frequency decreasing as the driving frequency increases. (c) Viscosity measurement of glycerol/water mixture solutions. The graph compares AMBR results in a magnetic field with 100 Hz driving frequency to published values and conventional (Ubbelohde) viscometer measurements of the same liquid. (d) AMBR microviscometer linear response to viscosity in prepared solutions of glycerol/water. Error bars represent standard deviations among three measurements.

5.2.5 Gel Electrophoresis

Gel electrophoresis was used to verify the DNA solution results measured by the AMBR microviscometer. A 0.8% agarose gel was prepared, and 1 μl reaction solution

was diluted and loaded onto the gel. The gel electrophoresis was conducted in a 1 × TBE buffer at 10 V/cm for 2 hr. The fluorescent signal intensities of the 4500 bp bands were estimated with ImageJ.

5.3 Results and Discussion

5.3.1 Calibration of AMBR Viscometer

A linear relationship was found between the solution viscosity and the rotation period of the bead in the solution. A series of glycerol/water solutions with varying glycerol mass fraction were analyzed by the AMBR microviscometer and, in parallel, with an Ubbelohde viscometer. [17] The microviscometer results matched both the Ubbelohde viscosity values and the theoretically predicted values for the mixtures over a viscosity range from 0.89 to 2.8 cP (Fig. 5.1c). [18] A correlation curve relating the bead rotation period with the solution viscosity was constructed and yielded excellent uniformity (Fig. 5.1d). The experimentally observed linear relationship between rotation and viscosity agrees well with the theory developed for the paramagnetic AMBR system. [19]

The linear calibration curve of the microviscometer is robust to variations in properties of the magnetic beads and magnetic fields. We calibrated the microviscometer using magnetic beads of different sizes (Fig. 5.2) and under different magnetic field driving frequencies (Fig. 5.3). Among different magnetic beads, the 45 μm beads shows optimal linear correlation results, because of its high sensitivity (i.e., a high value of the slope of curve) and high precision (i.e., low values of standard deviations). When operating the microviscometer at different driving frequencies, we note that the linearity does not hold as well for a frequency close to the instability threshold as shown in Figure 5.3. Furthermore, the measurement of rotation period is not as reliable, because the jerky motion affects the image analysis. Therefore, we chose

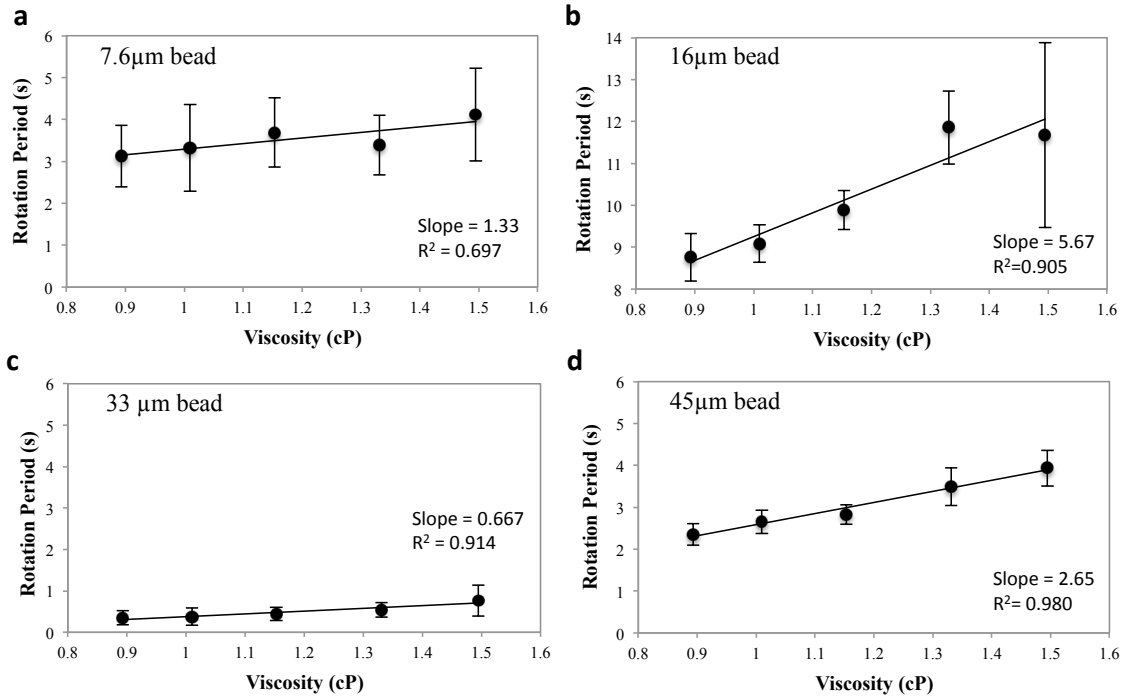

Figure 5.2: Calibration curves at 100 Hz using beads of different sizes. (a) 7.6 μm; (b) 16 μm; (c) 33 μm; (d) 45 μm. Error bars represent standard deviations among 10 beads in one measurement.

to use only the higher driving frequency regime for the DNA measurements.

The observed linear correlation between solution viscosity and bead rotation period can be explained by the nonlinear magnetic oscillation theoretical framework. [19–23] At a low driving frequency, the bead rotates at the same rate as the driving magnetic field. However, as the driving frequency increases, the bead cannot overcome the viscous drag exerted by the surrounding fluid, and thus cannot follow the rotating magnetic field. The bead then rotates slower, and asynchronously, with respect to the driving magnetic field (Fig. 5.1b). [19, 20, 23–26] The nonlinear oscillation only occurs in the asynchronous regime. In a low Reynolds number environment, the force balance between the magnetic torque and the viscous drag yields the relationship between the bead rotation period and the solution viscosity. The effects of interaction between the magnetic bead and the solid surface can be neglected under the experi-

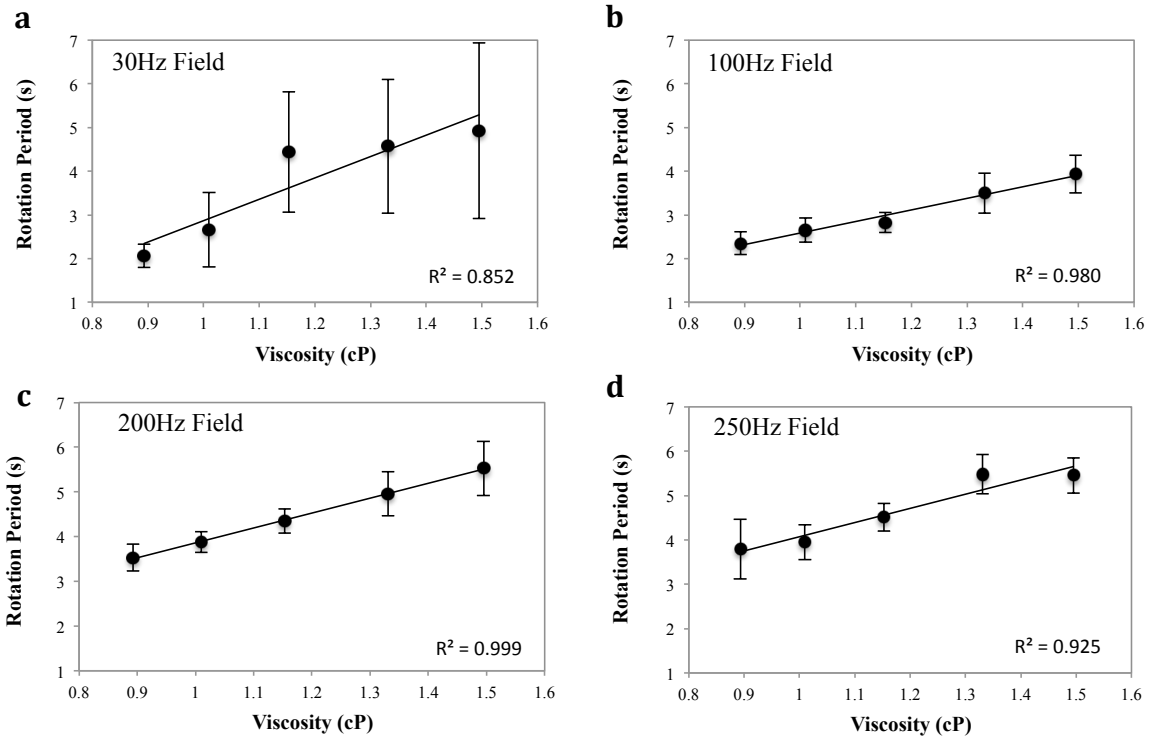

Figure 5.3: Calibration curves of 45 μm bead at different driving frequencies. (a) 30 Hz; (b) 100 Hz; (c) 200 Hz; (d) 250 Hz. The critical frequency is at 10-15 Hz. The error bars represent the standard deviations among ten different beads in one measurement. The calibration curves yield good linearity consistently at frequencies away from the critical frequency, i.e., from 100 Hz to 250 Hz.

mental conditions described in the Experimental Section. For a paramagnetic bead, the magnetic torque due to the induced magnetic dipole can be expressed as, [19]

$$\Gamma_{\mathrm{mag}} = \frac{\chi'' \mathrm{v_m} \mathrm{B}^2}{\mu_0} \tag{5.1}$$

where χ'' is the imaginary part of the magnetic susceptibility (which is frequency dependent), $\mathrm{V_m}$ is the volume of the bead's magnetic content (i.e., the magnetic nanoparticles embedded in the bead), B is the strength of the driving magnetic field, and μ_0 is the permeability of free space. The torque due to the viscous drag can be expressed as,

$$\Gamma_{\text{vis}} = -\kappa\eta \mathrm{V}\frac{\mathrm{d}\phi}{\mathrm{dt}} \tag{5.2}$$

where ϕ is the arc length of the rotation, κ is the shape factor of the bead ($\kappa = 6$ for a sphere), η is the solution viscosity, and V is the volume of the magnetic bead. By combining Equations 5.1 and 5.2, the equation becomes,

$$\frac{\mathrm{T}}{\eta} = \frac{2\pi\mu_0\kappa\mathrm{V}}{\chi''\mathrm{V_M}\mathrm{B}^2} \tag{5.3}$$

Therefore, in the asynchronous regime, the rotation period of a paramagnetic bead, under the rotating field of a given strength and frequency, is expected to be linearly proportional to the solution viscosity, i.e., $\mathrm{T} \propto \eta$. Our experimentally observed results confirm this theoretical relationship.

To advance the practical utility of the asynchronous rotation method, we investigated the influence of the variation in bead properties on bead rotation periods. A relative standard deviation of approximately 10% is observed due to the variation in bead properties, such as size and magnetic content. As shown in Figure 5.4a, the rotation periods of 20 beads in the same solution do not show a clear bead-size dependency. Thus, bead-size non-uniformity is not the primary contributor to the variation in the rotation period measurement, despite the expected correlation in Equation 5.3. More likely, the bead magnetic properties, such as magnetic volume and susceptibility, are more significant for the inter-bead variation than is the size variation. The scattered pattern in Figure 5.4a supports the averaging over multiple beads in the construction of correlation curves and viscosity measurement experiments.

To confirm that inter-bead variation in the rotation period is primarily due to inherent bead properties, we measured the rotation period of the same bead continuously over time. The differences in rotation period over time are much smaller than the differences between two beads in the same experiment (Fig. 5.4b). The

relative standard deviation for a single bead over time is approximately 1%, 10 times smaller than the standard deviation in the rotation period among 10 beads. Therefore, the observed measurement error is smaller than the error caused by the bead non-uniformity. A wide variation in commercial bead properties has been observed before [27, 28]; consequently, improved uniformity of bead magnetic character and size is expected to give better sensitivity in viscosity measurement.

5.3.2 Viscosity Measurement of DNA Aqueous Solutions

There is a linear relationship between the viscosity of common diagnostic reaction solutions and the concentration of DNA in those solutions. At a fixed temperature, the relationship between the solution viscosity, η, and the DNA concentration, C, for a very dilute solution can be expressed as $\eta = \eta_0(1+\mathrm{C}[\eta])$, where η_0 is the viscosity of the solvent and $[\eta]$ is the intrinsic viscosity of the DNA product. This equation gives a linear correlation between the viscosity and the macromolecule concentration. The intrinsic viscosity increases with the molecular weight of dsDNA, and this correlation has been documented, [15]

$$[\eta] = 3.5 \times 10^{-6} \times MW_{DNA}^{1.05}, \qquad 7 \times 10^3 \leq MW_{DNA} \leq 2 \times 10^6 \tag{5.4a}$$

$$[\eta] = 8.0 \times 10^{-4} \times MW_{DNA}^{0.690}, \qquad 2 \times 10^6 \leq MW_{DNA} \leq 8 \times 10^6 \tag{5.4b}$$

The linear relationship between the viscosity and the DNA concentration breaks down at very high molecular weight or high concentration due to the non-Newtonian property of the DNA solution. [29]

Digestion of DNA with *Eco*RI has a variety of uses and performs a selective cleaving of DNA at a specific site, forming DNA fragments of length 3530, 4878, 5643, 5804, 7421 and 21226 bp from lambda DNA of original length of 48502 bp. With the experimental relationship given in Figure 5.1c, we estimated the viscosities

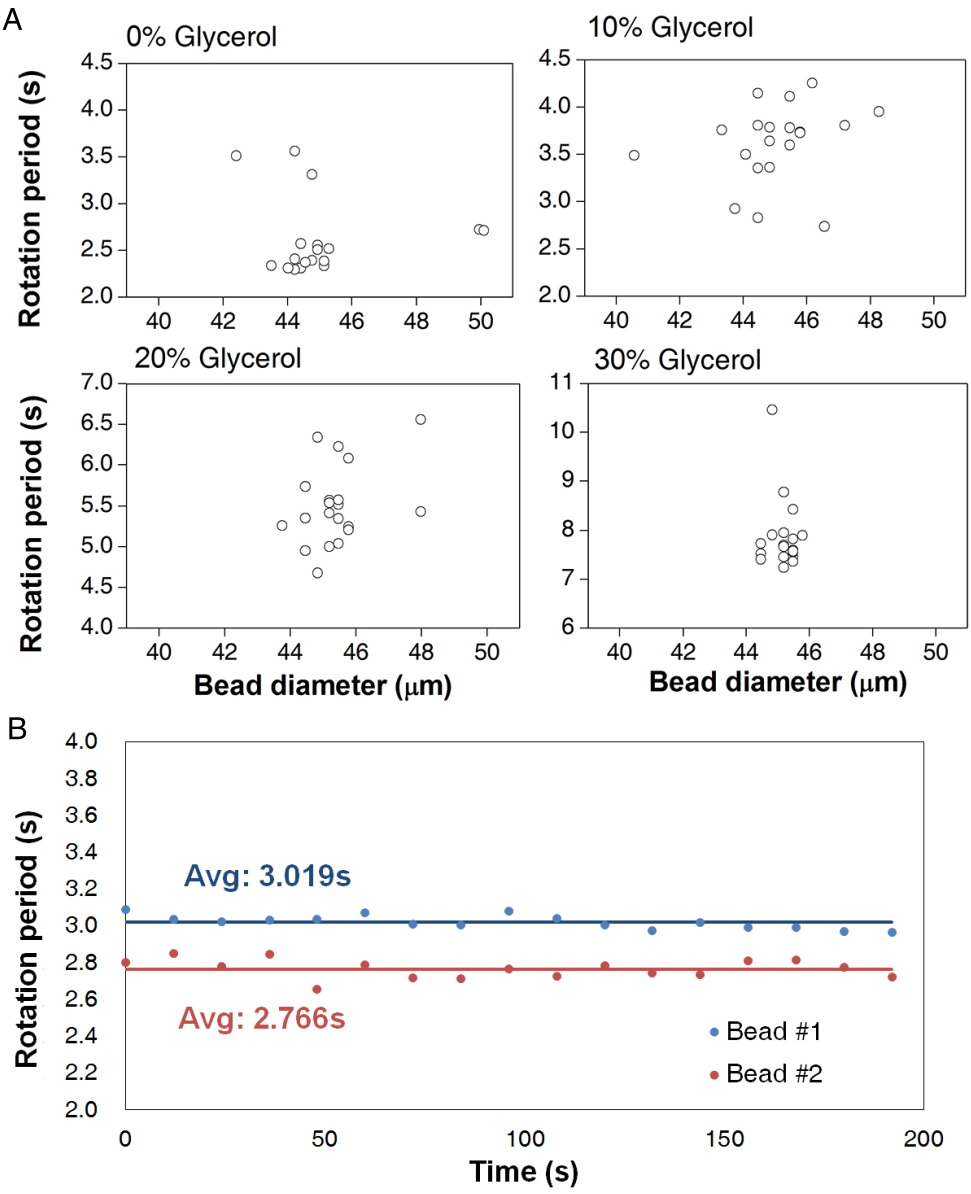

Figure 5.4: Reproducibility of AMBR viscosity measurements at 100 Hz driving frequency. (a) Rotation period measurement of 20 independent beads in the same solution plotted against the optically measured bead size of each bead. (b) The rotation periods of two examples of 45 μm beads observed over time in the same solution. The rotation periods are calculated over a 12 s period and plotted in the graph. The average values are for 17 sequential observations.

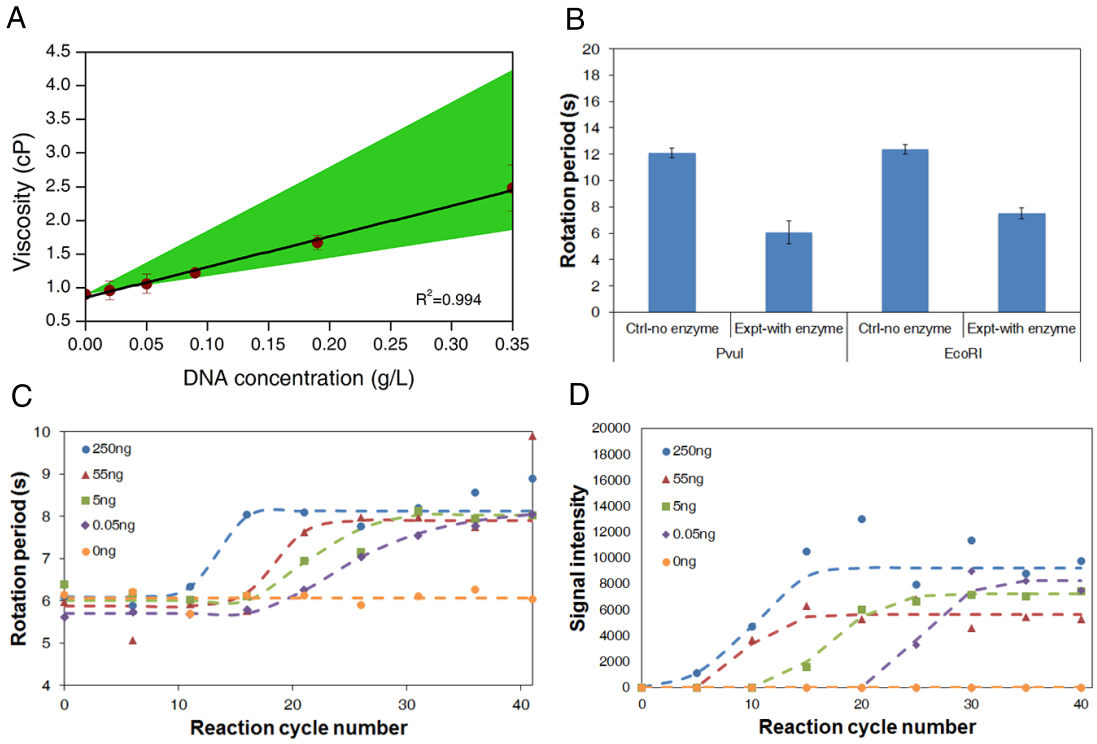

Figure 5.5: DNA measurement using AMBR microviscometer. (a) Viscosities of lambda DNA *Eco*RI digested DNA at different concentrations, as measured by AMBR microviscometer. The green area indicates the expected range of the viscosity calculated theoretically, assuming that only the longest (top range) or only the shortest (bottom range) DNA fragment size are present. Error bars represent standard deviations among 10 beads in one measurement. (b) Measurement of bead rotation period of pre- and post- digestion samples of lambda phage DNA by AMBR microviscometer. The field driving frequency is 150 Hz. The error bars show the standard deviations among 10 beads in each measurement. (c) Measurement of viscosity by bead rotation period in PCR reactions sampled every 5 cycles, starting from the 6th cycle. PCR reactions with initial DNA amounts of 0 ng, 0.05 ng, 5 ng, 55 ng, and 250 ng are shown. The reaction volumes are 50 μl each. The field driving frequency is 150 Hz, and the PCR product size is 4500 bp. Each point represents the mean value, observing ten beads. (d) Fluorescent signal intensities of the PCR product (4500 bp band) observed on a electrophoresis gel for the same samples measured in (c).

of the DNA *Eco*RI digest solutions, at different concentrations, using the measured bead rotation periods. A linear relationship was found between the solution viscosity

	Experimental Results		Expected Range	
DNA Conc. (g/l)	Rotation Period (s)	Viscosity (cP)	Min Viscosity (cP)	Max Viscosity (cP)
0.00	2.40 ± 0.24	0.90 ± 0.05	0.89	0.89
0.02	2.70 ± 0.64	0.96 ± 0.14	0.94	1.07
0.05	3.12 ± 0.62	1.06 ± 0.14	1.02	1.34
0.09	3.87 ± 0.21	1.22 ± 0.05	1.15	1.78
0.19	5.86 ± 0.49	1.67 ± 0.11	1.41	2.67
0.35	9.52 ± 1.53	2.48 ± 0.34	1.85	4.18

Table 5.1: Rotation periods and viscosities of lambda DNA *Eco*RI digest DNA of different DNA concentrations measured by AMBR microviscometer. The expected ranges of viscosities are calculated, assuming only the longest or shortest piece of DNA is present.

and the DNA concentration (Table 5.1 and Fig. 5.5a), confirming the assumption that these solutions were in the dilute solution regime. The viscosities of the DNA solutions measured using the AMBR microviscometer are within the theoretically estimated upper and lower bounds.

5.3.3 Measurement of DNA Reaction Progression

Measurements of restriction digestion samples confirm that the AMBR microviscometer is sensitive to viscosity changes caused by the DNA size changes. As shown in Fig. 5.5b, a clear difference in bead rotation period can be seen between the digested and undigested lambda DNA solutions. Thus, the AMBR microviscometer can detect DNA sequence variation using a site-specific restriction endonuclease to essentially alter the solution viscosity.

Measurements of PCR reaction samples over the course of the reaction show that the AMBR microviscometer can detect the formation of PCR products in real time. As expected, the reactions with the higher initial template concentration reach the maximum product concentration sooner than those with lower template concentrations (Fig. 5.5c), and the plot of reaction cycle number versus log of initial DNA concentration yields a linear correlation (Fig. 5.6). Comparing the AMBR measure-

ments with the gel electrophoresis results on the same samples (Fig. 5.5d) confirms that the viscosity-based method is approximately 5 cycles delayed, relative to gel electrophoresis detection.

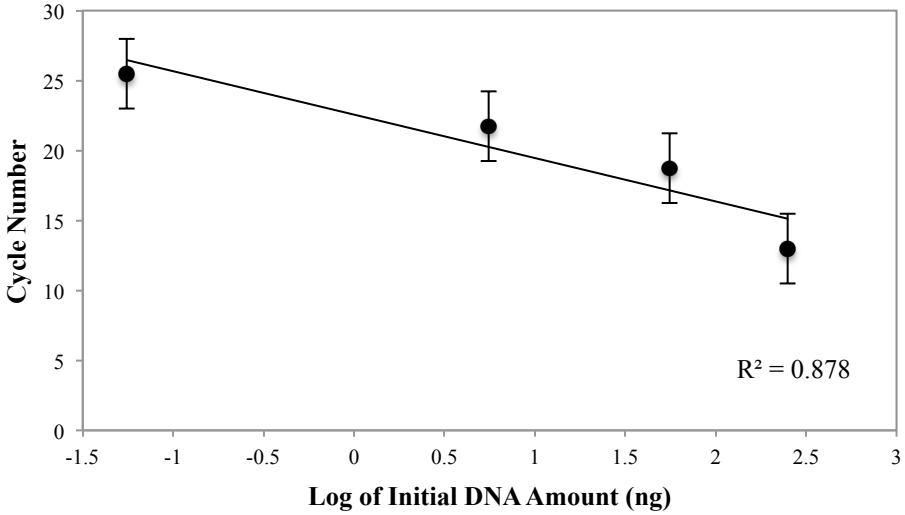

Figure 5.6: Plot of reaction cycle number versus log of initial DNA amount for the qPCR measurement by AMBR method. Error bars represent the uncertainty due to the AMBR measurement of every five cycles.

Using commercial paramagnetic beads, the AMBR microviscometer is found to be sensitive to the viscosity changes associated with DNA reactions. The results on PCR, with a product size of 4500 bp, yield a 10% relative error in the rotation period measurement. The AMBR microviscometer should be able to detect PCR product sizes as low as 1000 bp, assuming a conversion of $> 95\%$ of dNTPs to its polymerized product (i.e., 0.42 g/l final product concentration). However, this sensitivity can be further improved so as to meet the need of monitoring DNA reactions with smaller viscosity changes (e.g., PCRs with shorter DNA products) by optimizing the bead size, shape, and magnetic properties. Based on the 1% relative error observed for single bead measurements, over time, we predict that the AMBR microviscometer may be able to detect PCR with product size as low as 50 bp. By measuring the changes in viscosity of DNA solutions, our technique can measure the difference in molecular length for a known concentration or the difference in concentration for a

known length.

5.4 Conclusions

In summary, the viscosity-based approach using an AMBR microviscometer introduces a new option for label-free DNA detection and for reaction monitoring. In the viscosity range of common DNA reactions, the measurement is completed within one minute, and a typical AMBR microviscometer set-up allows continuous, real-time measurement during the course of any reaction. This viscometer requires only a small amount of sample, and volumes in the picoliter range may be accessible if integrated into a microfluidic device. A laser-photodiode apparatus can easily replace the microscope detection setup used in this work, so as to make the measurement more cost-effective. [30] Although demonstrated with DNA solutions, the viscosity-based technology described here can be applied to any polymer reaction or degradation system. An improved understanding of the AMBR microviscometer performance in complex fluids may enable new applications, such as mapping the viscosity in living cells, understanding drug delivery mechanisms, and diagnosing blood clotting.

5.5 Bibliography

[1] Y.-W. Tang, G. W. Procop, and D. H. Persing. Molecular diagnostics of infectious diseases. *Clinical Chemistry*, 43(11):2021–2038, 1997.

[2] M. A. Valasek and J. J. Repa. The power of real-time pcr. *Adv Physiol Educ*, 29(3):151–9, 2005.

[3] R. A. van Oorschot, K. N. Ballantyne, and R. J. Mitchell. Forensic trace dna: a review. *Investig genet*, 1(1):14, 2010.

[4] P. K. Mandal, A. K. Biswas, K. Choi, and U. K. Pal. Methods for rapid detection of foodborne pathogens: an overview. *Am. J. Food Technol*, 6:87–102, 2011.

[5] U. Landegren, R. Kaiser, C. T. Caskey, and L. Hood. Dna diagnostics–molecular techniques and automation. *Science*, 242(4876):229–237, 1988.

[6] M. Kubista, J. M. Andrade, M. Bengtsson, A. Forootan, J. Jonak, K. Lind, R. Sindelka, R. Sjoback, B. Sjogreen, L. Strombom, A. Stahlberg, and N. Zoric. The real-time polymerase chain reaction. *Mol Aspects Med*, 27(2-3):95–125, 2006.

[7] M. I. Handal and V. M. Ugaz. Dna mutation detection and analysis using miniaturized microfluidic systems. *Expert Review of Molecular Diagnostics*, 6(1):29–38, 2006.

[8] F. Li, A. R. Mahon, M. A. Barnes, J. Feder, D. M. Lodge, C.-T. Hwang, R. Schafer, S. T. Ruggiero, and C. E. Tanner. Quantitative and rapid dna detection by laser transmission spectroscopy. *PLoS ONE*, 6(12):e29224, 2011.

[9] M. L. Diakite, J. Champ, S. Descroix, L. Malaquin, F. Amblard, and J. L. Viovy. A low-cost, label-free dna detection method in lab-on-chip format based on electrohydrodynamic instabilities, with application to long-range pcr. *Lab Chip*, 12(22):4738–47, 2012.

[10] D. C. Leslie, J. Li, B. C. Strachan, M. R. Begley, D. Finkler, L. A. Bazydlo, N. S. Barker, D. M. Haverstick, M. Utz, and J. P. Landers. New detection modality for label-free quantification of dna in biological samples via superparamagnetic bead aggregation. *J Am Chem Soc*, 134(12):5689–96, 2012.

[11] N. Srivastava, R. D. Davenport, and M. A. Burns. Nanoliter viscometer for analyzing blood plasma and other liquid samples. *Analytical chemistry*, 77(2):383–392, 2005.

[12] E. Livak-Dahl, J. Lee, and M. A. Burns. Nanoliter droplet viscometer with additive-free operation. *Lab Chip*, 13(2):297–301, 2013.

[13] M. L. Huggins. The viscosity of dilute solutions of long-chain molecules. iv. dependence on concentration. *J Am Chem Soc*, 64(11):2716–2718, 1942.

[14] P. D. Ross and R. L. Scruggs. Viscosity study of dna. ii. the effect of simple salt concentration on the viscosity of high molecular weight dna and application of viscometry to the study of dna isolated from t4 and t5 bacteriophage mutants. *Biopolymers*, 6(8):1005–1018, 1968.

[15] A. Tsortos, G. Papadakis, and E. Gizeli. The intrinsic viscosity of linear dna. *Biopolymers*, 95(12):824–32, 2011.

[16] Y. Li, D. T. Burke, R. Kopelman, and M. A. Burns. Asynchronous magnetic bead rotation (ambr) microviscometer for label-free dna analysis. *Biosensors (Basel)*, 4(1):76–89, 2014.

[17] L. H. Cragg and H. Van Oene. Shear dependence in the viscometry of high polymer solutions: a new variable-shear capillary viscometer. *Canadian Journal of Chemistry*, 39(1):203–215, 1961.

[18] M. L. Sheely. Glycerol viscosity tables. *Industrial & Engineering Chemistry*, 24(9):1060–1064, 1932.

[19] P. Kinnunen, I. Sinn, B. H. McNaughton, D. W. Newton, M. A. Burns, and R. Kopelman. Monitoring the growth and drug susceptibility of individual bacteria using asynchronous magnetic bead rotation sensors. *Biosens Bioelectron*, 26(5):2751–5, 2011.

[20] G. Helgesen, P. Pieranski, and A. Skjeltorp. Nonlinear phenomena in systems of magnetic holes. *Physical Review Letters*, 64(12):1425–1428, 1990.

[21] G. Helgesen, P. Pieranski, and A. Skjeltorp. Dynamic behavior of simple magnetic hole systems. *Physical Review A*, 42(12):7271–7280, 1990.

[22] B. McNaughton, R. Agayan, J. Wang, and R. Kopelman. Physiochemical microparticle sensors based on nonlinear magnetic oscillations. *Sensors and Actuators B: Chemical*, 121(1):330–340, 2007.

[23] I. Sinn, P. Kinnunen, T. Albertson, B. H. McNaughton, D. W. Newton, M. A. Burns, and R. Kopelman. Asynchronous magnetic bead rotation (ambr) biosensor in microfluidic droplets for rapid bacterial growth and susceptibility measurements. *Lab Chip*, 11(15):2604–11, 2011.

[24] B. Frka-Petesic, K. Erglis, J. F. Berret, A. Cebers, V. Dupuis, J. Fresnais, O. Sandre, and R. Perzynski. Dynamics of paramagnetic nanostructured rods under rotating field. *Journal of Magnetism and Magnetic Materials*, 323(10):1309–1313, 2011.

[25] A. Tokarev, I. Luzinov, J. R. Owens, and K. G. Kornev. Magnetic rotational spectroscopy with nanorods to probe time-dependent rheology of microdroplets. *Langmuir*, 28(26):10064–71, 2012.

[26] L. Chevry, N. Sampathkumar, A. Cebers, and J. F. Berret. Magnetic wire-based sensors for the microrheology of complex fluids. *Physical Review E*, 88(6), 2013.

[27] J. Connolly, T. G. St. Pierre, and J. Dobson. Experimental evaluation of the magnetic properties of commercially available magnetic microspheres. *Bio-Medical Materials and Engineering*, 15(6):421–431, 2005.

[28] I. Sinn, P. Kinnunen, S. N. Pei, R. Clarke, B. H. McNaughton, and R. Kopelman. Magnetically uniform and tunable janus particles. *Applied Physics Letters*, 98(2):024101, 2011.

[29] Y. Heo and R. G. Larson. The scaling of zero-shear viscosities of semidilute polymer solutions with concentration. *Journal of Rheology*, 49(5):1117, 2005.

[30] A. Hecht, P. Commiskey, N. Shah, and R. Kopelman. Bead assembly magnetorotation as a signal transduction method for protein detection. *Biosensors and Bioelectronics*, 48:26–32, 2013.

CHAPTER VI

Preliminary Design of ChessTrap for Particle/Droplet Manipulation

6.1 Introduction

With continuous efforts and advances in miniaturization and optimization of reactions in microfluidic systems, a second phase, either an immiscible liquid (e.g. droplets) or a solid (e.g., particles and cells) phase, has been introduced to compartmentalize the previously continuous microfluidic systems. The use of the second phase creates individual reaction systems and effectively concentrates the reactants for better reaction kinetics and yields. For example, droplets provide a relatively closed compartment (with only diffusion of permeable material across the two-phase boundary to some extent) to isolate target reactants or cell species, rapidly mix the reaction solution, and thus drastically reduce the reaction time. [1–12] Similarly, microparticles act as a solid support for one reactant, often a substrate of an enzyme or a target of interest. These particles create an open system for the locally concentrated substrates to react with the enzyme/target in the surrounding fluids, thus increasing the likelihood and rate of a reaction (e.g. immunoassays and DNA hybridizations). [13–16]

More recently, a bio-sensing technique based on the asynchronous magnetic bead

rotation (AMBR) phenomenon has been developed. [17–19] In such systems, magnetic particles are placed in a rotating magnetic field. The rotation motion of the magnetic particles in the asynchronous regime is recorded, and the periodicity of the rotation of the magnetic particles is correlated with the measured properties, such as volumes of magnetic particles and solution viscosities surrounding the particles. This simple technique has been applied to a wide range of applications, such as biomolecule detection [20], viscosity measurement [8, 21], cell growth detection and antimicrobial susceptibility testing [22–25]. AMBR biosensors provide high measurement sensitivity and accuracy with the pre-requisite of high inter-particle uniformity of magnetic beads. However, this pre-requisite can potentially be removed if the same set of magnetic particles is used for different assays.

In order to achieve the automation and regeneration of AMBR biosensors as well as to eliminate the pre-requisite, a microfluidic platform needs to be developed to manipulate the magnetic particles, such as particle transporting, trapping, releasing, sorting and medium exchanging. [26–30] More specifically, various trapping techniques have been developed in the literature, including field-assisted trapping, physical trapping and hydrodynamic trapping. [31–37] Physical trapping techniques capture particles/droplets at constrictions that are smaller than the dimensions of the particles/droplets. Some systems force all particles/droplets through narrow openings, trapping subjects above the cut-off size of the openings. Common trapping features in these systems include arrays of constriction channels [38–41], trapping structures [42–47] or chambers with narrow outlets [48–51]. Other systems use pneumatic valves to traps particles/droplets temporarily upon actuation of the valve structures. [52–54]

In this work, we presented a preliminary prototype of a ChessTrap device to encapsulate a single magnetic bead into each trapping chamber. The device consists of a chessboard-like array of chambers and a membrane-based normally closed pneu-

matic valve on top. Upon actuation of the valve, single magnetic bead is physically trapped in the chamber. The AMBR measurements can be conducted when the valve is closed and the medium can be exchanged by opening the valve after measurements. We demonstrated the successful operation of the ChessTrap device to trap single magnetic particles in individual chambers.

6.2 Materials and Methods

6.2.1 Reagents

Fluorescent particles with diameters from $20 - 40\,\mu$m and magnetic beads with a diameter of $45\,\mu$m were purchased from Spherotech Inc. The particle solutions were diluted 10-fold for the fluorescent particles and 100-fold for the magnetic particles from the stock solutions before experiment. Bovine serum albumin (BSA) solutions were purchased from Thermo Fisher Scientific.

6.2.2 Device Fabrication

The device consists of four layers, including one silicon layer and three polydimethylsiloxane (PDMS) layers. For the silicon layer, one side of the 4 inch silicon wafer (Silicon Valley Microelectronics) was deposited with a monolayer of hexamethyldisilizane (HMDS) and then coated with $5\,\mu$m positive photoresist SPR 220 (Suss MicroTec ACS 200). The photoresist was patterned and developed using standard photolithography techniques. The silicon wafer was then etched using deep reactive ion etch (DRIE) techniques to create holes of approximately 200-300 μm in depth (STS Pegasus 4). After the residual photoresist was removed, the backside of the wafer was coated with positive photoresist using the same approach. The backside of the wafer was aligned with the front side feature and patterned using photolithography. The wafer was then glued to a dummy wafer using Santovac 5 and etched

through (approximately 200-300 μm in depth) using DRIE. The residual photoresist was completely removed with wet etching and subsequently plasma etching (YES-CV200RFS(E)). Finally, the silicon wafer was diced to yield individual devices (ADT 7100).

For the PDMS layers, standard PDMS casting techniques with SU-8 mold was used. Briefly, SU-8 2075 was spin-coated, patterned and developed on 4 inch silicon wafers to achieve a feature depth of approximately 100 μm. The wafer was then plasma activated and silanized using tridecafluoro-1,1,2,2-tetrahydrooctyl trichlorosilane in a desiccator. For PDMS curing, the PDMS monomers and the curing agent (SYLGARD 184) was mixed at a ratio of 10:1 and poured onto the SU-8 mold. The mixture was degassed and cured at 80 °C for 2 hours. The cured PDMS was cut to yield individual pieces, and inlet and outlet ports were punched. For the PDMS membrane layer, the PDMS mixture was degassed, spin-coated on to a silanized silicon wafer and then cured.

To assemble the device, the contact surface of the silicon or PDMS layer was plasma activated. The two neighboring layers were then optically aligned and put into contact. The assembly was placed on an 80 °C heating plate for 20 min before bonding the next layer. Note that the membrane layer was bonded to the PDMS layer with the valve chambers first before peeling off from the silicon wafer support.

6.3 Experimental Setup

The fluid was pumped into the device at a flow rate of approximately 0.5 ml/min and the valve was controlled by vacuum through a custom-built pressure control system. The ChessTrap device was pre-treated with BSA solution and placed in orthogonal Helmholtz coils on a microscope stage (Nikon Eclipse Ti). For the rotation period measurement of magnetic beads, the ChessTrap device was flipped and a light source from the bottom of the inverted microscope was used. The bead rotation

motion was recorded with a CCD camera (Q Imaging), and the rotation periods were measured with ImageJ. The details of the AMBR measurement can be found in [21]. The overlapped images of fluorescent particles on the ChessTrap device were captured on an Olympus BX 51 Fluorescent Microscope, and image stitching was used to scan the entire device.

6.4 Results and Discussion

6.4.1 ChessTrap Design and Fabrication

The ChessTrap design consists of a chessboard-like array of trapping chambers with a through-hole in the center of each chamber and a membrane-based valve for flow manipulation (Fig. 6.1a-c). The top part of the device is a vacuum activated normally closed valve made of PDMS (Fig. 6.1c). When vacuum is applied at the port in the center of the ChessTrap device (Fig. 6.1d), the membrane is deflected upward into the valve control chamber, permitting fluids to flow in from the inlet. The incoming flows are then forced through the holes in the center of trapping chamber or the bypasses at the right edge of the trap arrays (i.e., between the traps and the outlet port). If the size of a particle is larger than the size of the hole, it will be trapped at the hole, thus stopping flows into the chamber. Therefore, the ChessTrap design favors the capture of a single particle into each chamber. Particles that are not trapped flow into the bottom PDMS chamber, and then exit through the outlet port. Once particle trapping is completed, the valve is closed again by removing the vacuum source.

6.4.2 Particle Capturing

The capability of the ChessTrap device to capture single particle has been verified. We first tested the performance of the silicon trapping layer (without device

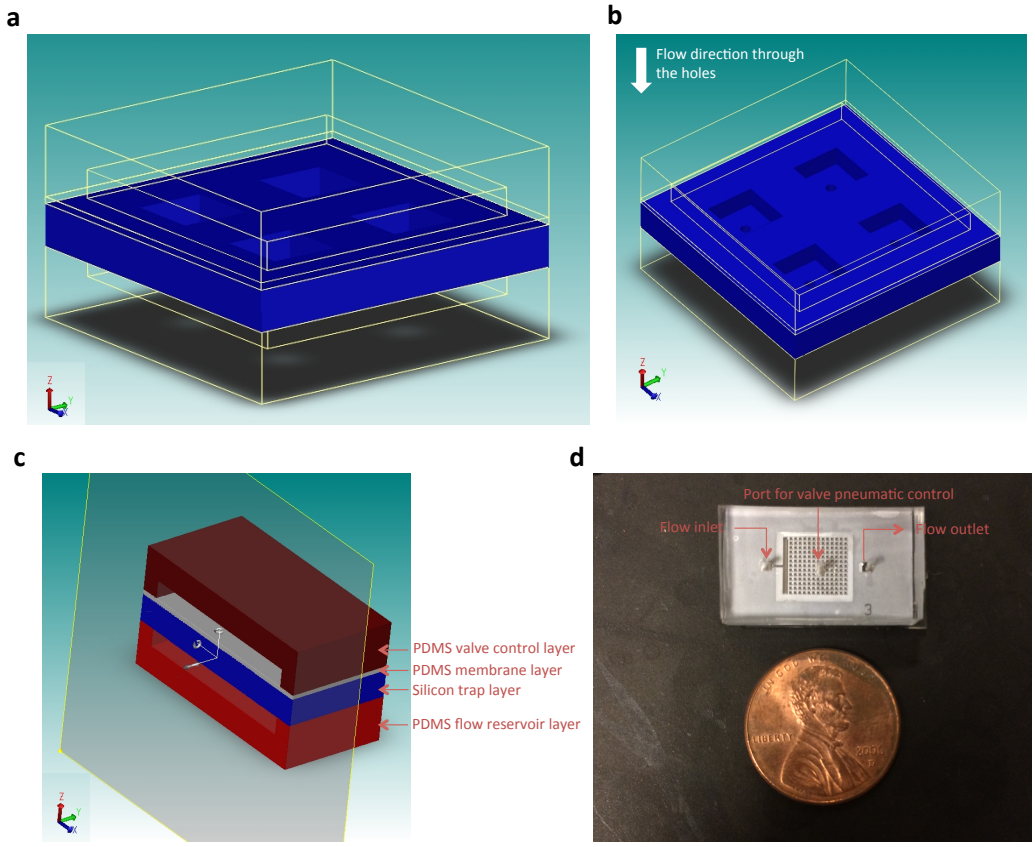

Figure 6.1: Design of a ChessTrap device. Schematics of device layout: (a) side view, (b) top view, (c) cross-sectional view. (d) A photo of the assembled device. Note that only four trapping chambers are shown in the schematics to represent the full array structures, and a bypass channel on the right edge of the array structures (i.e., close to the outlet port) and the inlet/outlet ports are not shown in the schematics. Diluted bead solution flows into the device from the inlet, then downward through the through holes or bypasses, and eventually out from the outlet. Vacuum is applied at the port in the center of the ChessTrap to open the valve.

assembly). We pipetted drops of diluted fluorescent particle solutions on top of the trapping arrays and drew vacuum from the bottom of the trapping layer. As shown in Fig. 6.2a, most of the trapping chambers contain zero or one fluorescent particle, and the particles locate in the center of the chambers. Then, we assembled the device and tested again by slowly infusing a diluted bead solution into the device upon valve actuation. Within a short period of inflow of the diluted bead solution, most

chambers captured zero or one fluorescent particle (Fig. 6.2b). However, if flowing the particle solution for longer time, it's observed that the particles suddenly accumulate at the edges of the valve structure. We think this is due to increased particle concentration over time due to particle sedimentation and the smaller openings at the edges of the valve structure, so continuous mixing of the particles is necessary to avoid sedimentation and bead aggregation and to achieve higher occupancy of the chambers.

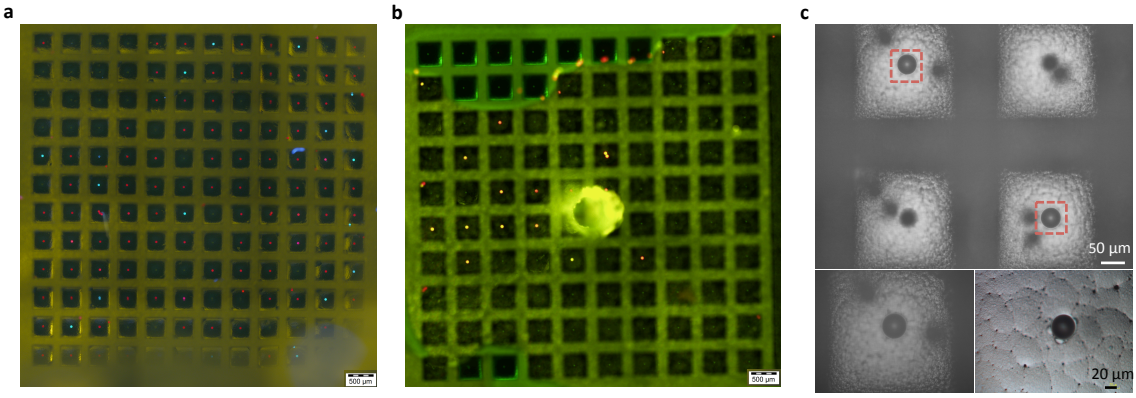

Figure 6.2: Overlapped light and fluorescent images of captured fluorescent beads on ChessTrap device. (a) Particle distribution when drawing liquid from the bottom of the silicon layer with vacuum. Fluorescent particles are 20 (red) and 30 (blue) μm in diameter. (b) Particle distribution when slowly infusing the particle solution upon valve actuation. Fluorescent particles of 30 (red) and 40 μm (yellow) were used. (c) Images of captured magnetic particles under a light microscope. The red squares in the top image indicate captured particles. Note that some dark spots due to burning exist surrounding the hole in the center of each chamber. The bottom left photo shows a captured particle in another batch of device with improved plasma etch protocol, providing better surface topology and reduced burning.

6.4.3 Preliminary Results on AMBR Measurements

We also conducted preliminary experiments to measure periods of rotation motion of magnetic beads in the trapping chambers filled with water (Table 6.1). In the synchronous regime (i.e., driving frequency below approximately 8-10 Hz), the measured

Synchronous Regime		Asynchronous Regime	
Driving frequency (Hz)	Rotation Period (s)	Driving frequency (Hz)	Rotation Period (s)
3	0.32 ± 0.02	40	0.46 ± 0.01

Table 6.1: Measurements of rotation periods in the synchronous and asynchronous rotation regimes of 45 μm paramagnetic beads in a ChessTrap device filled with water. The error bars represent the standard deviations of measurements over a period of 4 seconds.

rotation period of magnetic beads match with the period of the rotating field. In the asynchronous regime, periodicity of the magnetic beads was observed up to a driving frequency of 50 Hz, much lower than the upper limit of driving frequency of 250 Hz when the bead rotation was measured on glass slides. Above 50 Hz, the rotational motion of magnetic became irregular and eventually stopped at approximately 80 Hz, so no measurement could be made. However, the repeatability of the bead rotation period is low in the field frequency range of 10-50 Hz [21], so it is not practical to use the AMBR sensors in this frequency range.

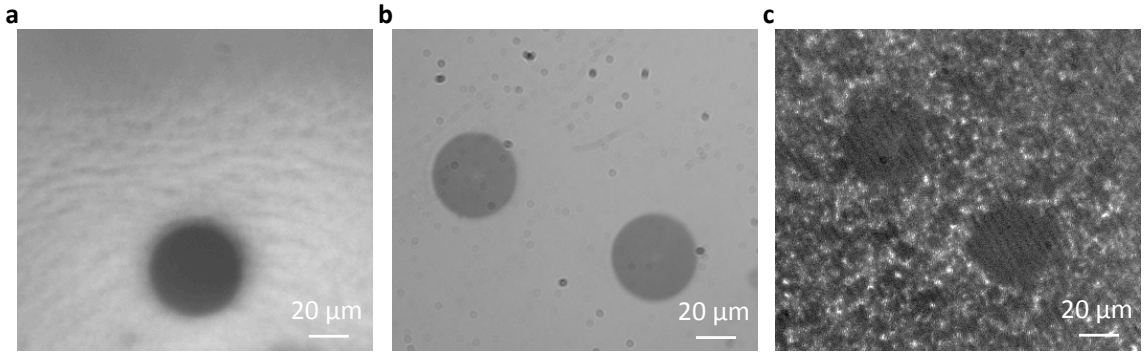

Figure 6.3: Comparison of surface roughness of the ChessTrap device with the polished and un-polished sides of a silicon wafer under a microscope. (a) ChessTrap; (b) the polished side; (c) the un-polished side.

To investigate the reason of the lower operable driving frequency in the ChessTrap device, we made the hypothesis that this narrow range of driving frequency is due to the roughness of the chamber surface. We conducted experiment to measure bead rotation periods on the polished and un-polished sides of a silicon wafer which were

pre-treated with BSA solutions. The surface of the polished side of the silicon wafer is smoother than the surface of chambers in a ChessTrap device, while the unpolished side of the silicon wafer is rougher (Fig. 6.2c and Fig. 6.3). Experimentally, we observed that the bead rotation stopped at approximately 150 Hz for measurements on the polished side, but 20 Hz for measurements on the un-polished side.

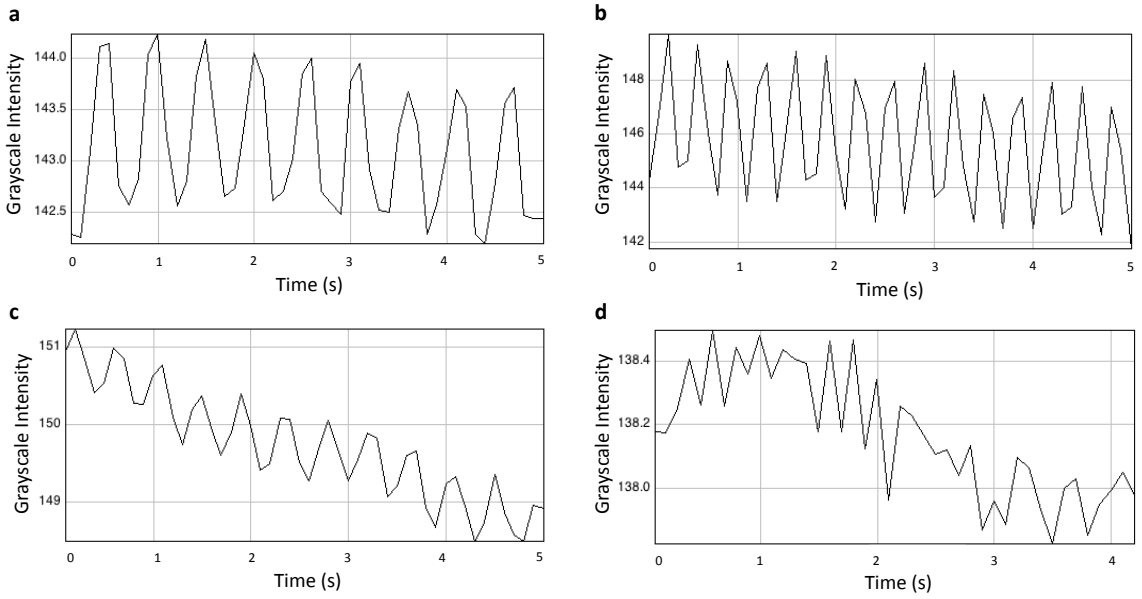

Figure 6.4: Image analysis data of bead periodicity at different field driving frequencies. The grayscale intensity of a circled area on the images was measured over time in ImageJ. The critical frequency is approximately 8-10 Hz. The driving frequencies were (a) 2 Hz; (b) 10 Hz; (c) 40 Hz; (d) 100 Hz.

We also observed rotational periodicity of magnetic beads at increasing driving frequencies on the polished side of a silicon wafer (Fig. 6.4). In the synchronous regime, the bead rotational period was approximately 0.5 s at a driving frequency of 2 Hz as expected (Fig. 6.4a). In the asynchronous regime, the bead rotated at a lower speed than the magnetic field and the rotation periods increased with driving frequencies. At frequencies slightly above the critical frequency, the intensities of the peak signals remain relatively constant (Fig. 6.4b). However, at higher frequencies, the intensities decrease over time, indicating translational motion of the magnetic

beads out of the circled area of the image (Fig. 6.4c). At driving frequencies close to its upper limit, we observed that the bead motion became irregular, containing both non-periodical rotational motion and translational motion. We suspected that this is due to increased importance of surface sticking at higher driving frequencies. This effect is expected to be more significant with higher surface roughness. The results suggest that we should use double side polished silicon wafers in the device fabrication and a better plasma etch protocol needs to be developed to ensure smooth chamber surface after fabrication.

6.5 Conclusion

In summary, we have designed a ChessTrap device to trap single particles into individual chambers. Preliminary results demonstrate that the device favorably traps only one particle into each chamber. The device could be readily scaled up by expanding the number of trapping chambers. Although we designed ChessTrap to automate AMBR sensors in our work, it has a wide range of applications, such as microarray technology for diagnosis of infection diseases or DNA sequencing. Currently, the use of AMBR sensors in the ChessTrap device has not yet been demonstrated due to the surface roughness of the chambers, and the capability of medium exchange has not yet been tested. Due to the great potential of ChessTrap for particle manipulation and bio-sensing automation, further studies and improvement need to be done in the future to make the device fully functional.

6.6 Bibliography

[1] J. Atencia and D. J. Beebe. Controlled microfluidic interfaces. *Nature*, 437(7059):648–55, 2005.

[2] H. Song, D. L. Chen, and R. F. Ismagilov. Reactions in droplets in microfluidic channels. *Angew Chem Int Ed Engl*, 45(44):7336–56, 2006.

[3] H. Song, H.-W. Li, M. S. Munson, T. G. Van Ha, and R. F. Ismagilov. On-chip titration of an anticoagulant argatroban and determination of the clotting time within whole blood or plasma using a plug-based microfluidic system. *Analytical chemistry*, 78(14):4839–4849, 2006.

[4] S. Y. Teh, R. Lin, L. H. Hung, and A. P. Lee. Droplet microfluidics. *Lab Chip*, 8(2):198–220, 2008.

[5] X. Casadevall i Solvas and A. deMello. Droplet microfluidics: recent developments and future applications. *Chem Commun (Camb)*, 47(7):1936–42, 2011.

[6] J. Park, A. Kerner, M. A. Burns, and X. N. Lin. Microdroplet-enabled highly parallel co-cultivation of microbial communities. *PLoS One*, 6(2):e17019, 2011.

[7] E. Livak-Dahl, I. Sinn, and M. Burns. Microfluidic chemical analysis systems. *Annu Rev Chem Biomol Eng*, 2:325–53, 2011.

[8] I. Sinn, T. Albertson, P. Kinnunen, D. N. Breslauer, B. H. McNaughton, M. A. Burns, and R. Kopelman. Asynchronous magnetic bead rotation microviscometer for rapid, sensitive, and label-free studies of bacterial growth and drug sensitivity. *Anal Chem*, 84(12):5250–6, 2012.

[9] M. T. Guo, A. Rotem, J. A. Heyman, and D. A. Weitz. Droplet microfluidics for high-throughput biological assays. *Lab Chip*, 12(12):2146–55, 2012.

[10] Y. Zhu and Q. Fang. Analytical detection techniques for droplet microfluidics–a review. *Anal Chim Acta*, 787:24–35, 2013.

[11] L. Mazutis, J. Gilbert, W. L. Ung, D. A. Weitz, A. D. Griffiths, and J. A. Heyman. Single-cell analysis and sorting using droplet-based microfluidics. *Nat Protoc*, 8(5):870–91, 2013.

[12] D. K. Kang, M. M. Ali, K. Zhang, S. S. Huang, E. Peterson, M. A. Digman, E. Gratton, and W. Zhao. Rapid detection of single bacteria in unprocessed blood using integrated comprehensive droplet digital detection. *Nat Commun*, 5:5427, 2014.

[13] C. T. Lim and Y. Zhang. Bead-based microfluidic immunoassays: the next generation. *Biosens Bioelectron*, 22(7):1197–204, 2007.

[14] M. D. Tarn and N. Pamme. Microfluidic platforms for performing surface-based clinical assays. *Expert Rev Mol Diagn*, 11(7):711–20, 2011.

[15] T. Konry, S. S. Bale, A. Bhushan, K. Shen, E. Seker, B. Polyak, and M. Yarmush. Particles and microfluidics merged: perspectives of highly sensitive diagnostic detection. *Mikrochim Acta*, 176(3-4):251–269, 2012.

[16] K. N. Han, C. A. Li, and G. H. Seong. Microfluidic chips for immunoassays. *Annu Rev Anal Chem (Palo Alto Calif)*, 6:119–41, 2013.

[17] B. H. McNaughton, K. A. Kehbein, J. N. Anker, and R. Kopelman. Sudden breakdown in linear response of a rotationally driven magnetic microparticle and application to physical and chemical microsensing. *The Journal of Physical Chemistry B*, 110(38):18958–18964, 2006.

[18] B. McNaughton, R. Agayan, J. Wang, and R. Kopelman. Physiochemical microparticle sensors based on nonlinear magnetic oscillations. *Sensors and Actuators B: Chemical*, 121(1):330–340, 2007.

[19] P. Kinnunen, I. Sinn, B. H. McNaughton, and R. Kopelman. High frequency asynchronous magnetic bead rotation for improved biosensors. *Appl Phys Lett*, 97(22):223701, 2010.

[20] A. Hecht, A. A. Kumar, and R. Kopelman. Label-acquired magnetorotation as a signal transduction method for protein detection: aptamer-based detection of thrombin. *Anal Chem*, 83(18):7123–8, 2011.

[21] Y. Li, D. T. Burke, R. Kopelman, and M. A. Burns. Asynchronous magnetic bead rotation (ambr) microviscometer for label-free dna analysis. *Biosensors (Basel)*, 4(1):76–89, 2014.

[22] B. H. McNaughton, P. Kinnunen, R. G. Smith, S. N. Pei, R. Torres-Isea, R. Kopelman, and R. Clarke. Compact sensor for measuring nonlinear rotational dynamics of driven magnetic microspheres with biomedical applications. *Journal of Magnetism and Magnetic Materials*, 321(10):1648–1652, 2009.

[23] R. Elbez, B. H. McNaughton, L. Patel, K. J. Pienta, and R. Kopelman. Nanoparticle induced cell magneto-rotation: monitoring morphology, stress and drug sensitivity of a suspended single cancer cell. *PLoS One*, 6(12):e28475, 2011.

[24] P. Kinnunen, I. Sinn, B. H. McNaughton, D. W. Newton, M. A. Burns, and R. Kopelman. Monitoring the growth and drug susceptibility of individual bacteria using asynchronous magnetic bead rotation sensors. *Biosens Bioelectron*, 26(5):2751–5, 2011.

[25] I. Sinn, P. Kinnunen, T. Albertson, B. H. McNaughton, D. W. Newton, M. A. Burns, and R. Kopelman. Asynchronous magnetic bead rotation (ambr) biosensor in microfluidic droplets for rapid bacterial growth and susceptibility measurements. *Lab Chip*, 11(15):2604–11, 2011.

[26] C. Yi, C.-W. Li, S. Ji, and M. Yang. Microfluidics technology for manipulation and analysis of biological cells. *Analytica Chimica Acta*, 560(1-2):1–23, 2006.

[27] D. R. Gossett, W. M. Weaver, A. J. Mach, S. C. Hur, H. T. Tse, W. Lee, H. Amini, and D. Di Carlo. Label-free cell separation and sorting in microfluidic systems. *Anal Bioanal Chem*, 397(8):3249–67, 2010.

[28] M. G. Simon and A. P. Lee. Microfluidic droplet manipulations and their applications. pages 23–50, 2012.

[29] P. Sajeesh and Ashis Kumar Sen. Particle separation and sorting in microfluidic devices: a review. *Microfluidics and Nanofluidics*, 17(1):1–52, 2013.

[30] Z. T. Yu, K. M. Aw Yong, and J. Fu. Microfluidic blood cell sorting: now and beyond. *Small*, 10(9):1687–703, 2014.

[31] J. Nilsson, M. Evander, B. Hammarstrom, and T. Laurell. Review of cell and particle trapping in microfluidic systems. *Anal Chim Acta*, 649(2):141–57, 2009.

[32] R. R. Pompano, W. Liu, W. Du, and R. F. Ismagilov. Microfluidics using spatially defined arrays of droplets in one, two, and three dimensions. *Annu Rev Anal Chem (Palo Alto Calif)*, 4:59–81, 2011.

[33] A. J. Mach, J. H. Kim, A. Arshi, S. C. Hur, and D. Di Carlo. Automated cellular sample preparation using a centrifuge-on-a-chip. *Lab Chip*, 11(17):2827–34, 2011.

[34] M. Tanyeri, M. Ranka, N. Sittipolkul, and C. M. Schroeder. A microfluidic-based hydrodynamic trap: design and implementation. *Lab Chip*, 11(10):1786–94, 2011.

[35] M. Tanyeri and C. M. Schroeder. Manipulation and confinement of single particles using fluid flow. *Nano Lett*, 13(6):2357–64, 2013.

[36] H. Amini, W. Lee, and D. Di Carlo. Inertial microfluidic physics. *Lab Chip*, 14(15):2739–61, 2014.

[37] A. Shenoy, C. V. Rao, and C. M. Schroeder. Stokes trap for multiplexed particle manipulation and assembly using fluidics. *Proc Natl Acad Sci U S A*, 113(15):3976–81, 2016.

[38] X. Chen, D. Cui, C. Liu, and H. Li. Microfluidic chip for blood cell separation and collection based on crossflow filtration. *Sensors and Actuators B: Chemical*, 130(1):216–221, 2008.

[39] K. Chung, C. A. Rivet, M. L. Kemp, and H. Lu. Imaging single-cell signaling dynamics with a deterministic high-density single-cell trap array. *Anal Chem*, 83(18):7044–52, 2011.

[40] R. D. Sochol, M. E. Dueck, S. Li, L. P. Lee, and L. Lin. Hydrodynamic resettability for a microfluidic particulate-based arraying system. *Lab Chip*, 12(23):5051–6, 2012.

[41] X. Li, W. Chen, G. Liu, W. Lu, and J. Fu. Continuous-flow microfluidic blood cell sorting for unprocessed whole blood using surface-micromachined microfiltration membranes. *Lab Chip*, 14(14):2565–75, 2014.

[42] D. Di Carlo, L. Y. Wu, and L. P. Lee. Dynamic single cell culture array. *Lab Chip*, 6(11):1445–9, 2006.

[43] S. L. Faley, M. Copland, D. Wlodkowic, W. Kolch, K. T. Seale, J. P. Wikswo, and J. M. Cooper. Microfluidic single cell arrays to interrogate signalling dynamics of individual, patient-derived hematopoietic stem cells. *Lab on a Chip*, 9(18):2659–2664, 2009.

[44] A. Huebner, D. Bratton, G. Whyte, M. Yang, A. J. Demello, C. Abell, and F. Hollfelder. Static microdroplet arrays: a microfluidic device for droplet trapping, incubation and release for enzymatic and cell-based assays. *Lab Chip*, 9(5):692–8, 2009.

[45] R. Burger, P. Reith, G. Kijanka, V. Akujobi, P. Abgrall, and J. Ducree. Array-based capture, distribution, counting and multiplexed assaying of beads on a centrifugal microfluidic platform. *Lab Chip*, 12(7):1289–95, 2012.

[46] X. Chen, S. Shojaei-Zadeh, M. L. Gilchrist, and C. Maldarelli. A lipobead microarray assembled by particle entrapment in a microfluidic obstacle course and used for the display of cell membrane receptors. *Lab Chip*, 13(15):3041–60, 2013.

[47] J. Lee and M. A. Burns. Asymmetric traps array for particle transport. *RSC Adv.*, 5(5):3358–3364, 2015.

[48] W. H. Tan and S. Takeuchi. A trap-and-release integrated microfluidic system for dynamic microarray applications. *Proc Natl Acad Sci U S A*, 104(4):1146–51, 2007.

[49] C. H. Schmitz, A. C. Rowat, S. Koster, and D. A. Weitz. Dropspots: a picoliter array in a microfluidic device. *Lab Chip*, 9(1):44–9, 2009.

[50] S. S. Bithi and S. A. Vanapalli. Behavior of a train of droplets in a fluidic network with hydrodynamic traps. *Biomicrofluidics*, 4(4):44110, 2010.

[51] K. Chung, Y. Kim, J. S. Kanodia, E. Gong, S. Y. Shvartsman, and H. Lu. A microfluidic array for large-scale ordering and orientation of embryos. *Nature methods*, 8(2):171–176, 2011.

[52] Y. H. Jang, C. H. Kwon, S. B. Kim, S. Selimovic, W. Y. Sim, H. Bae, and A. Khademhosseini. Deep wells integrated with microfluidic valves for stable docking and storage of cells. *Biotechnol J*, 6(2):156–64, 2011.

[53] H. S. Rho, Y. Yang, A. T. Hanke, M. Ottens, L. W. Terstappen, and H. Gardeniers. Programmable v-type valve for cell and particle manipulation in microfluidic devices. *Lab Chip*, 16(2):305–11, 2016.

[54] Y. Zhou, S. Basu, K. J. Wohlfahrt, S. F. Lee, D. Klenerman, E. D. Laue, and A. A. Seshia. A microfluidic platform for trapping, releasing and super-resolution imaging of single cells. *Sens Actuators B Chem*, 232:680–691, 2016.

CHAPTER VII

Conclusion and Future Work

7.1 Conclusion

This dissertation has demonstrated the use of droplet-based and particle-based microfluidic viscometers to measure viscosities continuously for biochemical and diagnostic analysis. These devices provide simple and cost-effective methods to acquire information on viscosity or viscosity changes in biological reactions, which has not yet been made readily accessible. This type of operation is beneficial to biological applications where samples are difficult or costly to obtain, particularly when continuous viscosity monitoring is necessary. While both devices offer highly sensitive and robust viscosity measurements, the two devices can be differentiated by their applicable viscosity range, best areas of application and the flow fields in which the viscosities are measured.

The droplet-based microfluidic viscometer measures viscosities or viscosity changes of Newtonian [Chapter II], non-Newtonian [Chapter III] and biological fluids [Chapter IV] from the lengths of droplets generated on-chip. While droplets are continuously generated, the continuous viscometer is capable of measuring viscosity changes in 10 seconds or less and consuming a total sample volume of less than 1 μl per hour. The range of measurable viscosity spans three orders of magnitude. This is the first time that a change in droplet size, which can be readily measured either optically

(e.g. microscopes) or electronically (e.g. on-chip capacitive sensors or diodes), has been used as a highly sensitive indicator of viscosity. Furthermore, the flow in the microfluidic channels is driven by constant pressure/vacuum source, and the channel dimensions are on the orders of μm. Therefore, it measures viscosity in a pressure-driven flow, thus best for continuous viscosity measurements of fluids in pipelines or blood in microvascular networks.

The particle-based microfluidic viscometer measures viscosities surrounding the rotating magnetic particles continuously from their rotational periods [Chapter V]. The viscometer applies the phenomenon of asynchronous magnetic bead rotation (AMBR) and the reduction in rotational periods due to viscous drag is measured to calculate viscosities. The AMBR viscometer measures viscosities in a velocity-driven flow, and offers rapid viscosity measurements with ultra-high sensitivity, especially in the low viscosity range. The technology can live up to its full potential in applications such as DNA quantification in diagnostic reactions and viscosity mapping inside cells. The operation of AMBR viscometers can potentially be automated using the microfluidic ChessTrap device, which enables transport, multiplexing and regeneration of the particle-based viscometers [Chapter VI].

7.2 Future Work

The droplet-based microfluidic viscometer developed in Chapters II-IV can be automated for point-of-care applications. Droplet lengths and speeds can be automatically measured and viscosities can be displayed in real-time by incorporating on-chip electrodes. This can be achieved either through refractive index sensing (with diodes) or capacitive sensing. Preliminary results of droplet detection using capacitive sensing have been demonstrated in Chapter IV, but more studies need to be done to reduce the signal-to-noise ratio and improve the detection sensitivity for the purpose of automation.

In addition, this droplet-based viscometer can be integrated into a blood analysis platform that measures various blood properties, such as viscosities of whole blood and blood plasma, deformability of red blood cells and kinetics of blood coagulation. This will greatly expand the applications of the device and benefits more patients and health care providers, including emergency physicians, hematologists, intensivists, surgeons, blood bankers, and pharmacists. In order to integrate different measurement capabilities onto a single chip, several microfluidic components need to be included: droplet generation, separation of whole blood into blood cells and plasma, mixing of reagents with blood droplets to trigger blood coagulation, cell deformability assays. For the cell deformability assays, preliminary experiments have been conducted using planar arrays of trapping structures with openings of decreasing size. A channel depth of approximately $3\,\mu$m is used to constrain monolayers of red blood cells to lay flat through the constrictions. The red blood cells are caught at the constrictions if they are not able to deform through the openings, and the locations where the cells are trapped indicate the deformability of the cells.

The AMBR technology described in Chapter V can potentially be used for sequence-specific detection. As suggested by the AMBR theory, the rotational period of the magnetic particles can also be used to measure volume changes of the magnetic particles due to attachment of biological targets. Preliminary evaluation of the feasibility of measuring DNA molecules directly hybridized onto oligonucleotide-coated magnetic particles has been conducted, yet with its current sensitivity, the . Therefore, we propose a two-probe method, where one DNA probe is attached to the magnetic particles and the other is labeled with gold nanoparticles. The use of nanoparticles helps amplify the signal (i.e., increase the volume change) when the target hybridizes with the two probes, thus enabling sequence-specific detection.

The preliminary design of ChessTrap device in Chapter VI can be further tested and developed to achieve full functionality. A protocol to fabricate the silicon layer

with better surface smoothness needs to be developed, and the surfaces of the ChessTrap devices need treatment to better prevent particle sticking. The development of an on-chip sensor is highly desirable to eliminate the need for a microscope. Furthermore, the robustness of the membrane-based valve upon repetitive actuation needs to be tested, and the capability of medium exchange needs to be tested. Finally, the use of ChessTrap to manipulate particles/droplets and automate AMBR biosensors (e.g. AMBR viscometer) needs to be demonstrated.